TUNABLE MICROWAVE AND MILLIMETRE-WAVE METAMATERIAL STRUCTURES AND APPLICATIONS

by

MARINA MAVRIDOU

A thesis submitted to the University of Birmingham for the degree of DOCTOR OF

PHILOSOPHY

School of Electronic, Electrical and Systems Engineering

College of Engineering and Physical Sciences

University of Birmingham

August 2015

ABSTRACT

TUNABLE MICROWAVE AND MILLIMETRE-WAVE METAMATERIAL STRUCTURES AND APPLICATIONS

MARINA MAVRIDOU

Doctorate of Philosophy

School of Electronic, Electrical and Systems Engineering

University of Birmingham

Novel designs of metamaterial structures as well as novel techniques and configurations for tuning metamaterials are presented in this PhD thesis. The proposed tuning techniques overcome the challenges that exist in other tuning techniques available thus far. Moreover, possible applications of tunable metamaterials in communication systems are proposed. Initially, tunable Electromagnetic Band-Gap (EBG) structures are proposed for low frequencies operation (3GHz to 6GHz) employing a novel biasing technique for varactor diodes. Subsequently, the proposed tunable EBG structures are applied to closely spaced antennas, achieving isolation enhancement for Multiple Input Multiple Output (MIMO) systems. Moreover, a new technique of tuning High Impedance Surface (HIS) structures is presented, with low-loss performance and no parasitic effects, based on employing two types of piezoelectric actuators, each type being suitable to a different frequency band. Particularly, bender piezoelectric actuators are used for configurations operating at low mm-wave frequencies (~15GHz) and stack multilayer actuators for operation at higher mm-wave frequencies (60GHz) where achieving a low loss performance is even more challenging. Two tunable antenna designs are also proposed incorporating both tunable HIS structures (at 15GHz and 60GHz). Finally, novel configurations of tunable Frequency Selective Surfaces (FSS) are proposed based on the concept of piezoelectric actuators to obtain a tunable

response. Again, this is carried out for two operating bands, 15GHz and 60GHz. The particular designs of tunable HIS and FSS, are directly scalable to even higher frequencies (THz), offering a promising solution at this band.

To my husband Kostas and my family,

Acknowledgements

First and foremost, I would like to thank my thesis supervisor, Dr. Alexandros Feresidis, for his support and guidance throughout my PhD without which I would not have been able to complete this work.

Furthermore, I would like to thank my second supervisor, Dr. Peter Gardner as well as Dr. Costas Constantinou for their useful insight, advices and overall support during my PhD studies.

I would also like to thank the technician of the Department of Electronic, Electrical and Systems Engineering, Alan Yates for his valuable assistance with practical issues and for the fabrication of my structures' prototypes.

In addition, I would like to acknowledge the help of Dr. James Bowen, previously working in the Department of Chemical Engineering of the University of Birmingham and currently Lecturer in Materials Engineering at The Open University, for measuring using the optical interferometer.

Special thanks go to the PhD and postdoctoral researchers of my group Konstantinos Konstantinidis, Elena Abdo Sanchez, Tade Oluwabunmi and Yuriy Nechayev.

Finally, I would like to acknowledge the financial support from the school and from EPRSC.

List of Publications

Journal papers:

1. **M. Mavridou**, A. P. Feresidis, P. Gardner and P. S. Hall, "Tunable millimetre-wave phase shifting surfaces using piezoelectric actuators," *IET Microw. Antennas Propag.*, vol.8, no. 11, pp. 829-834, Aug. 2014.

2. Q. Li, A. P. Feresidis, **M. Mavridou**, and P. S. Hall, "Miniaturized Double-Layer EBG Structures for Broadband Mutual Coupling Reduction Between UWB Monopoles," *IEEE Trans. Antennas and Propag.*, vol. 63, no. 3, pp. 1168–1171, March 2015.

3. **M. Mavridou**, A. P. Feresidis, P. Gardner, "Tunable Double-Layer EBG Structures and Application to Antenna Isolation", *IEEE Trans. Antennas and Propag.,* accepted, publication pending.

4. **M. Mavridou**, K. Konstantinidis, A. P. Feresidis, "Continuously Tunable mm-Wave High Impedance Surface," *IEEE Antennas and Wireless Propag. Lett.*, submitted.

5. **M. Mavridou**, A. P. Feresidis, "Dynamically Reconfigurable High Impedance and Frequency Selective Meta-Surfaces", *IEEE Trans. Antennas and Propag.*, submitted.

International conferences:

1. **M. Mavridou**, A. P. Feresidis, P. Gardner, P. S. Hall, "Tunable defected ground slits for mutual coupling reduction applications," *Antennas and Propagation Conference (LAPC)*, 2012 Loughborough, UK.

2. P. Gardner, A. P. Feresidis, P. S. Hall, T. J. Jackson, O. Tade, **M. Mavridou**, Y. Kabiri, X. Gao, "Frequency reconfiguration in single and dual antenna modules," *7th European Conference on Antennas and Propagation*, Gothenburg, Sweden, Apr. 8-12, 2013.

3. **M. Mavridou**, A. P. Feresidis, P. Gardner, P. S. Hall, "Tunable Electromagnetic Band Gap Slits for Mutual Coupling Reduction", *European Microwave Week 2013*, Nuremberg, Germany, October 6-11, 2013.

4. **M. Mavridou**, A. P. Feresidis, P. Gardner, "Tuning Periodic Surfaces with Piezoelectric Actuators", *8ᵗʰ European Conference on Antennas and Propagation*, The Hague, Netherlands, Apr. 6-11, 2014.

5. **M. Mavridou**, A. P. Feresidis, "A new class of tunable multi-layer meta-surfaces", *8th International Congress on Advanced Electromagnetic Materials in Microwaves and Optics – Metamaterials 2014* Copenhagen, Denmark, 25-30 August 2014.

6. **M. Mavridou**, A. P. Feresidis, P. Gardner, "A New Technique for Tuning Millimetre-Wave Artificial Impedance Surfaces", *Antennas and Propagation Conference (LAPC)*, 2014 Loughborough, UK.

7. **M. Mavridou**, A. P. Feresidis, P. Gardner, "A Report on Tuning mm-Wave Periodic Structures with Piezoelectric Actuators", *IET 2nd Annual Active and Passive RF Devices Seminar*, Birmingham, UK, 29 October 2014.

8. **M. Mavridou**, K. Konstantinidis, A. P. Feresidis, P. Gardner, "Reconfigurable Beams from Millimetre-Wave Leaky-Wave Antennas", *9ᵗʰ European Conference on Antennas and Propagation*, Lisbon, Portugal, Apr. 12-17, 2015.

9. **M. Mavridou**, A. P. Feresidis, P. Gardner, "Tunable mm-Wave Artificial Impedance Surfaces Using Piezoelectric Bender Actuators", *9ᵗʰ European Conference on Antennas and Propagation*, Lisbon, Portugal, Apr. 12-17, 2015.

Contents

CHAPTER 1.

INTRODUCTION

1.1 BACKGROUND

1.1.1 Metamaterials and Meta-surfaces

Metamaterials are artificial periodic structures that exhibit electromagnetic properties which are not available in nature, such as negative [1] or near-zero refractive index [2]. Due to these extraordinary properties, they have attracted a lot of research interest recently for cloaking [3], super-reflection [4] tunnelling [5] and other applications. Moreover, it has been demostrated that metamaterial structures have the ability to enhance the performance or reduce the size of antennas and other microwave devices exploiting some of their unique EM properties [6-9]. Meta-surfaces are typically 2-dimensional metamaterial structures [10, 11] formed by periodic arrays of metallic elements printed on dielectric substrates or apertures etched off metallic sheets. A periodic surface can be characterized as a meta-surface if it consists of unit cells with sub-wavelength dimensions and exhibits extraordinary electromagnetic properties.

Electromagnetic Band-Gap (EBG) structures are a type of metamaterials that have the property of prohibiting electromagnetic wave propagation within a specific frequency band [12]. Initially, Photonic Band-Gap (PGB) structures were investigated which prohibit electromagnetic wave propagation in the optical region. These structures consist in photonic crystals, i.e. periodic arrangements of high dielectric constant cavities in a low dielectric region. PGBs were then scaled to lower frequencies for applications in the microwave and millimetre-wave frequency regimes in which case the term EBGs was coined [12-15]. Various

implementations of EBG structures have been reported. Some typical implementations consist of periodic arrays of metallic elements, such as dipoles, printed on dielectric substrates [16-19] as well as arrays of aperture type elements etched off a metallic screen [20].

EBGs have been extensively employed to suppress surface waves (and thus also surface currents) [15, 17, 21]. Due to this characteristic they can be applied to achieve directivity improvement for a single antenna [15] and isolation enhancement between the elements of an antenna array [22-23]. A typical S_{21} response of an EBG structure can be seen in Fig. 1.1.1, which shows the measured S_{21} for surface wave propagation along a square patch array for transverse electric (TE) and transverse magnetic (TM) waves. The common band-gap region of the TE and TM modes is shaded [18].
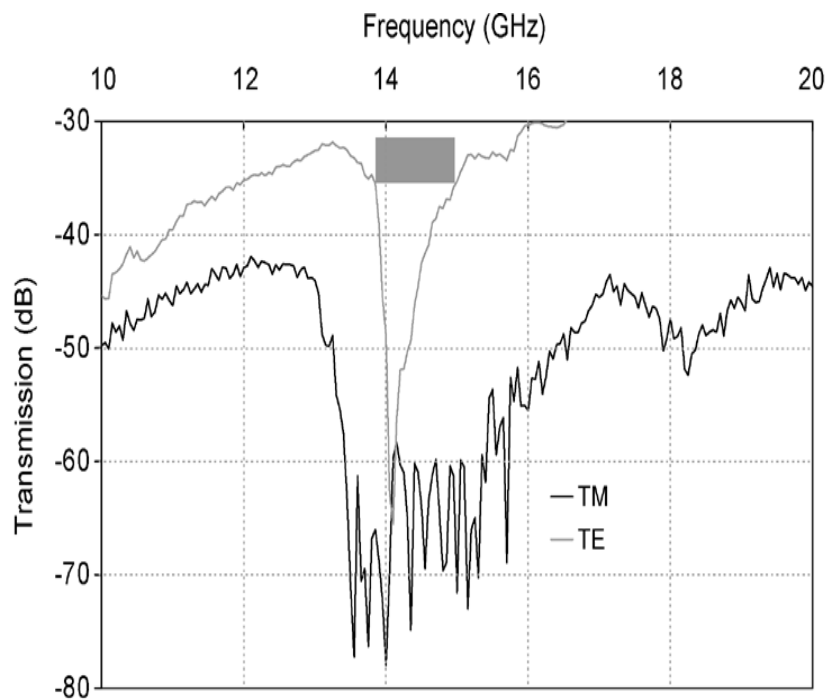
Fig. 1.1.1   Typical response of a square patch EBG array (taken from [18]).

Frequency Selective Surfaces (FSS) are two-dimensional metamaterial structures formed from periodic arrays of metallic elements printed on dielectric substrates or apertures in

metallic contacting planes. As their name suggests, they selectively allow electromagnetic waves to pass through them, depending on their frequency. More specifically, they exhibit stop-band and pass-band characteristics when illuminated by an electromagnetic wave with an arbitrary angle of incidence. If the angle of incidence becomes 90°, then there is surface wave propagation and hence in this case the structure can be approached as an EBG structure [24, 25].

The geometry of the elements can vary from simple square or dipole elements to more complicated shapes such as Jerusalem crosses, spirals, loops and many others. Depending on the geometry and the separation of the elements, different reflection and transmission characteristics are obtained. In the case of conducting periodic elements, a stop-band region is created (i.e. high reflection coefficient) at the FSS resonance (which is related to the resonant frequency of the metallic elements), while at other frequencies, the FSS is completely transparent. Similarly, aperture FSSs, exhibit a pass-band region with full reflection at frequencies away from the resonance [24, 25]. As an example, the reflection and transmission response of a square aperture FSS is depicted in Fig. 1.1.2. In addition, in complementary arrays, i.e. arrays with elements of the same shape such that if the two arrays are put on top of each other, a complete perfectly conducting plane is obtained (Fig. 1.1.3), the reflection coefficient of the conducting array is equal to the transmission coefficient of the aperture array and vice versa, assuming that there is no dielectric substrate (free-standing FSSs).

The frequency selectivity they exhibit makes FSS eligible for applications like microwave filters [24-26], beam splitters [27], multi-band reflectors [28] and arrays [29], radomes [30] or absorbers [31]. In addition, they have been extensively studied for applications in antenna systems [32, 33]. Moreover, FSSs can also be operated as Partially Reflective Surfaces (PRS)

at frequencies near the resonance, which is useful in certain applications such as Fabry-Perot type antennas [34-37].
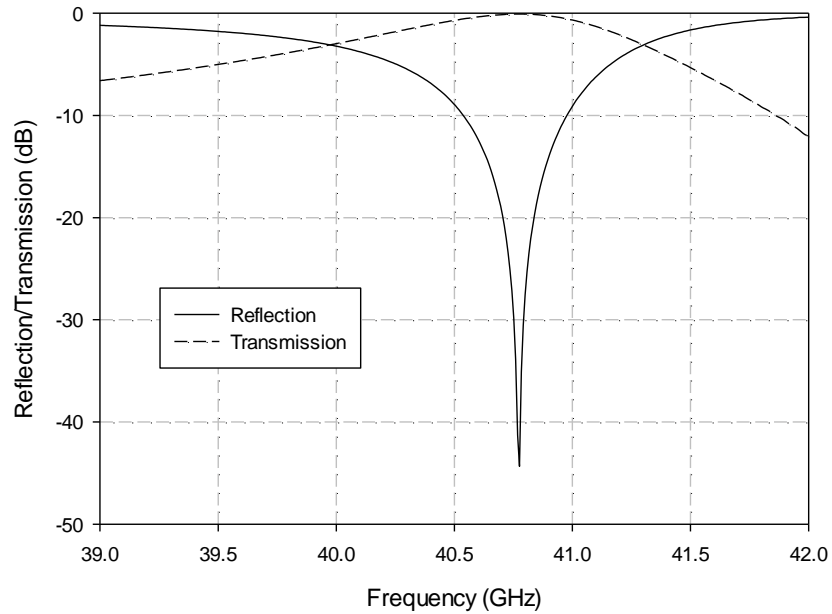
Fig. 1.1.2   Reflection and transmission response of a square aperture FSS array.

(a)   (b)
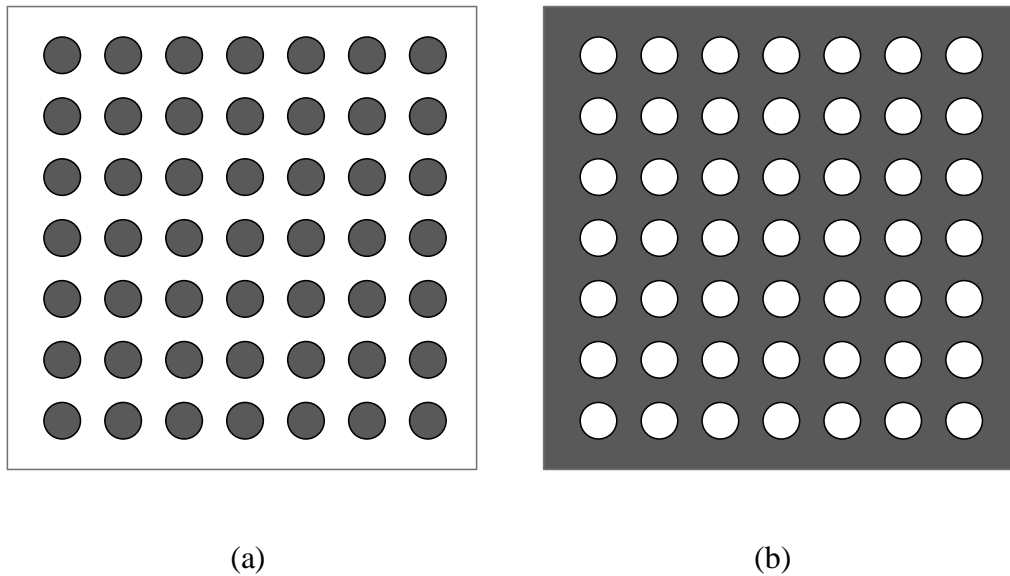
Fig. 1.1.3   Example of complementary FSS arrays, (a) circular patches array and (b) circular apertures array.

If a FSS is placed at close proximity over a ground plane, or is printed on a grounded dielectric substrate, it acts as a **High Impedance Surface (HIS)** [21]. High Impedance Surfaces (HIS) have been extensively investigated for their property to provide an engineered reflection phase for impinging electromagnetic waves [18, 21, 36-43]. They exhibit full reflection with a reflection phase of zero at a specific frequency, acting as an Artificial Magnetic Conductor (AMC). Thus, in such structures the magnetic field tangential to the surface vanishes for a range of frequencies. They are complementary to Perfect Electric Conductors (PEC) which introduce a phase shift of 180° to the reflected plane waves.

HISs were introduced by Sievenpiper [21], who proposed mushroom-type metallic elements in a 2-D periodic arrangement printed on a grounded dielectric substrate. An understanding of the structure's geometry can be realized through Fig. 1.1.4 and it essentially consists of metallic patches connected to the ground plane through vias. Later on, it has been proven that a HIS response can be achieved without the need of vias [36-40] which complicate the fabrication, especially at higher frequencies. A typical HIS response is presented in Fig. 1.1.5 corresponding to a structure with an AMC operation at 56.6GHz. As useful bandwidth in AMC structures is considered the range of frequencies where the reflection phase is between -90° and $+90^o$ (shaded in the figure). However, HISs can also be operated at various reflection phase values for different applications. They can be applied as ground planes in printed [21] or in cavity antennas for profile reduction [36, 37], but they have also been employed for their phase shifting properties in applications such as relfectarrays [41], polarisation converters [42], holographic surfaces [43] etc.

(a)   (b)

Fig. 1.1.4   Mushroom-type HIS structure, (a) front view, (b) cross section.
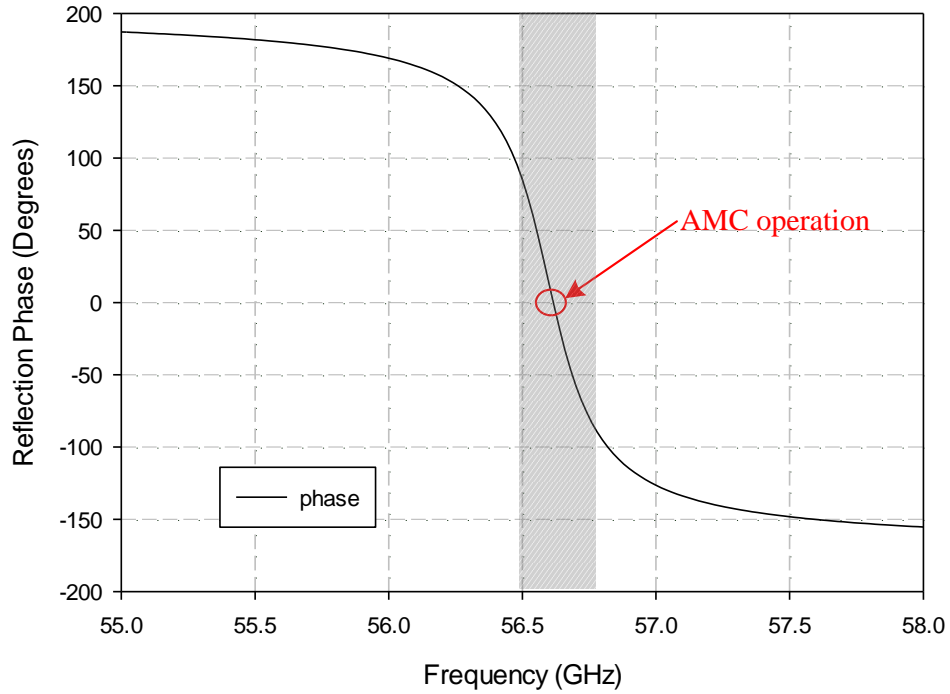
Fig. 1.1.5   Reflection phase response of a square loop element HIS array.

1.1.2 Overview of Tuning Techniques for Metamaterial Structures

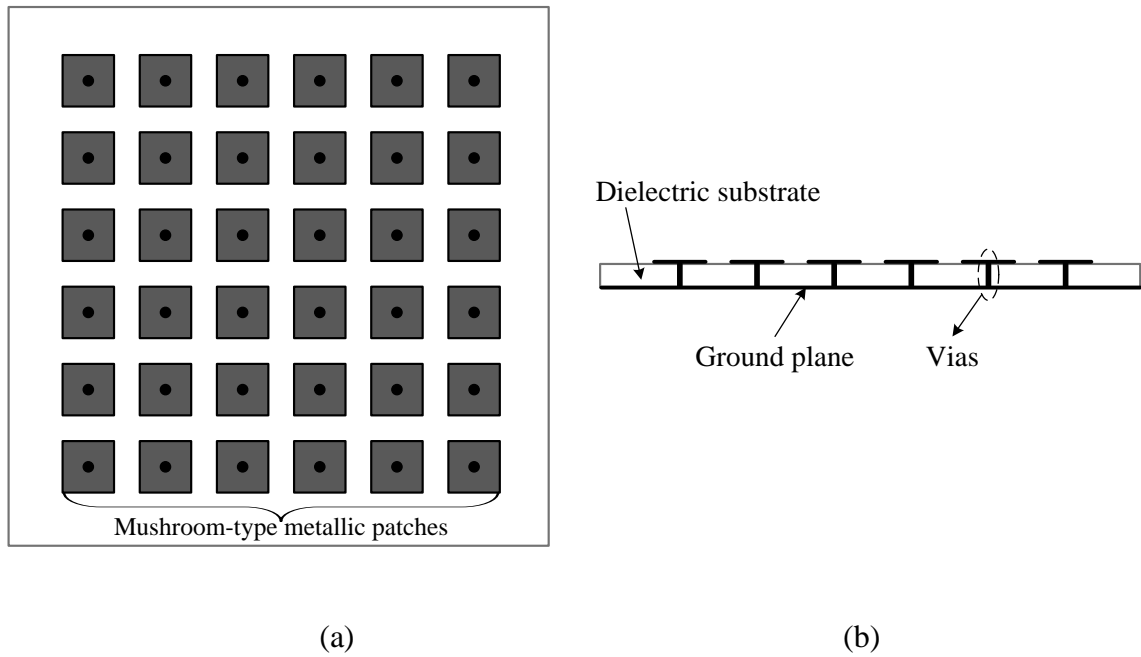As mentioned in the previous section, the resonant frequency of a FSS depends on the shape of the elements, their separation, the geometry and the dielectric constant and thickness of the supporting material. Similarly, the different geometrical parameters, as well as the substrate type and thickness, affect the response of EBG and HIS structures. The reconfiguration of the response of these structures is an important characteristic for a number of applications such as reconfigurable antennas in terms of frequency [44] or pointing angle of the main beam [45], and tunable filters [46]. These are required for varying environment applications, like multi-band communication systems or cognitive radios [47].

In order to be able to reconfigure this response, various tuning techniques for metamaterial structures have been investigated. These tuning techniques can be classified in two categories. Namely, tuning based on **tunable components**, and tuning based on **tunable materials**. **Tunable** or active **components** can be solid state components such as varactor [44-46, 48] or PIN diodes [49], or Radiofrequency Micro-Electro-Mechanical Systems (RF MEMS) [50-54]. These are incorporated in the structure to physically or effectively change one of the periodic array geometrical parameters. More specifically, varactor diodes are employed to change the capacitance of the conductive elements forming the structure. Generally, periodic elements correspond to an equivalent capacitance and/or inductance depending on their size and shape. Thus, adding a variable capacitance to each element results in a change of its electrical length. This way, a dynamic control of the frequency response can be achieved [44-46, 48]. On the other hand, PIN diodes act as switches that are employed to actively change the shape or size of the array's elements [49]. Both techniques require external biasing either to dynamically change the capacitance or to switch ON and OFF the varactor or PIN diode respectively. Switching time is low in these components so they are employed in low frequency

(microwave regime) applications. Moreover, their use is prohibitive in higher microwave frequencies because they exhibit high losses, parasitic effects and non-linearities.

Furthermore, there are various types of Micro-Electro-Mechanical Systems (MEMS) such as MEMS varactors or MEMS switches which can be employed the same way as the corresponding solid state components, but with better performance for higher frequencies [50, 53, 54]. Nevertheless, there are also MEMS that can provide electromechanical actuation and thus can be used for tuning since an appropriate micro–actuator can be employed to mechanically (i.e. physically) change the size, shape, spacing and orientation of the metamaterial structure elements as well as the distance between two layers (either two layers of arrays or an array layer and the ground plane), and have shown promising results [51, 52]. However, typically in order to obtain tuning, a MEMS component has to be integrated to each element of the periodic structure. This implies an upper frequency limit for the suitability of this technology (30GHz–90GHz [50, 51, 53, 54]), as the dimensions of the periodic elements decrease with the frequency, impeding the incorporation of an electrically large component in the unit cell of the array. This size restriction is mainly caused from the packaging of such components. Fully integrated ones would occupy less space and hence could be suitable for higher frequencies. For example, in [51], magnetic MEMS have been employed acting as the dipoles that form the periodic array of a FSS. The particular MEMS/dipoles are tilted to an angle when a magnetic field is applied. By doing this, the dipole's effective length (i.e. its projected length on the substrate's surface) decreases with the angle, and so the resonant frequency increases. A different approach is presented in [52] where only one MEMS structure comprising a movable membrane is employed and proposed for THz frequencies. The membrane is supported by four anchored flexure arms which can be pulled down if a voltage difference is applied between the top and bottom electrodes. This results in a vertical

8

and homogeneous displacement of the membrane. At high frequencies the size of elements is very small, and it decreases as the frequency increases. Consequently, at THz frequencies an array of periodic elements can be integrated on the movable MEMS membrane [52]. This structure can consist of either two layers of periodic arrays, or a layer of arrays and a metallic ground plane. With the external voltage the air gap between the two layers can be controlled, resulting in a variation of the electromagnetic coupling between the two layers. Therefore this approach can be used to tune the resonant frequency, the bandwidth and other parameters.

Finally, **tunable materials** such as ferroelectric substrates [55] at lower microwave frequencies and more recently liquid crystals [56-58] and graphene [59, 60] at higher millimetre-wave frequencies have been investigated producing promising results. These tuning techniques are essentially based on changing the properties of the material, by applying an electric or magnetic field. This in turn changes the frequency response of the structure since it alters the guided wavelength and hence the resonance frequency. For example, nematic liquid crystals (LCs) possess a voltage dependant dielectric anisotropy. In the unbiased state the liquid crystal molecules are oriented horizontally (i.e. parallel to the surface of the periodic array if the LC is used as a substrate) while by applying a voltage the molecules rotate, becoming vertical (i.e. perpendicular to the periodic surface) at a certain voltage value. The electric permittivity of the LC therefore varies between two values $\varepsilon_{//}$ and $\varepsilon_{\perp}$, for the unbiased and biased state respectively. This property has been extensively exploited to obtain tunable metamaterial structures [56-58]. Similar concepts apply in ferroelectric substrates. Graphene on the other hand is a material with variable complex conductivity under electric-field biasing. Thus, it has been employed to fabricate the conductive elements of periodic structures and not the substrate [59, 60]. The main

disadvantage of these tuning techniques is that they exhibit high losses and very low switching speeds in the case of liquid crystals [58].

1.2 MOTIVATION AND OBJECTIVES

In section 1.1, a brief description of EBG, FSS and HIS metamaterial structures has been carried out, along with an overview of existing tuning techniques for such structures. It is evident that significant amount of work has been already carried out concerning tunable metamaterials, since the latter can be applied in numerous applications such as frequency reconfigurable [44] or beam-scanning antennas [44, 45], tunable filters [46, 49-51, 55, 56], or reflectarrays [53, 54, 57-60]. However, there are still many challenges that need to be dealt with depending on the frequency regime. More specifically, varactor and PIN diodes have been successfully employed for low microwave frequencies but require complex biasing networks. This is caused by the fact that a tunable component has to be incorporated to each of the elements which form the periodic structure. Subsequently, due to the increased number of elements and thus of tunable components biasing is highly non-trivial.

Furthermore, as the frequency increases, the use of semiconductor based components becomes prohibitive, so alternative tuning techniques have to be considered such as MEMS and liquid crystals. Similarly to the other tunable components, multiple MEMS need to be employed, integrated to the individual elements, which also implies a complexity in the design in terms of the biasing network, but furthermore it imposes an upper limit at the frequency of operation due to the size of the MEMS as explained in the previous section. Liquid crystals on the other hand are more appropriate for high millimetre-wave and submillimetre-wave frequencies but exhibit low switching speeds and high losses. Thus, **the motivation of this PhD thesis is to investigate and propose novel designs of metamaterial structures and introduce novel techniques and configurations for tuning metamaterials**

that overcome the aforementioned challenges. This could greatly benefit antenna designs based on periodic surfaces and generally communication systems in terms of flexibility and efficiency, while it could offer the possibility to expand the functionality of traditional metamaterial structures at high frequencies (THz). For this reason **another objective of this thesis is to explore possible applications of tunable metamaterials in communication systems**.

Initially, novel biasing techniques for varactor diodes are investigated for tuning EBG structures operating at low frequencies (3GHz to 6GHz). The application of tunable EBG structures for isolation enhancement of closely spaced passive and novel reconfigurable antennas in MIMO systems is also investigated. Additionally, a new low-loss technique of tuning HIS structures is investigated, as an effort to address the issue of excessive losses and parasitic effects of tuning techniques employed thus far for the realization of tunable HISs. The technique is based on employing two types of piezoelectric actuators, each type being suitable to a different frequency band. Particularly, bender piezoelectric actuators are used for configurations operating at low mm-wave frequencies (~15GHz) and stack multilayer actuators for operation at higher mm-wave frequencies (60GHz) where achieving a low loss performance is even more challenging. Moreover, this tuning technique achieves significantly improved switching speeds compared to LCs or ferroelectrics. The incorporation of both tunable HIS structures in tunable antenna designs is studied. Finally, tunable FSS are introduced making several design considerations in order to propose novel configurations and to exploit the concept of piezoelectric actuators to obtain a tunable response. Again, this is carried out for two operating bands, 15GHz and 60GHz. The particular designs of tunable HIS and FSS, are directly scalable to even higher frequencies (THz), while having addressed the issue of high losses and low switching speed, offering a promising solution at this band.

1.3 OUTLINE OF CHAPTERS

This PhD thesis is focused on tunable metamaterial structures and their applications for microwave and millimetre-wave frequencies. In total it is organized in seven chapters. In this Chapter, an introduction to the background of the thesis has been carried out, along with a description of the motivation of this research.

In Chapter 2, the theoretical background on which the work in this thesis is based is described. Various tools have been employed in order to analyze the three investigated types of metamaterials, EBG, FSS and HIS structures. More specifically dispersion analysis of surface waves is explained for EBGs, while a ray optics theory approach is adopted and analyzed for FSS and HIS. In addition, a brief description of the operation of Leaky Wave Antennas (LWA) is included in the Chapter, since a tunable LWA is proposed later on in Chapter 5. Subsequently, full-wave periodic analysis based on Floquet theorem is described which is employed to characterize periodic structures since it has the advantage of analyzing just the unit cell instead of the complete structure, giving useful insight for the behaviour of the structures under investigation. Finally, the operation of varactor diodes and piezoelectric actuators, which are the tuning components employed to tune different types of metamaterial structures, is explained in order to provide an initial understanding of the proposed tuning techniques throughout this PhD thesis.

Chapter 3 is devoted to the analysis and design of tunable EBG structures based on varactor diodes with simplified biasing configuration. Initially simulated results are presented, performed to evaluate the tunability of the structures, and then measurements of fabricated prototypes are provided validating the concept. Subsequently, the proposed tunable EBGs are employed to improve the isolation of closely spaced antennas for MIMO systems. Simulation

and measurements are presented and explained. Finally, the concept is extended using tunable monopole antennas. A novel tunable monopole antenna is introduced. Then, two same antennas are incorporated with the tunable EBG structures, achieving high isolation across their tuning range. The proposed EBGs and antennas are designed to operate at frequencies from 3GHz to 6GHz.

In Chapter 4, designs of tunable HIS are studied for low millimetre-wave frequencies. Tuning of the proposed HIS structures is based on bender piezoelectric actuators. These are employed to produce a displacement when voltage is applied to them, and hence change the cavity distance between the two layers forming the structure, i.e. the ground plane and the periodic array placed at a small distance above it. This results in a change of the reflection phase response of the structure. The first two designs that are being investigated exhibit a single resonance (at a specific state of the actuators), which is around 15GHz for the first HIS structure and around 30GHz for the second. The third design that is presented, is multi-resonant, resulting in a broadband HIS operating at 15GHz. This is also tuned using the same tuning technique. The tunability of the structures has been evaluated extracting their reflection characteristics through full wave periodic analysis carried out in 3D electromagnetic simulation software. Simulation results demonstrate that the proposed configurations can be employed as dynamic impedance surfaces obtaining significant phase shift with a low-loss performance. Moreover, measurements are presented for the first design validating the simulated results. Finally, as a practical application, a dipole antenna is presented, placed above the proposed tunable HIS, obtaining a significant tuning of its operational frequency.

In Chapter 5, a tunable HIS for higher mm-wave frequencies is investigated. The HIS consists of a periodic surface placed over a ground plane creating an air cavity. Initially, the HIS design is optimized in order to obtain a fast variation of the reflection phase with

frequency, making the proposed HIS very sensitive to small changes of the cavity thickness. The tuning technique employed in this Chapter is similar with the one introduced in Chapter 4. However in this Chapter the tuning is obtained by virtue of compact stack multi-layer piezoelectric actuators that produce a small displacement between the two layers, when voltage is applied to them. Thus, this technique is more appropriate for the targeted frequency band, since due to the reduced dimensions at higher frequencies, a smaller displacement is required to dynamically change the reflection phase response of the structure. Simulated and measured results are presented, achieving a phase shift of over 200 degrees at about 60GHz. In addition, a losses evaluation is performed. Finally, a continuous beam steered antenna application is proposed based on a 1D hollow Leaky-Wave Antenna (LWA) formed by a Partially Reflective Surface (PRS) placed on top of the proposed tunable HIS.

Chapter 6 is focused on tunable FSS structures applying the same tuning techniques as the ones described in Chapters 4 and 5. Initially, a novel design of multi-layer Frequency Selective Meta-Surfaces (FSmS) is presented achieving significant tuning of the pass-band response with low losses, operating at low mm-wave frequencies. In contrast to conventional FSS, the proposed FSmS consist of multiple layers of non-resonant sub-wavelength periodic meta-surfaces. In particular, a periodic array of square loop elements is placed between two periodic arrays of square apertures on metallic sheets, separated by thin sub-wavelength air cavities. The combination of the square loop array and one square aperture array produces a HIS response. This response is tuned using the piezoelectric actuators by changing the distance between the two surfaces which in turn alters the resonance condition of the complete structure and thus the central frequency of the pass-band. Subsequently, the design and tunability of the proposed FSmS is presented and compared with an alternative design. The angular stability is also studied and discussed. Simulation and measurement results are

presented validating the proposed concept. Finally, a tunable FSS for higher mm-wave frequencies consisting of two square aperture arrays printed on dielectric substrates and separated by an air cavity is investigated. Tuning of the band-pass filter response of the double layer FSS is achieved by means the stack piezoelectric actuators positioned around the surfaces. The proposed actuators dynamically change the thickness of the air cavity, due to their property of expanding vertically under DC biasing, which results in tuning the transmission characteristics of the structure.

Finally, in Chapter 7 the conclusions and main contribution of this PhD thesis are presented. Moreover, possible future work is discussed.

REFERENCES

[1] S. Zhang, W. Fan, N. C. Panoiu, K. J. Malloy, R. M. Osgood, and S. R. Brueck, "Experimental demonstration of near-infrared negative index metamaterials," *Phys. Rev. Lett.*, 95, 1374041, (2005).

[2] P. Moitra, Y. Yang, Z. Anderson, I. Kravchenko, D. Briggs, and J. Valentine, "Realization of an all-dielectric zero-index optical metamaterial," *Nature Photonics*, 7, 791-795, (2013).

[3] T. Ergin, N. Stenger, P. Brenner, J. B. Pendry, and M. Wegener, "Three-dimensional invisibility cloak at optical wavelengths," *Science* 328, 337, (2010).

[4] J. Hao, W. Yan, and M. Qiu, "Super-reflection and cloaking based on zero index metamaterial," *Appl. Phys. Lett.*, 96, 101109, (2010).

[5] M. Silveirinha and N. Engheta, "Tunneling of electromagnetic energy through subwavelength channels and bends using ε-near-zero materials," *Phys. Rev. Lett.*, 97**,** 157403, (2006).

[6] R. W. Ziolkowski and A. Erentok, "Metamaterial-based efficient electrically small antennas," *IEEE Trans. Antennas Propag.*, vol. 54, no. 7, pp. 2113–2130, Jul. 2006.

[7] M. Anioniades and G. V. Eleftheriades, "Compact linear lead/lag metamaterial phase shifters for broadband applications," *IEEE Antennas Wireless Propag. Lett.*, vol. 2, no. 7, pp. 103–106, Jul. 2003.

[8] C. Caloz and T. Itoh, Electromagnetic Metamaterials: Transmission Line Theory and Microwave Applications. New York: Wiley, 2004.

[9] C. Caloz, and T. Itoh, "Transmission line approach of left- handed (LH) materials and microstrip implementation of an artificial LH transmission line," *IEEE Trans. Antennas Propag.*, vol.52, no.5, pp.1159-1166, May 2004.

[10]   F. Falcone, T. Lopetegi, M. A. G. Laso, J. D. Baena, J. Bonache, M. Beruete, R. Marqués, F. Martín, and M. Sorolla, "Babinet principle applied to the design of metasurfaces and metamaterials," *Phys. Rev. Lett.*, vol. 93, pp. 197401(1)-197401(4), Nov. 2004.

[11]   N. Yu and F. Capasso, "Flat optics with designer metasurfaces," *Nat. Mat.*, vol. 13, pp. 139-150, Jan. 2014.

[12]   L. Brillouin, *Wave Propagation in Periodic Structures; Electric Filters and Crystal Lattices*, 2nd ed. New York: Dover, 1953.

[13]   A. Harvey, "Periodic and guiding structures at microwave frequencies," *IRE Trans. Microwave Theory Tech.*, vol. 8, pp. 30–61, June 1959.

[14]   M. Sigalas, C. Chan, K.-M. Ho, and C. Soukoulis, "Metallic photonic band-gap materials," *Phys. Rev. B, Condens. Matter*, vol. 52, pp. 11744–11751, 1995.

[15]   R. Gonzalo, P. de Maagt, and M. Sorolla, "Enhanced patch antenna performance by suppressing surface waves using photonic bandgap substrates," *IEEE Trans. Microwave Theory Tech.*, vol. 47, pp. 2131–2138, Nov. 1999.

[16]   A. S. Barlevy and Y. Rahmat-Samii, "Characterization of electromagnetic band-gaps composed of multiple periodic tripods with interconnecting vias: Concept, analysis, and design," *IEEE Trans. Antennas Propagat.*, vol. 49, pp. 343–353, Mar. 2001.

[17]   A. P. Feresidis, G. Apostolopoulos, N. Serfas and J. C. Vardaxoglou, "Closely coupled metallodielectric electromagnetic band-gap structures formed by double-layer dipole and tripole arrays," *IEEE Trans. Antennas Propagat.*, vol. 52, no. 5, pp. 1149-1158, May 2004.

[18]   G. Goussetis, A. Feresidis and J. Vardaxoglou, "Tailoring the AMC and EBG characteristics of periodic metallic arrays printed on grounded dielectric substrate," *IEEE Trans. Antennas Propagat.*, vol. 54, no. 1, pp. 82-89, Jan. 2006.

[19]   Y. R. Lee, A. Charaya, D. S. Lockyer, and J. C. Vardaxoglou, "Dipole and tripole metallodielectric photonic bandgap (MPBG) structures for microwave filter and antenna applications," *Proc. Inst. Elect. Eng. Optoelectron.*, vol. 127, pp. 395–400, Dec. 2000.

[20]   P. De Maagt, R. Gonzalo, J. C. Vardaxoglou, and J. M. Baracco, "Photonic bandgap antennas and components for microwave and (sub)millimeter wave applications," *IEEE Trans. Antennas Propag., Special Issue on Metamaterials*, vol. 51, no. 10, pp. 2667-2677, Oct. 2003.

[21]   D. Sievenpiper, L. Zhang, R. F. J. Broas, N. G. Alexopolous, and E. Yablonovitch, "High-impedance electromagnetic surfaces with a forbidden frequency," *IEEE Trans. Microw. Theory Tech.*, vol. 47, no. 11, pp. 2059–2074, Nov. 1999.

[22]   F. Yang, and Y. Rahmat-Samii, "Microstrip antennas integrated with electromagnetic band-gap (EBG) structures: a low mutual coupling design for array applications," *IEEE Trans. Antennas Propagat.*, vol. 51, pp. 2936-2944, Oct. 2003.

[23]   E. Rajo-Iglesias, O. Quevedo-Teruel, L. Inclan-Sanchez, "Mutual coupling reduction in patch antenna arrays by using a planar EBG structure and a multilayer dielectric substrate," *IEEE Trans. Antennas Propagat.*, vol. 56, no. 6, pp. 1648-1655, Jun. 2008.

[24]   J. C. Vardaxoglou, *Frequency selective Surfaces: Analysis and Design.*, vol. 10, Taunton: Research Studies, 1997.

[25]   B. A. Munk, *Frequency Selective Surfaces: Theory and Design.* Wiley − Interscience, 2005.

[26]   R. Mittra, C. H. Chan, and T. Cwik, "Techniques for analyzing frequency selective surfaces-a review," Proc. IEEE, vol. 76, pp. 593–615, Dec. 1988.

[27]   R. Ulrich, "Far-infrared Properties of Metallic Mesh and its Complementary Structure", *Infrared Physics*, vol. 7, pp.37-55, 1967.

[28]   V. D. Agrawal, and F.A. Pelow, "Design of a Dischroic Casegrain Subreflector", *IEEE Trans. Antennas Propag.,* AP-27, no. 4, pp.466-473, July 1979.

[29]   J. Romeu, and Y. Rahmat-Samii, "Fractal FSS: A Novel Dual-Band Frequency Selective Surface", *IEEE Trans. Antennas and Propag.*, Vol. 48, no. 7, pp. 1097-1105, July 2000.

[30]   C. J. Larson, "Modified Center Layer Metallic Biplanar Radome Design", Tech. Rept. AFAL-TR-78-28, Ohio State Univ. ElectroScience Lab. Rept. RF 4346-2, Columbus, March 1978.

[31]   F. C. Seman, R. Cahill, V. F. Fusco, and G. Goussetis, "Design of a Salisbury Screen Absorber Using Frequency Selective Surfaces to Improve Bandwidth and Angular Stability Performance", *IET Microw. Antennas Propag.,* vol. 5, no. 2, pp. 149-156, Jan. 2011.

[32]   Y. Rahmat-Samii and A. N. Tulintseff, "Diffraction analysis of frequency selective reflector antennas," *IEEE Trans. Antennas Propag.*, vol. AP-41, pp. 476–487, Apr. 1993.

[33]   R. Dickie, R. Cahill, H. S. Gamble, V. F. Fusco, A. Schuchinsky, and N. Grant, "Spatial demultiplexing in the sub-mm wave band using multilayer free-standing frequency selective surfaces," *IEEE Trans. Antennas Propag.*, vol. 53, pp. 1903–1911, 2005.

[34]   A. P. Feresidis, and J. C. Vardaxoglou, "High-Gain Planar Antenna Using Optimized Partially Reflective Surfaces", *IEE Proc. Microw. Antennas Propag.*, vol. 148, no. 6, Feb. 2001.

[35]   Y. J. Lee, J. Yeo, R. Mittra, and W. S. Park, "Design of a High-Directivity Electromagnetic Bandgap (EBG) Resonator Antenna Using a Frequency Selective Surface (FSS) Superstrate", *Microwave and Optical Technology Letters*, vol. 43, no. 6, pp. 462-467, Dec. 2004.

[36]   S. Wang, A.P. Feresidis, G. Goussetis, J.C. Vardaxoglou, "Low-Profile Resonant Cavity Antenna with Artificial Magnetic Conductor Ground Plane", *Electron. Lett.*, vol.40, no.7, pp.405,406, 1 April 2004.

[37]   A. P. Feresidis, G. Goussetis, S. Wang, and J. C. Vardaxoglou, "Artificial Magnetic Conductor Surfaces and Their Application to Low-Profile High- Gain Planar Antennas", *IEEE Trans. Antennas Propag.*, vol. 53, no. 1, pp. 209-215, Jan. 2005.

[38]   H. Mosallaei and K. Sarabandi, "Antenna miniaturization and bandwidth enhancement using a reactive impedance substrate," *IEEE Trans. Antennas Propag.*, vol. 52, no. 9, pp. 2403–2414, Sep. 2004.

[39]   Y. E. Erdemli, K. Sertel, R. A. Gilbert, D. E. Wright, and J. L. Volakis, "Frequency-selective surfaces to enhance performance of broad-band reconfigurable arrays," *IEEE Trans. Antennas Propag.*, vol. 50, no. 12, pp. 1716–1724, Dec. 2002.

[40]   Y. Zhang, J. von Hagen, M. Younis, C. Fischer, and W. Wiesbeck, "Planar Artificial Magnetic Conductors and Patch Antennas," *IEEE Trans. Antennas Propag., Special Issue on Metamaterials*, vol. 51, no. 10, pp. 2704–2712, Oct. 2003.

[41]   J. Huang and J. A. Encinar, *Reflectarray antennas.* Hoboken, NJ: Wiley, 2008.

[42]   E. Doumanis, G. Goussetis, J.-L. Gomez-Tornero, R. Cahill, and V. Fusco, "Anisotropic impedance surfaces for linear to circular polarization conversion," *IEEE Trans. Antennas Propag.*, vol. 60, no. 1, pp. 212–219, Jan. 2012.

[43]   B. H. Fong, J. S. Colburn, J. J. Ottusch, J. L. Visher, and D. F. Sievenpiper, "Scalar and tensor holographic artificial impedance surfaces," *IEEE Trans. Antennas and Propag.*, vol. 58, no. 10, pp. 3212–3221, Oct. 2010.

[44]   F. Costa, A. Monorchio, S. Talarico, and F. M. Valeri, "An active high impedance surface for low profile tunable and steerable antennas," *IEEE Antennas Wireless Propagat. Lett.*, vol. 7, pp. 676–680, 2008.

[45]   R. Guzmán-Quirós, J.-L. Gómez-Tornero, A. R. Weily, and Y. J. Guo, "Electronically steerable 1D Fabry-Perot leaky-wave antenna employing a tunable high impedance surface," *IEEE Trans. Antennas Propag.*, vol. 60, no. 11, pp. 5046–5055, Nov. 2012.

[46]   C. Mias, "Varactor-tunable frequency selective surface with resistive-lumped-element biasing grids," *IEEE Microw. Wireless Component Lett.*, vol. 15, no. 9, pp. 570–572, Sep. 2005.

[47]   F. Ghanem, P. S. Hall, and J. R. Kelly, "Two port frequency reconfigurable antenna for cognitive radios," *IET Electron. Lett.*, vol. 45, no. 11, pp. 534–536, May 2009.

[48]   C. Mias and J. H. Yap, "A varactor-tunable high impedance surface with a resistive-lumped-element biasing grid," *IEEE Trans. Antennas Propag.*, vol. 55, no. 7, pp. 1955–1962, Jul. 2007.

[49]   B. Sanz-Izquierdo, E. A. Parker, and J. C. Batchelor, "Switchable frequency selective slot arrays," *IEEE Trans. Antennas Propag.*, vol. 59, no. 7, pp. 2728–2731, Jul. 2011.

[50]   B. Schoenlinner, A. Abbaspour-Tamijani, L. C. Kempel, and G. M. Rebeiz, "Switchable low-loss RF MEMS ka-band frequency-selective surface," *IEEE Trans. Microw. Theory Tech.*, vol. 52, no. 11, pp. 2474–2481, Nov. 2004.

[51]   J. M. Zendejas, J. P. Gianvittorio, Y. Rahmat-Samii, and J. W. Judy, "Magnetic MEMS reconfigurable frequency-selective surfaces," *J. Microelectromech. Syst.*, vol. 15, no. 3, pp. 613–623, Jun. 2006.

[52]   J. S. Fernandez, G. Goussetis, and R. Cheung, "Tunable 2D Electromagnetic Band-Gap (EBG) structures based on Micro-Electro-Mechanical Systems (MEMS) for THz frequencies," *IEEE Antennas and Propagation Society International Symposium (APSURSI)*, pp. 1 – 4, July 2010.

[53] O. Bayraktar, O. Civi, and T. Akin, "Beam switching reflectarray monolithically integrated with RF MEMS switches," *IEEE Trans. Antennas Propag.*, vol. 60, no. 2, pp. 854–862, Feb. 2012.

[54] C. Guclu, J. Perruisseau-Carrier, and O. Civi, "Proof of concept of a dual-band circularly-polarized RF MEMS beam-switching reflectarray," *IEEE Trans. Antennas Propag.*, vol. 60, no. 11, pp. 5451–5455, Nov. 2012.

[55] E. A. Parker, S. B. Savia, "Active frequency selective surfaces with ferroelectric substrates," *Proc. Inst. Elect. Eng. Microwaves, Antennas and Propag.*, vol. 148, pp. 103–108, Apr. 2001.

[56] W. Hu, R. Dickie, R. Cahill, H. Gamble, Y. Ismail, V. Fusco, D. Linton, N. Grant, and S. Rea, "Liquid crystal tunable mm wave frequency selective surface," *IEEE Microw. Wireless Compon. Lett.*, vol. 17, no. 9, pp. 667–669, Sept. 2007.

[57] G. Perez-Palomino, P. Baine, R. Dickie, M. Bain, J. Encinar, R. Cahill, M. Barba, and G. Toso, "Design and experimental validation of liquid crystal-based reconfigurable reflectarray elements with improved bandwidth in F-band," *IEEE Trans. Antennas Propag.*, vol. 61, no. 4, pp. 1704–1713, Apr. 2013.

[58] M. Y. Ismail, W. Hu, R. Cahill, H. S. Gamble, R. Dickie, V. F. Fusco, D. Linton, S. P. Rea and N. Grant, "Performance of reflectarray cells printed on liquid crystal film," presented at the IEEE Asia Pacific Conf. on Electromagn. (APMC-2006), Yokohama, Japan, Dec. 12–15, 2006.

[59] J. Perruisseau-Carrier, "Graphene for antenna applications: Opportunities and challenges from microwaves to THz," in Proc. LAPC, UK, Nov. 2012.

[60] E. Carrasco and J. Perruisseau-Carrier, "Reflectarray antenna at terahertz using graphene," *IEEE Antennas Wireless Propag. Lett.*, vol. 12, pp. 253–256, 2013.

CHAPTER 2.

THEORETICAL BACKGROUND

This Chapter presents the theoretical background on which the work in this thesis is based. Section 2.1 focuses on the three types of periodic surfaces that will be investigated in terms of their tunability later on this thesis, i.e Electromagnetic Band-Gap (EBG) structures, Frequency Selective Surfaces (FSS) (consisting of multiple layers) and High Impedance Surfaces (HIS). EBG metamaterial structures are described based on dispersion analysis of surface waves, while both multi-layer FSS and HIS structures are analysed employing a ray optics theory approach. In addition, a brief description of the operation of Leaky Wave Antennas (LWA) is carried out to provide an understanding of a tunable LWA proposed in Chapter 5. Subsequently, in section 2.2, a description of full-wave periodic analysis is performed. This is the method employed to analyse periodic structures and is based on Floquet theorem. The technique has the advantage of analysing only a unit cell instead of the complete structure, giving useful insight for the behaviour of the structures under investigation and significantly reduces the computational time. Finally, section 2.3 provides a brief explanation of the operation of varactor diodes and piezoelectric actuators which are the tuning components employed to tune different types of metamaterial structures.

2.1 PERIODIC STRUCTURES

Periodic structures are formed by an infinite repetition of a basic building block which is defined as unit cell of the structure. There can be 1-D, 2-D or 3-D periodic structures, produced from the repetition of the unit cell shifted by one, two or three translation vectors respectively. When electromagnetic waves propagate in a periodic structure, the electric and magnetic fields have the same magnitude in all unit cells with an added phase shift in

consecutive unit cells. This can greatly simplify the analysis of such structures, since only one unit cell can be analyzed employing boundary conditions that take into account the phase shift between the unit cells [1]. Often, different types of periodic structures are characterized as metamaterials due to the fact that they exhibit electromagnetic properties which are not available in nature. This thesis focuses in three basic types introduced in Chapter 1 (section 1.1.1), classified according to a specific electromagnetic property.

2.1.1 Electromagnetic Band-Gap (EBG) Structures

As explained in section 1.1, Electromagnetic Band-Gap (EBG) structures are metamaterial structures which exhibit stop-band and pass-band regions for surface waves propagation and thus suppress surface waves in the band-gap regions [2-5]. Surface waves are slow waves. This means that the propagation constant β is greater than the free space wave number k_0 and their phase velocity is smaller than the speed of light. They can occur on the boundary between a metal and free space. Their propagation is bound to the interface, and they decay exponentially into the surrounding materials. They only radiate if there are discontinuities, for example if the medium of propagation is terminated or if the metallic surface is textured with a specific pattern.

An estimation of the band-gap region of a specific EBG topology i.e. the frequency range where no surface wave propagation occurs, can be performed extracting a dispersion diagram. This essentially consists in calculating the value of the propagation constant β within the irreducible Brillouin zone. It can be performed by varying β on the contour of the irreducible zone and determining the frequencies where a mode is supported by the structure [2, 6]. The irreducible Brillouin zone is defined in the reciprocal lattice [2, 6] of the periodic structure after finding all symmetry axes and is the smallest area that if repeated (mirrored at the symmetry axes) will produce the reciprocal lattice. In Fig. 2.2.1, the unit cells of a dipole and

a square patch array are shown with their corresponding reciprocal lattice. The irreducible Brillouin zone is shaded in both examples. For the case of the dipole array with periodicities p_x and p_y along the x and y axis respectively, β should be varied as follows:

ΓX: $\quad 0 \leq \beta_x \leq \pi/p_x$, $\quad \beta_y = 0$

XM: $\quad \beta_x = \pi/p_x$, $\quad 0 \leq \beta_y \leq \pi/p_y$

MK: $\quad 0 \leq \beta_x \leq \pi/p_x$, $\quad \beta_y = \pi/p_y$

$K\Gamma$: $\quad \beta_x = 0$, $\quad 0 \leq \beta_y \leq \pi/p_y$

Similarly, for the square patch array with periodicity p (Fig. 2.1.1b), β is varied along the contour of the irreducible zone:

ΓX: $\quad 0 \leq \beta_x \leq \pi/p$, $\quad \beta_y = 0$

XM: $\quad \beta_x = \pi/p$, $\quad 0 \leq \beta_y \leq \pi/p_y$

$M\Gamma$: $\quad 0 \leq \beta_x \leq \pi/p$, $\quad 0 \leq \beta_y \leq \pi/p$

This procedure will provide information of all the allowed modes in the structure. The regions where no modes are propagating will be the bang-gap regions of the EBG. Usually the light line is also plotted in the dispersion diagram which indicates the propagation of waves in free space. Slow waves are below this line, if fast waves existed they would be located above it. As an example, the dispersion diagram of a square patch array with p=11mm and d=8mm is shown in Fig. 2.1.2. For the particular structure no absolute band-gap occurs as can be seen from the figure.
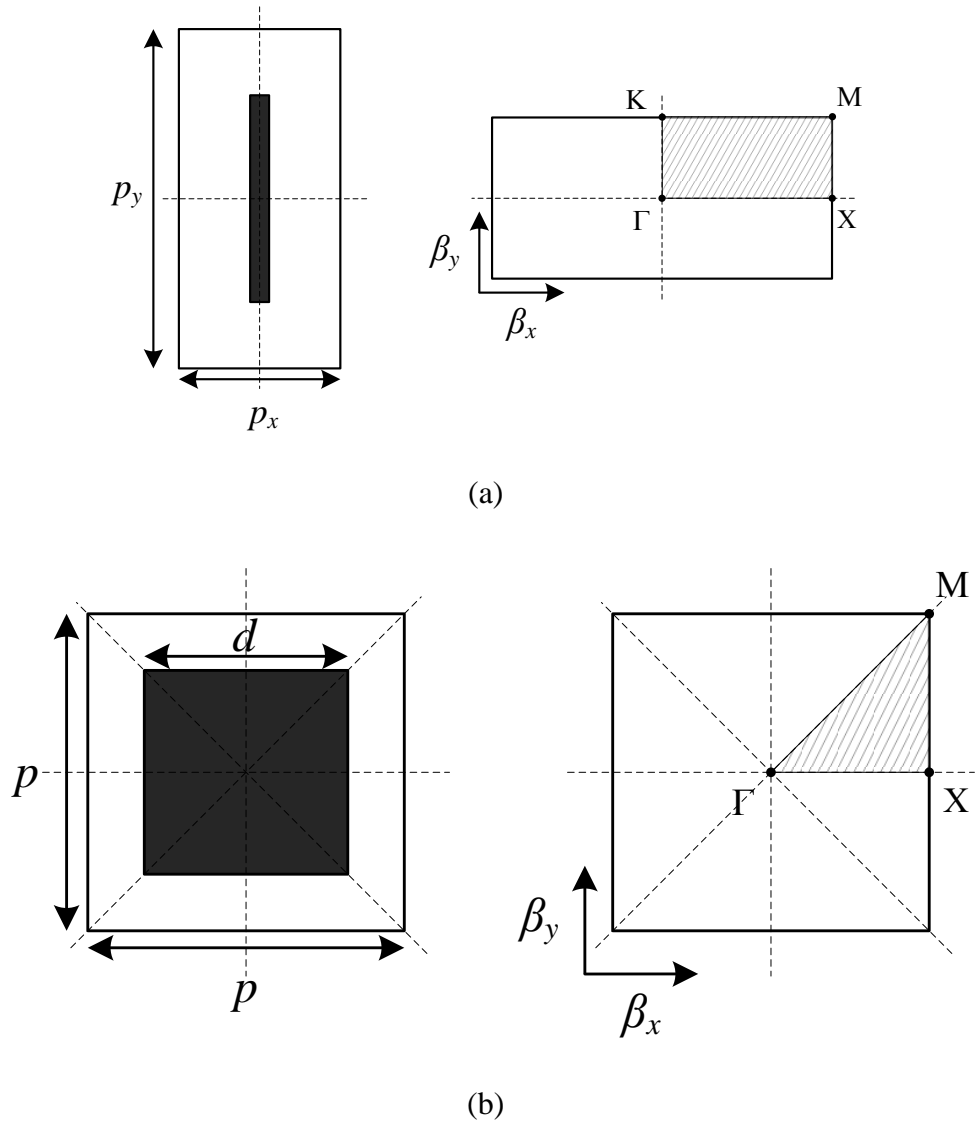
(a)

(b)

Fig. 2.1.1   Examples of unit cells (left) and their corresponding reciprocal lattices with the irreducible Brillouin zones (right). (a) Dipole element array, (b) Square element array.
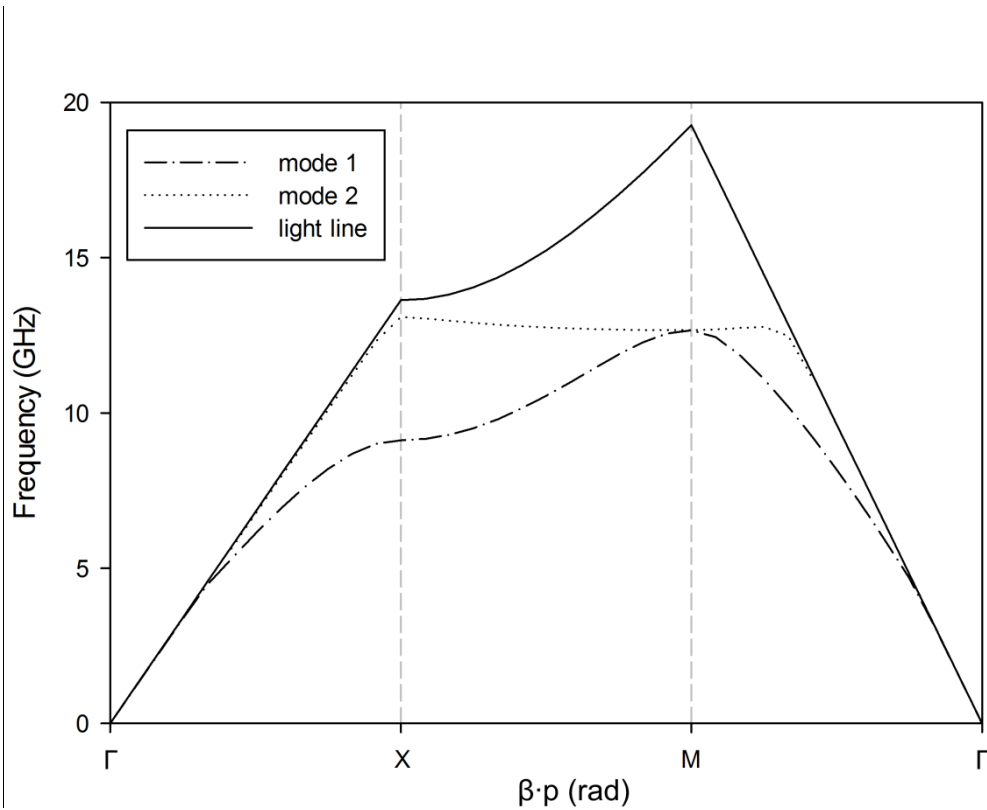
Fig. 2.1.2   Dispersion diagram for square patch array with p=11mm and d=8mm.

2.1.2 Frequency Selective Surfaces (FSS)

Typically the resonant frequency of Frequency Selective Surfaces (FSS) is defined by the dimensions of the periodic elements, their separation and the type and thickness of the substrate, as mentioned in Chapter 1. However, multi-layer FSS are being investigated in this thesis, whose response is not related to the individual FSS resonance but predominantly to a cavity type resonance producing a pass-band response [7].

In order to explain this, let's assume two FSS arrays printed on either sides of a dielectric substrate with thickness S and relative electric permittivity ε_r, as shown in Fig. 2.1.3. The structure can be studied employing ray optics theory, as it resembles a Fabry-Perot interferometer [7]. For a plane wave with an arbitrary angle of incidence θ, in order to obtain

a transmission maximum, the two transmitted rays φ_1 and φ_2 must be in phase, i.e. $\Delta\varphi$ should satisfy:

$$\Delta\varphi = \varphi_1 - \varphi_2 = 2N\pi \text{ , with } N=0,\ 1,\ 2,...$$
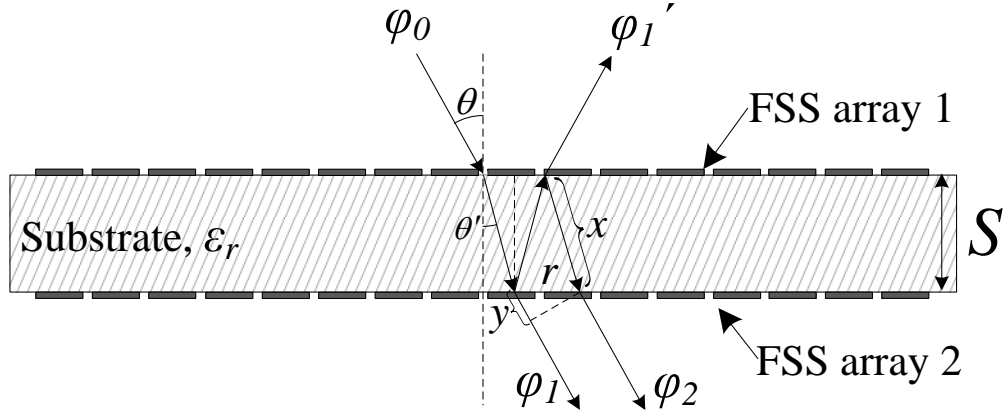
(2.1-1)

Fig. 2.1.3   Schematic diagram of double layer FSS with two arrays printed on either sides of a dielectric substrate.

Taking into account the optical path length that the rays follow due to reflections between the two surfaces and the phase shift introduced by the transmission and reflection at the surfaces, (2.1-1) can be written:

$$2N\pi = \varphi_1 - \varphi_2 = \varphi_{T1} - x\cdot\frac{2\pi}{\lambda_r} + \varphi_{T2} - y\cdot\frac{2\pi}{\lambda} - \left(\varphi_{T1} - 3x\cdot\frac{2\pi}{\lambda_r} + \varphi_{R2} + \varphi_{R1} + \varphi_{T2}\right)$$

$$= 2x\cdot\frac{2\pi}{\lambda_r} - y\cdot\frac{2\pi}{\lambda} - \varphi_{R2} - \varphi_{R1}$$

(2.1-2)

where λ_r is the wavelength in the substrate, φ_{T1} and φ_{T2} the phases of the transmission coefficients and φ_{R1} and φ_{R2} the phases of the reflection coefficients at FSS array 1 and 2 respectively.

From Fig. 2.1.3 it can be extracted that:

$$x = \frac{S}{\cos \theta'}, \quad r = \frac{2\,S \cdot \sin \theta'}{\cos \theta'} \quad \text{and} \quad y = r \cdot \sin \theta = \frac{2\,S \cdot \sin \theta'}{\cos \theta'} \cdot \sin \theta$$

Substituting the above in (2.1-2) we get:

$$2\,N\,\pi = 2\,\frac{S}{\cos \theta'} \cdot \frac{2\,\pi}{\lambda} \cdot \sqrt{\varepsilon_r} - \frac{2\,S \cdot \sin \theta'}{\cos \theta'} \cdot \sin \theta \cdot \frac{2\,\pi}{\lambda} - \varphi_{R2} - \varphi_{R1}$$

$$= \frac{2\,\pi}{\lambda} \cdot 2\,S \left(\frac{\sqrt{\varepsilon_r}}{\cos \theta'} - \frac{\sin^2 \theta}{\sqrt{\varepsilon_r}\,\cos \theta'} \right) - \varphi_{R2} - \varphi_{R1}$$

$$= \frac{2\,\pi}{\lambda} \cdot 2\,S \left(\frac{\varepsilon_r - \sin^2 \theta}{\sqrt{\varepsilon_r}\,\cos \theta'} \right) - \varphi_{R2} - \varphi_{R1}$$

$$= \frac{2\,\pi}{\lambda} \cdot 2\,S \left(\frac{\varepsilon_r - \sin^2 \theta}{\sqrt{\varepsilon_r}\,\sqrt{1 - \sin^2 \theta'}} \right) - \varphi_{R2} - \varphi_{R1}$$

$$= \frac{2\,\pi}{\lambda} \cdot 2\,S \left(\frac{\varepsilon_r - \sin^2 \theta}{\sqrt{\varepsilon_r - \sin^2 \theta}} \right) - \varphi_{R2} - \varphi_{R1}$$

$$2\,N\,\pi = \frac{2\,\pi}{\lambda} \cdot 2\,S \sqrt{\varepsilon_r - \sin^2 \theta} - \varphi_{R2} - \varphi_{R1} \qquad (2.1\text{-}3)$$

Rearranging the resonance condition (2.1-3), the substrate thickness for $N=0$ can be calculated from:

$$S = \frac{\varphi_{R2} + \varphi_{R1}}{4\,\pi\,\sqrt{\varepsilon_r - \sin^2 \theta}} \cdot \lambda \qquad (2.1\text{-}4)$$

In the special case of an air filled cavity, ε_r is equal to 1 and the relations (2.1-3) and (2.1-4) can be simplified to:

$$\frac{2\pi}{\lambda} \cdot 2S \cdot \cos\theta - \varphi_{R2} - \varphi_{R1} = 2N\pi \qquad (2.1\text{-}5)$$

$$S = \frac{\varphi_{R2} + \varphi_{R1}}{4\pi \cdot \cos\theta} \cdot \lambda \qquad (2.1\text{-}6)$$

Moreover, for normal incidence and taking into account that for aperture FSS the reflection phase is close to π, the cavity thickness is approximately half-wavelength. The same can be extracted for conducting arrays who exhibit a reflection phase close to $-\pi$, for $N=2$. As an example of the above analysis, two FSSs with different reflection characteristics are considered, placed at distance $S=2$mm and operating at 15GHz. If the reflection phase of FSS array 1 is $\varphi_{R1}=159.62^{o}$ for normal incidence, (2.1-6) is satisfied for $\varphi_{R2}=-87.62^{o}$. This is in excellent agreement with full-wave simulations, according to which a resonance at 15GHz is obtained with an FSS exhibiting a reflection phase of $\varphi_{R2}=-87.56^{o}$ at this frequency.

2.1.3 High Impedance Surfaces (HIS)

High Impedance Surfaces (HIS) have already been briefly explained in section 1.1. Most of their applications are based on their property of acting as AMC at a specific frequency. However they also behave as EBGs, since they don't support surface waves at certain frequencies, so two distinct phenomena occur which do not necessarily coincide in frequency [8]. The AMC operation of HISs is not related to the resonance of the FSS array but to the resonance of the resonant type cavity formed between the FSS and the ground plane [8, 9]. A schematic diagram of a HIS structure formed by a periodic array printed on a grounded dielectric substrate of thickness t is illustrated in Fig. 2.1.4. The condition to achieve AMC

performance, i.e the resonance condition (2.1-7) is derived from ray optics theory by setting the phase difference between the direct wave φ_0 and reflected wave φ_1 equal to $2N\pi$ [6]. After taking into account the optical path length followed in the cavity, the reflection at the ground plane and the transmission at the periodic array the phase difference $\Delta\varphi$ is given from:

$$\Delta\varphi = \varphi_1 - \varphi_0 = \varphi_T - \frac{2\pi}{\lambda} \cdot t - \pi + \varphi_T - \frac{2\pi}{\lambda} \cdot t - 0$$

$$2\varphi_T - \frac{2\pi}{\lambda} \cdot 2t - \pi = 2N\pi , \text{ with } N=0, 1, 2,... \tag{2.1-7}$$

where φ_T is the phase of the transmission coefficient of the FSS array, λ the wavelength in the propagation medium (dielectric or air) and t the cavity distance.

From (2.1-7) can be seen that the cavity distance (in this case the substrate thickness) t can be calculated from:

$$t = \frac{2\varphi_T - (2N+1)\pi}{4\pi} \cdot \lambda \tag{2.1-8}$$
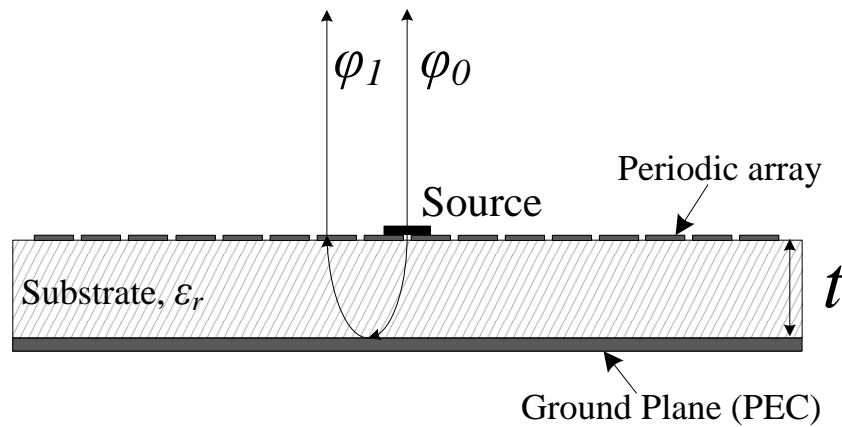
Fig. 2.1.4   Schematic diagram of a High Impedance Surface.

31

2.1.4 Leaky Wave Antennas (LWA)

Leaky Wave Antennas (LWA) are antennas whose operation is based on fast waves produced from surface waves propagating in waveguiding structures due to discontinuities. In contrast to slow waves, the propagation constant β of fast waves, also called leaky waves, is smaller than the free space wave number k_0 and their phase velocity is greater than the one of the light. Moreover, they are characterized by a complex propagation constant [10]:

$$k = \beta - j\alpha \tag{2.1-9}$$

where β is the phase constant and α the attenuation constant.

The attenuation constant, also referred to as leakage rate, is related to the beamwidth of the radiated beam, while the phase constant defines the angle of the beam according to:

$$\sin\theta = \frac{\beta}{k_0} \tag{2.1-10}$$

where θ the angle of the main radiated beam with respect to the normal direction. From (2.1-10) it is evident that in order for radiation to occur, $\beta \leq k_0$ should be satisfied, since from trigonometry $\sin\theta \leq 1$.

Leaky Wave Antennas have attracted a lot of interest as they require a simple feeding, they have high directivity and efficiency, and they are very good candidates for beam-scanning applications due to their dispersive properties. It has been shown that static one-dimensional LWAs can achieve a steering of the main radiation beam with frequency, if the antenna's source is placed towards the one end of the structure [10].

2.2 PERIODIC ANALYSIS AND ELECTROMAGNETIC SOLVERS

Periodic structures can be analysed employing Floquet's theorem which is an extension of Fourier series theorem [1]. According to this theorem, the problem of an infinite periodic structure can be reduced to the analysis of a single unit cell. The scattered fields from the periodic array and the induced currents from plane wave excitation can be expressed as a Fourier series where the periodicity is equal to that of the unit cell.

Using the appropriate boundary conditions, electromagnetic fields can be calculated through various techniques. One of these techniques is Method of Moments (MoM) which is a Frequency domain – Integral Equation method, based on solving the integral equation of the unknown currents reducing them to a linear system of simultaneous equations [11]. Other techniques include Time domain-Differential equations such as Finite Difference Time Domain (FDTD) [12, 13], Finite Element Method (FEM) [14] or Transmission Line Matrix (TLM) [15]. The aforementioned techniques are employed by different commercial simulation software packages and have advantages and disadvantages depending on the geometry of the structure under investigation. For example, MoM is very accurate for the analysis of simple structures but not suitable for structures with arbitrary geometries since it cannot take into account fine details. On the other hand, both FDTD and FEM are suitable for small and moderate size structures with arbitrary shapes.

2.2.1 Commercial 3D Electromagnetic Solvers

Some of the commercial simulation softwares that can be employed to perform periodic analysis are ANSYS HFSS, Analyst^{TM} and FEKO. In this PhD thesis CST Microwave Studio^{TM} simulation software has been used.

CST Microwave Studio^{TM} is a 3–D simulation software which was originally based on Finite Difference Time Domain (FDTD). FDTD is a numerical method of solving the electromagnetic fields for periodic structures and is based on Time domain-Differential equations [12, 13]. CST includes various electromagnetic solvers, each suitable for different type of structures. In this thesis three of them were utilized, the finite integral Time-Domain (TD) solver, the finite-element Frequency-Domain (FD) solver and the Eigenmode solver. The TD solver employs a numerical technique similar to FDTD with the main difference being that it uses the integral form of Maxwell equations, as opposed to the differential form employed by FDTD. It is ideal for analysing structures for a broadband frequency range but it is not suitable for highly resonant structures. It can be employed for the analysis of the unit cell of a 2D periodic structure applying electric boundaries along the one repetition axis and magnetic boundaries along the other axis. However, this solver can produce results just for normally incident plane wave. If an oblique angle of incidence needs to be considered, then FD solver has to be employed. This solver is appropriate for the analysis of highly resonant structures. Moreover, it gives the option of periodic boundary conditions for the unit cell of periodic structures. These boundary conditions can be applied to arbitrarily shaped unit cells and infinite size structures are assumed, introducing the appropriate phase shift between consecutive periodic elements. Finally, the Eigenmode solver is suitable for the simulation of closed resonant loss free structures. It is a FD based solver used to calculate the frequencies and the corresponding electromagnetic field patterns (eigenmodes), where no excitation is applied. In this thesis it is employed to obtain dispersion diagrams of the periodic structures under investigation. It also includes the feature of periodic boundary conditions, which are utilized in the simulation of the unit cell for the generation of the dispersion diagram, since the solver calculates the eigenmode frequencies of the supported modes [16].

2.3 TUNING COMPONENTS

Tuning of periodic structures can be achieved with various techniques as described in section 1.1.2 and it consists in using either a tuning component or a tunable substrate. The work in this thesis has focused on the use of two types of components, varactor diodes for low frequency applications (below 10GHz) and piezoelectric actuators for higher frequency applications (from 10GHz to ~60GHz).

2.3.1 Varactor Diodes

Varactor diodes, also known as varicap diodes or variable capacitance diodes are diodes that exhibit a capacitance across their terminals that depends on the voltage applied to them. The symbol that is typically used to represent the varactor diode is the one shown in (Fig. 2.3.1a), alternatively the symbol shown in Fig. 2.3.1(b), corresponding to a capacitor with a variable value can also be utilized. As diodes, they are semiconductor devices that consist of a PN junction optimised to perform as a variable capacitor under reverse bias. Three regions are created in the diode, the P region illustrated in blue in Fig. 2.3.2, the N region illustrated in red and the white region that corresponds to the depletion zone. When voltage is applied the regions P and N can conduct current but the depletion zone acts as an insulator as no current carriers are available. This is how the capacitor is created, since two conducting areas are formed around a non conducting dielectric. As the voltage increases the depletion zone occupies more space, so the distance between the two effective metallic plates increases resulting in a decrease of the diode's capacitance (Fig. 2.3.2b).

Ideally the diode would only exhibit the variable capacitance C_v and no losses but in a practical case, the equivalent circuit of a varactor is as depicted in Fig. 2.3.3. The resistance R_s can arise from the semiconductor, from the lead and package elements of the component and

a small part could be caused from the dielectric substrate. The inductance L_s is attributed also to the packaging and finally there is a parasitic capacitance C_p [17].

(a)   (b)
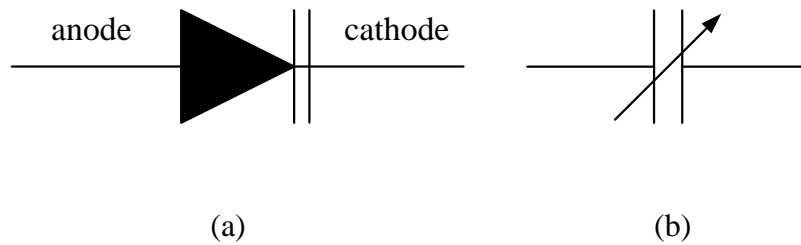
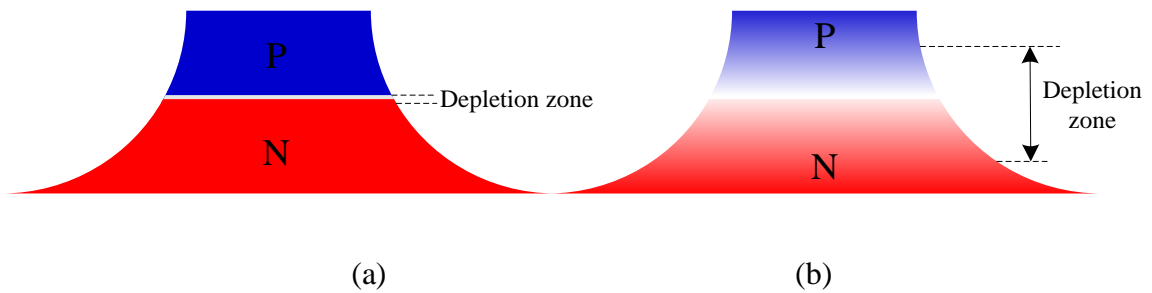Fig. 2.3.1.   Alternative symbols for varactor diode representation.

(a)   (b)

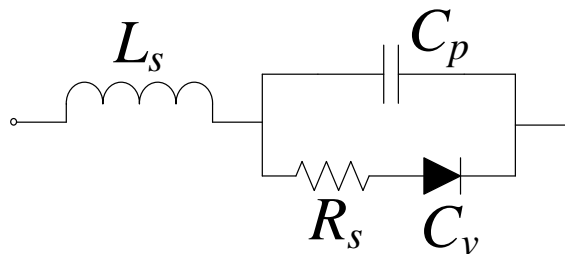Fig. 2.3.2.   Illustration of PN junction in a varactor under reverse bias: (a) unbiased state corresponding to maximum capacitance, (b) biased state.

Fig. 2.3.3.   Equivalent circuit of a varactor diode representation.

As mentioned in section 1.1.2, varactor diodes are suitable for a variety of applications where tuning is desired. However they are not appropriate for high frequency applications as they exhibit high losses and non-linearities.

2.3.2 Piezoelectric Actuators

The piezoelectric effect is a physical phenomenon that consists in the generation of an electric potential when pressure is applied to specific type of materials such as quartz crystals, called piezoelectric materials. However, the inverse effect is also observed in certain materials, where expansion of the material is obtained when voltage is applied to it, converting electrical energy to mechanical energy. This inverse piezoelectric effect is the principle of operation of the piezoelectric actuators in order to produce displacement. There are different types of piezo-actuators classified depending on their displacement mode in Longitudinal Stack Actuators, Shear Actuators, Tube Actuators, Contracting Actuators and Bending Actuators. In this work, two types of piezo-actuators have been used; the bending or bender actuators and a type of longitudinal stack actuators available from Physik Instrumente (PI) [18].

2.3.2.1 *Bender Actuators*

Bending or bender actuators are built from two layers of ceramic plates placed on top of each other (Fig. 2.3.4a). Each ceramic layer has the property of expanding or contracting when exposed to positive or negative electrical potential respectively due to the inverse piezoelectric phenomenon. Different voltage is applied to the upper and lower layer through the three electrodes (+V, 0, −V) provoking an expansion to the upper layer and a contraction to the lower one. This phenomenon creates a bending of the actuator, similar to the principle of thermostatic bi-metals, that translates the small change in the length of the ceramic plates

into a large vertical displacement (Fig. 2.3.4b). The total displacement of a piezoelectric bender actuator depends on its total length and can be described from (2.3-1) where ΔL_{bend} the bending displacement, n the number of ceramic layers, d a transversal piezoelectric deformation coefficient, l_f the actuator's free length, h_p the height of each layer and V the operating voltage (Fig. 2.3.4). They have a quick time response of less than 10msec and can achieve displacements up to several millimetres with a blocking force of up to a few newtons and a maximum operating voltage of 60V [18].

$$\Delta L_{bend} = \frac{3}{8} nd \frac{l_f^{2}}{h_P^{2}} V \qquad (2.3\text{-}1)$$

(a)

(b)
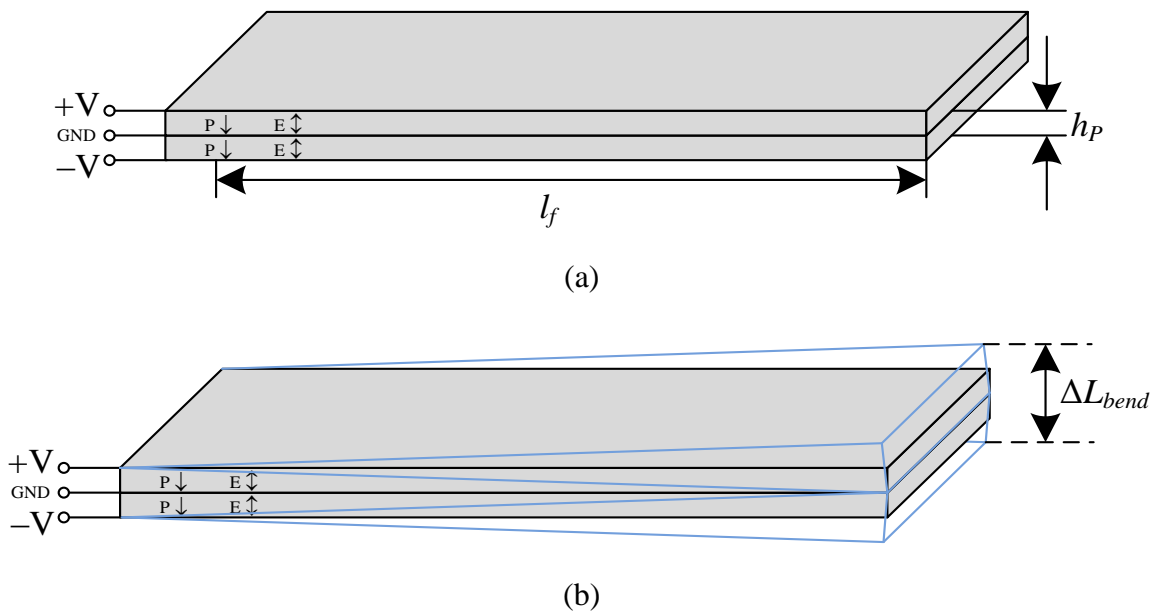
Fig. 2.3.4.   Schematic of piezoelectric bender actuator at (a) unbiased stated and (b) biased state.

2.3.2.2 *Stack Multilayer Piezo-actuators*

The next type of actuators described here, are a sub-category of longitudinal stack actuators. They are built from Lead (Pb) Zirconate (Zr) Titanate (Ti) (PZT) ceramic disks placed on top of each other forming stacks, also known as PZT stacks. A schematic diagram can be seen in Fig. 2.3.5(a). Due to the inverse piezoelectric phenomenon, each of the disks has the property of expanding vertically when exposed to an electric potential. In the stack, the disks are separated by thin metallic electrodes where the voltage is applied. Consequently, the total expansion ΔL of the actuator is the sum of the expansion of each disk. The maximum operating voltage is proportional to the thickness of the disks and the total displacement a piezo-stack actuator can produce is proportional to its total length and more specifically equal to 10% of its length. An estimation of the displacement can be made from (2.3-2) where d_{33} is a strain coefficient that describes the forces applied to the actuator and the properties of the piezoelectric material used, n is the number of ceramic layers and V is the applied voltage [18]. In order to achieve maximum displacement a mechanical preloading for the actuators is desired. This can be for example a spring which is supported on the surface to be displaced, on the side opposite the actuator and applies a small force opposing the expansion of the actuator. Therefore without preloading, a slightly smaller displacement is expected. A photograph of a stack multilayer piezo-actuator is shown in Fig. 2.3.5(b).

$$\Delta L \approx d_{33} \cdot n \cdot V \tag{2.3-2}$$
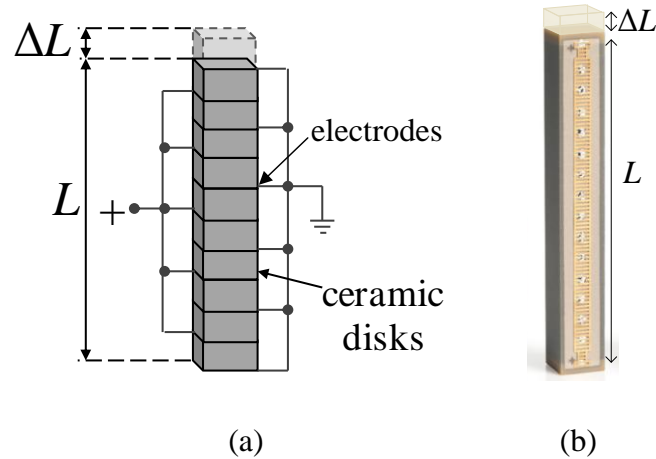
Fig. 2.3.5.   (a) Schematic diagram of piezoelectric stack multilayer actuator and (b) photograph of a commercial actuator.

The main advantages of this type of piezoelectric actuators are their high accuracy and reliability for nano-positioning applications, their low-cost and their very fast response in the order of microseconds, which is important for applications such as communication and radar systems. Moreover, they exhibit sub-nanometre resolution, high energy conversion efficiency, low voltage operation, large force and reduced Electromagnetic Interference (EMI). The maximum operating voltage in this type of actuators is 120V, while the maximum displacement that can be obtained is 38μm which is significantly less than the one obtained from bender actuators. This makes them suitable for higher frequency applications where a small displacement will have a significant effect [18].

REFERENCES

[1] M. G. Floquet, "Sur les équations différentielles linéaires à coefficients périodiques", *Annales scientifiques de l'École Normale Supérieure,* pp. 47-88, 1883.

[2] L. Brillouin, *Wave Propagation in Periodic Structures; Electric Filters and Crystal Lattices*, 2nd ed. New York: Dover, 1953.

[3] A. Harvey, "Periodic and guiding structures at microwave frequencies," *IRE Trans. Microwave Theory Tech.*, vol. 8, pp. 30–61, June 1959.

[4] M. Sigalas, C. Chan, K.-M. Ho, and C. Soukoulis, "Metallic photonic band-gap materials," *Phys. Rev. B, Condens. Matter*, vol. 52, pp. 11744–11751, 1995.

[5] R. Gonzalo, P. de Maagt, and M. Sorolla, "Enhanced patch antenna performance by suppressing surface waves using photonic bandgap substrates," *IEEE Trans. Microwave Theory Tech.*, vol. 47, pp. 2131–2138, Nov. 1999.

[6] J. C. Vardaxoglou, *Frequency selective Surfaces: Analysis and Design.*, vol. 10, Taunton: Research Studies, 1997.

[7] A. C. Lima and E. A. Parker, "Fabry–Perot approach to the design of double layer FSS," *Proc. Inst. Elect. Eng. Microw. Antennas Propag.*, vol. 143, no. 2, pp. 157–162.

[8] G. Goussetis, A. Feresidis and J. Vardaxoglou, "Tailoring the AMC and EBG characteristics of periodic metallic arrays printed on grounded dielectric substrate," *IEEE Trans. Antennas Propagat.*, vol. 54, no. 1, pp. 82-89, Jan. 2006.

[9] A. P. Feresidis, G. Goussetis, S. Wang, and J. C. Vardaxoglou, "Artificial magnetic conductor surfaces and their application to low profile high-gain planar antennas," *IEEE Trans. Antennas Propag.*, vol. 53, no. 1, pp. 209–215, Jan. 2005.

[10]   A. A. Oliner, *Leaky-Wave antennas*, in Antenna Engineering Handbook, 3rd ed, R. C. Hansen, Ed. New York: McGraw-Hill, 1993, ch.10.

[11]   R. F. Harrington, "*Field Computation by Moment Method*", New York, NY: Macmillan, 1968.

[12]   K. S. Yee, "Numerical Solutions of Initial Boundary Value Problems Involving Maxwell's Equations in Isotropic Media", *IEEE Trans. Antennas Propag.*, vol. 14, no. 5, pp. 302-307, May 1966.

[13]   A. Monorchio, and R. Mittra, "Time-Domain (FE/FDTD) Technique for Solving Complex Electromagnetic Problems", *IEEE Microw. and guided waves Lett.*, vol 8, no. 2, pp. 93-95, Feb. 1998.

[14]   M.N.O. Sadiku, "A Simple Introduction to Finite Element Analysis of Electromagnetic Problems", *IEEE Trans. Educ.,* vol. 32, no. 2, May 1989, pp. 85–93.

[15]   C. Christopoulos, "*The Transmission-Line Modeling Method in Electromagnetics*", Morgan & Claypool publishers, 2006.

[16]   www.cst.com

[17]   K. E. Mortenson, *Variable capacitance diodes: the operation and characterization of varactor, charge storage and PIN diodes for RF and microwave applications*, Dedham, Mass.: Artech House, 1974.

[18]   www.physikinstrumente.co.uk

CHAPTER 3.

TUNABLE EBG STRUCTURES USING VARACTOR DIODES AND APPLICATIONS

EBG structures have been proposed in the past for isolation enhancement between closely spaced antennas, such as the elements of an antenna array [1] or the antennas of multiple input multiple output (MIMO) communication systems [2, 3]. Various configurations have been proposed such as multiple slots etched in the ground plane of the antennas [4, 5], and metallic patch EBG structures which suppress the surface waves and currents in common ground planes and therefore isolate closely spaced antennas [6-8]. Although EBG structures require a large number of elements (ideally infinite) in order to exhibit their full properties, there are various reports of isolation improvement using EGB structures with only a small number of elements along the virtual line that connects the two antennas [6, 8]. Even with this small number of elements, the obtained results demonstrate that surface wave suppression can be achieved within the area of interest.

Recently, miniaturized EBG structures have been proposed for broadband mutual coupling reduction between UWB monopoles, employing double-layer structures and exploiting the coupling between the layers to achieve the miniaturization [9]. However, for multi-band or tunable antennas, low mutual coupling in all the frequency bands of interest is desired. Tunable or reconfigurable antennas are required in many applications where the antenna's performance has to adapt to a varying environment, for example in multi-band communication systems or cognitive radios [10-12].

In this Chapter, novel tunable two–layer varactor-loaded EBG structures are presented, with a wide tuning range and significantly simplified biasing network. The structures consist

of apertures (slots or slits) etched off a metallic ground, and a varactor-loaded patch printed on a thin dielectric substrate, placed on top of each aperture. The proposed EBGs are initially excited by a microstrip line and exhibit a stop-band in the S_{21} response which is then tuned by changing the voltage applied to the varactor diodes. The proposed structure is then employed for enhancing the isolation between printed antennas. Initially two ultra wideband (UWB) monopoles are used in order to demonstrate the tuning range of the proposed structure. Tunable monopoles are also presented resulting in a tunable two-element antenna with high isolation across the tuning range. Simulations were performed in a full-wave software package (CST Microwave Studio^{TM}) to predict the performance of the proposed design. Prototypes of the proposed structures have been fabricated and tested and the measured results are presented yielding good agreement with the simulated results.

3.1 TUNABLE EBG STRUCTURES

The proposed tunable EBG structures consist of slots or slits etched off a metallic ground. The slots are λ/2 long and are located in the centre of the ground plane, while the term slit refers to λ/4 long structures at the edge of the ground plane with an open termination (see Fig. 3.1.7). A varactor-loaded split patch is placed on top of each slot/slit as depicted in Fig. 3.1.1(a), printed on a thin dielectric substrate separating the patches from the slots/slits and the ground. A better visualization of the different layers of the structure can be obtained from the cross-section of the structure illustrated in Fig. 3.1.1(b). Due to the close distance of the patches and the slots/slits, there is a strong coupling that alters the resonant frequency of each individual slot-patch resonator when the capacitance value of the varactor is changed. One of the advantages of the proposed multi-layer structure is the electrical isolation between the diodes and the ground plane which greatly simplifies the biasing network.

As a working example, the ground plane with the slots/slits is printed on a 1.52mm thick

Taconic RF-35 dielectric substrate (ε_r=3.5, $tan\delta$=0.0018) with overall dimensions 50mm×30mm. On the other side of the substrate, a 50Ω microstrip line excites the slots to allow an investigation of the band-gap regions of the proposed EBG structure and its tunability.

(a)

(b)
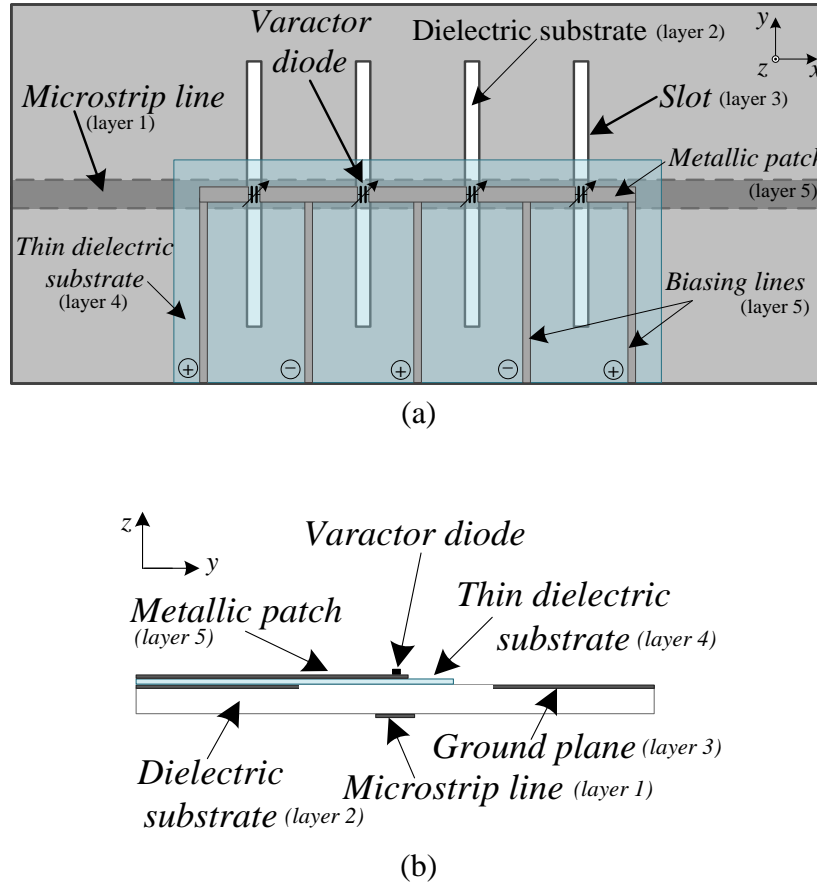
Fig. 3.1.1   Schematic diagram of proposed structure with microstrip line excitation: (a) Proposed tunable EBG structure with four slots, (b) Cross section.

3.1.1 Dispersion Characterization of Slots in a Ground Plane

In this section, the proposed EBGs are studied using a rigorous full-wave dispersion analysis. Initially, we assume a 1D periodic array along the *x*-axis of slots etched off the ground plane and conducting patches placed on top of them, printed on a thin dielectric

substrate of thickness h=0.055mm and dielectric constant ε_r=3, separating the patches from the slots and the ground. The microstrip line is also included in the design. The unit cell of the structure is depicted in Fig. 3.1.2(a). The slot has a length of 15.5mm and a width of 0.5mm, and is situated exactly at the middle of the unit cell whose periodicity is D_x=8mm, while the width of the patch is 1mm. The dimensions have been chosen to obtain a band-gap at frequencies around 3GHz. Due to the close distance of the patch and the slot, there is a strong coupling that alters the resonant frequency of the structure if the dimensions of the patch are changed and thus the frequency of the band-gap is altered. In order to evaluate how the patch length affects the resonant frequency, simulations have been carried out changing this parameter. The dispersion diagram for propagation at this direction (ΓX) has been extracted using the simulation software (CST) Eigenmode solver by applying periodic boundaries and imposing the appropriate phase shift between the boundaries, and is illustrated in Fig. 3.1.3(a). This is performed varying the patch length from 4mm to 8mm. It can be observed that as the patch length decreases the band-gap is shifted towards higher frequencies (from 2.75GHz to 3.44GHz). The same behaviour is observed in Fig. 3.1.3(b) which presents the S_{21} response of a structure formed by 4 unit cells. Good agreement of the two approaches (dispersion diagram and S_{21}) is obtained for the band-gap region of the structure. From this study, it can be concluded that as the patch length p_x decreases, the coupling between the patch and the slot also decreases, leading to the frequency shift of the band-gap. Based on this study, a varactor diode is employed on the patch which effectively changes the patch electric length, in order to be able to dynamically control the frequency as demonstrated in the next sections (section 3.1.2 – 3.1.4).

(a)   (b)
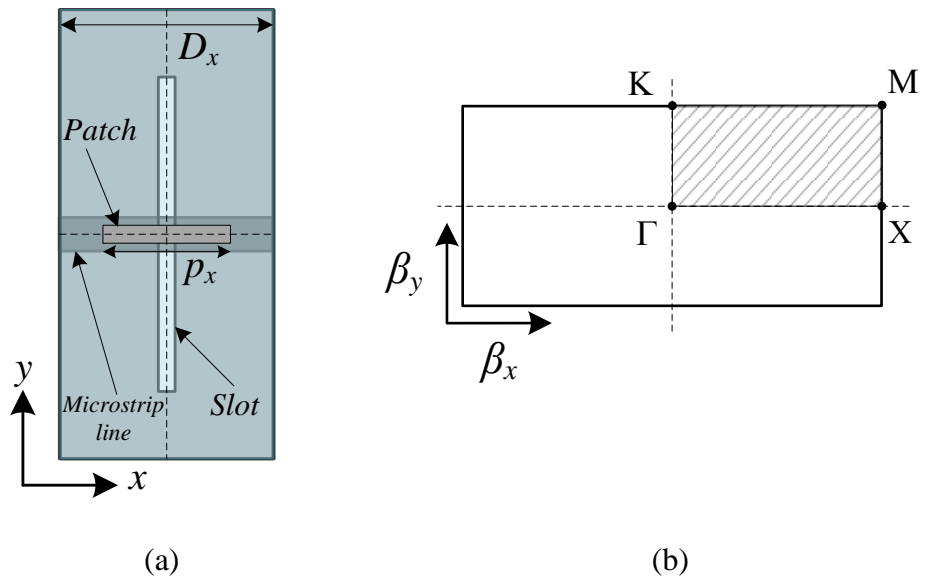
Fig. 3.1.2   Unit cell of EBG structure, (b) Representation of the reciprocal lattice and the

irreducible Brillouin zone.
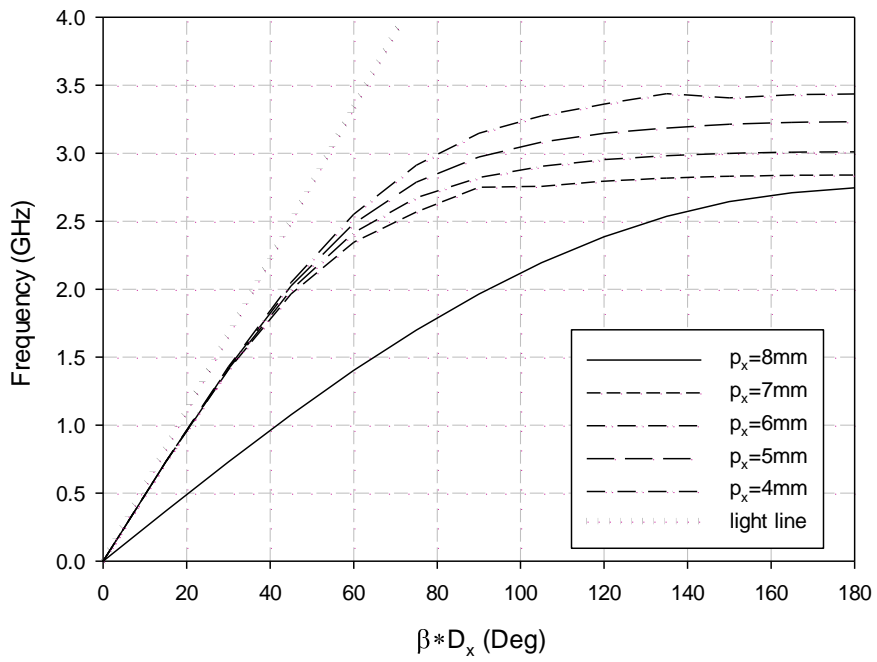
(a)
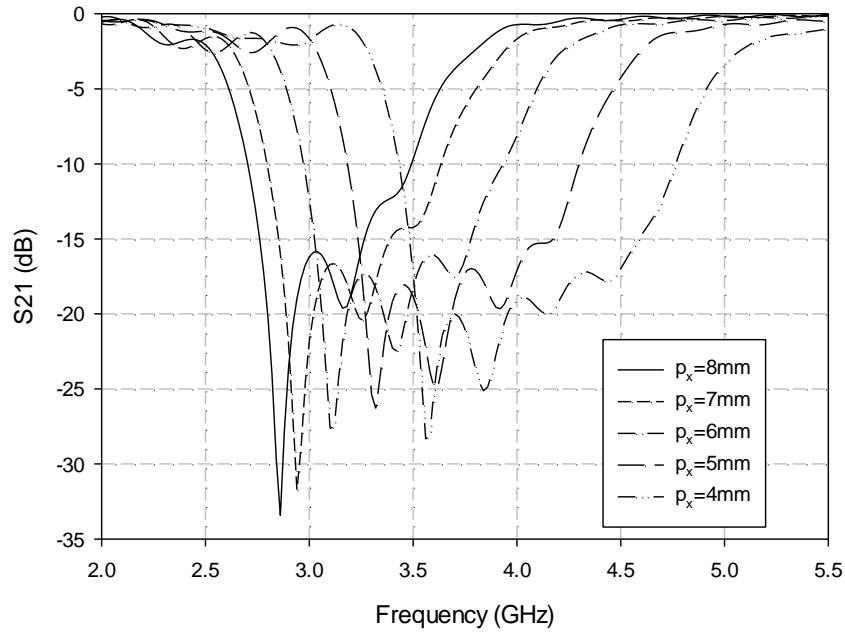
(b)

Fig. 3.1.3   Dispersion diagram along the ΓX direction and (b) S_{21} response for different patch lengths.

3.1.2 Design of Single Tunable Slot-Patch Structure

A single tunable slot-patch structure is investigated in this section, as the resonator which constitutes the building block of the proposed EBGs. The structure is shown in Fig. 3.1.4, where the slot has the dimensions given in the previous section, and is placed exactly at the middle of the metallic ground. The patch has length p_x=8mm and width 2mm. Different thin substrates have been investigated but for the particular design the patch is printed on a 130μm thick RO3010 substrate (ε_r=10.2, $tan\delta$=0.0023) shown in light blue in the figure. A varactor diode is inserted in the middle of the patch where a small gap is etched producing a split patch. The dimensions of the slot and the patch have been chosen such that the resonance would occur in the frequency range of interest (2GHz-5GHz). More specifically, the slot itself produces a minimum in the S_{21} response around 8GHz since its length is about λ/2 at this

48

frequency. The resonant frequency is then reduced due to the strong capacitive coupling between the slot and the varactor loaded patch. Apart from the actual patch which is perpendicular to the slot; two metallic lines along the y direction are also included in the design serving as biasing lines for the varactor (see Fig. 3.1.1a and Fig. 3.1.4). These lines are isolated in practice from the patch through RF choke inductors which are not shown in the figures. *The electrical isolation of the diode from the ground plane significantly simplifies the biasing by eliminating the need for additional slots and the use of DC blocking capacitors on the ground plane.*

The complete structure is simulated in CST, modelling the varactor as an ideal lumped capacitor with parametrically changed capacitance. The extracted S_{21} response is shown in Fig. 3.1.5(b) while the corresponding S_{11} response is depicted in Fig. 3.1.5(a). It can be observed that a sharp minimum is produced in the S_{21}, which is tuned towards lower frequencies as the capacitance increases. This is expected since the total equivalent capacitance of the resonator increases, causing a decrease in the resonance frequency. For C=0.5pF to C=1.4pF, the resonant frequency is tuned from 3.9GHz to 2.75GHz resulting in a tuning range of 34.6%. This single slot-patch structure has proven the validity of the concept and can be considered the unit cell of the proposed tunable EBG structure.
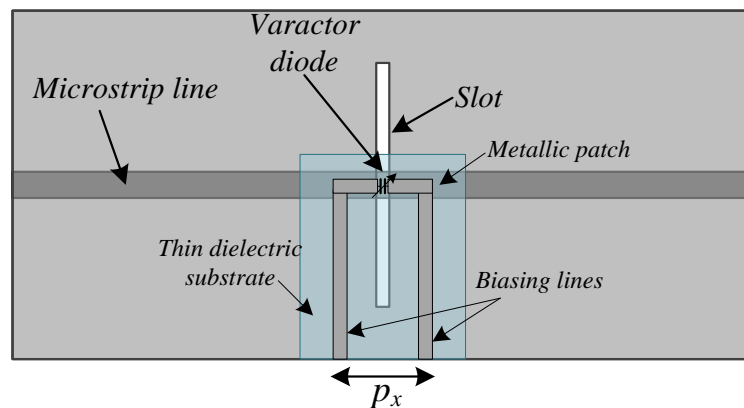
Fig. 3.1.4   Schematic diagram of proposed single slot-patch structure.
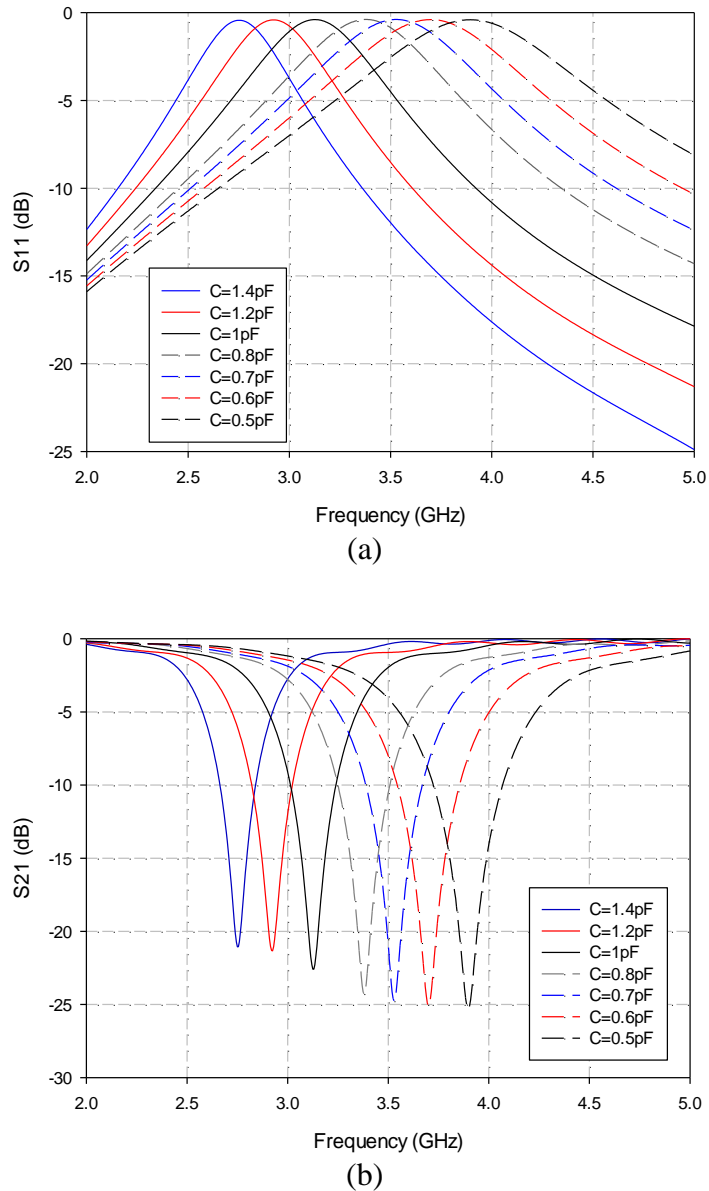
Fig. 3.1.5   Simulated (a) S_{11} and (b) S_{21} response of a single slot-patch structure for different capacitance values.

3.1.3 Design of Multiple Tunable Slot-Patch EBG

Subsequently, four slots were etched off the ground plane with the dimensions described in the previous sections (Fig. 3.1.1a). The periodicity of the structure is 8mm. This is equal to the length of each patch, which means that the patches are connected, reducing the number of

the required biasing lines. Fig. 3.1.1(a) shows that the first varactor diode is placed with the cathode on the left side, the next diode reversed with the cathode on the right side and so on for the other two diodes, allowing all the diodes to be correctly biased using only 5 biasing lines instead of 8.

(a)

(b)
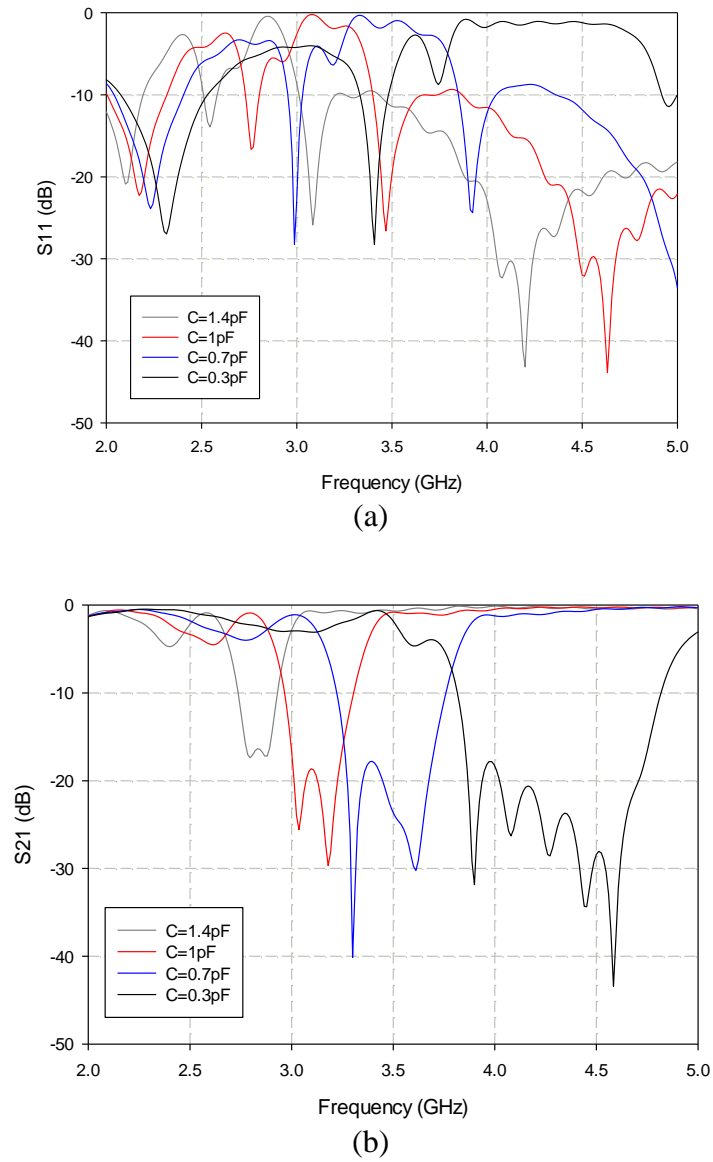
Fig. 3.1.6   Simulated (a) S_{11} and (b) S_{21} response of four slot-patch structures for different capacitance values.

Again, the varactors are modelled as capacitors with different capacitance values and the S_{21} response has been obtained, presented in Fig. 3.1.6(b). The corresponding S_{11} is shown in Fig. 3.1.6(a). Although the tuning is continuous, only four states are illustrated in the figure for clarity. It is evident that in the case of multiple slot-patch structures, a broader band-gap is produced. As the capacitance of the varactors increases, the band-gap shifts to lower frequencies while its bandwidth decreases. Nevertheless, a significant tuning range is achieved for capacitances from C=0.3pF to C=1.4pF, tuning the beginning of the band-gap from 3.85GHz to 2.77GHz and the end from 4.78GHz to 2.9GHz respectively.

3.1.4 Design of Slit-patch Structures

Finally, the concept is extended to slits instead of slots. The slits are etched in the middle of the long side of the ground plane (*x* axis) and have length *l*=6mm and width *w*=1mm. In this case the initial length of the slit without the patch is $\lambda/4$ at its resonant frequency, which is then reduced due to the coupling with the patches. The microstrip line is also moved accordingly and the patches are positioned in the middle of the slits as shown in Fig. 3.1.7. In this case a different substrate is employed for printing the patches. It consists in a 55μm thick polyester film with dielectric constant ε_r=3.

A configuration with three slit-patch structures is investigated. The effect is similar to the case of the slot-patch structures, with the difference of a larger tuning range achieved with a smaller capacitance range (0.9pF compared to 1.1pF). This is expected since the substrate separating the varactor-loaded conducting patches from the slits is now significantly thinner, making the coupling between the two layers stronger. Other than that, similar tuning behaviour is observed, with the slit-patch structures giving a broadband S_{21} minimum, as can be seen in Fig. 3.1.8.
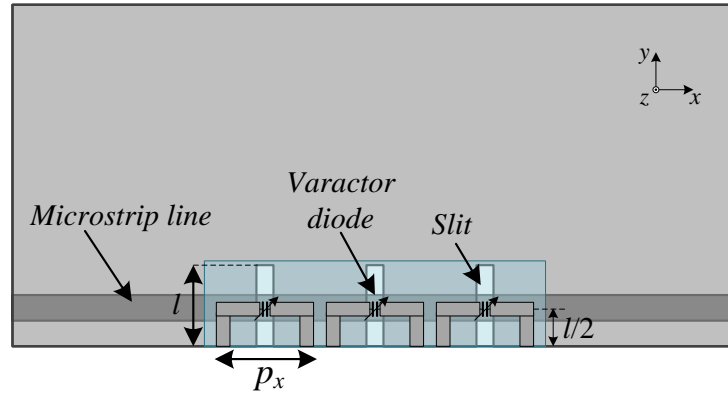
Fig. 3.1.7   Schematic diagram of three slit-patch tunable structures excited by microstrip line.
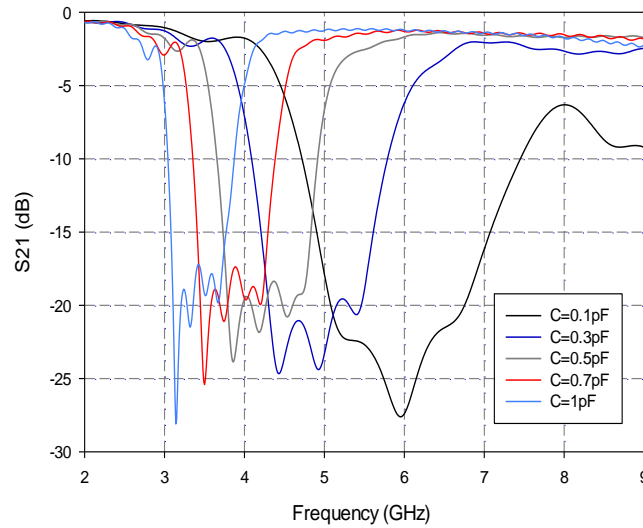
Fig. 3.1.8   Simulated S21 response of three slit-patch structures for different capacitance values.

3.1.5 Equivalent Circuit Approach

An equivalent circuit approach has been developed to analyse the proposed EBG structure in order to provide valuable insight and initial design guidelines. The slots or slits in a metallic plane can be modelled as a parallel *LC* circuit producing a resonance in the S_{21} response. Depending on the length of the aperture, the resonance frequency can be calculated

and hence the product of *L* and *C* can be evaluated. The values of *L* and *C* can be estimated by matching the equivalent circuit response with the one obtained from full-wave simulations. Adding the varactor-loaded patch, introduces an extra capacitance as explained earlier, due to the close coupling between the aperture and the patch which decreases the resonance frequency. This is modelled as capacitance C_1 parallel to the *LC*. The resulting equivalent circuit for the configuration with the one slot is shown in Fig. 3.1.9(a), where C_1 includes the capacitance introduced by the patch itself and the one introduced by the varactor diode. A comparison between the responses obtained from the equivalent circuit and the full-wave simulations is shown in Fig. 3.1.10(a) for four values of the varactor's capacitance showing a good agreement.

The four-slot structure is modelled connecting four resonators in series (Fig. 3.1.9b). The length of the transmission line between the resonators l' is adjusted to match the distance between the slots. The obtained results in this case are depicted in Fig. 3.1.10(b). It is evident that for the four slots the agreement between full-wave and equivalent circuit simulations is not as good as for the case of one slot-patch. This is to be expected since the equivalent circuit approach does not take into account higher order mode interactions between the elements. However, the use of the equivalent circuit gives an insight into the behaviour of the proposed EBG structures. Moreover, it provides a fast and useful tool for an initial estimation of the structure's response.

(a)

(b)
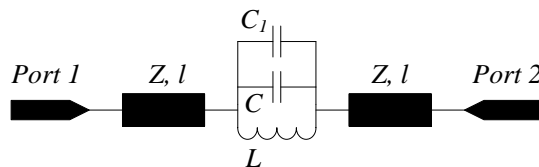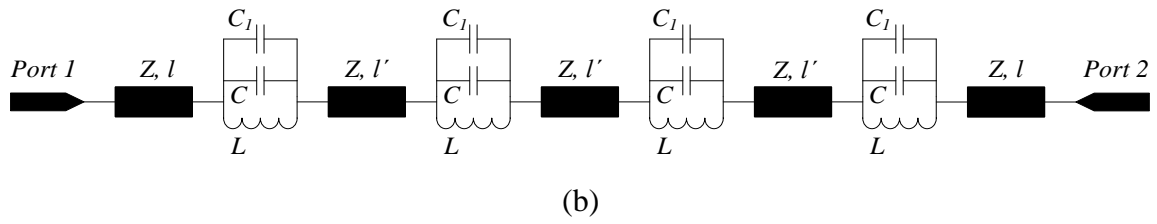
Fig. 3.1.9　Equivalent circuit for (a) a single slot-patch structure and (b) four slot-patch structures excited by microstrip line.
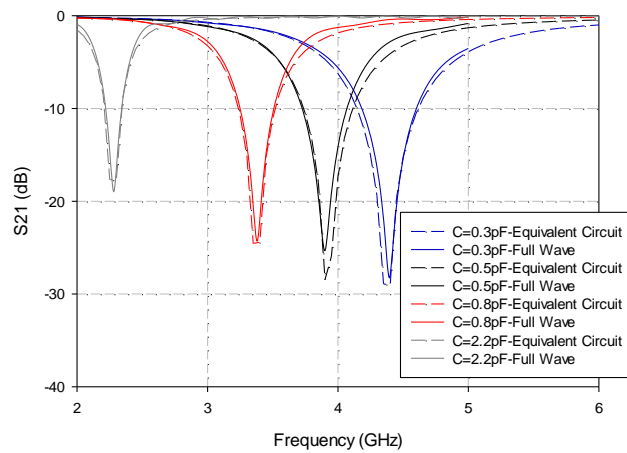
(a)
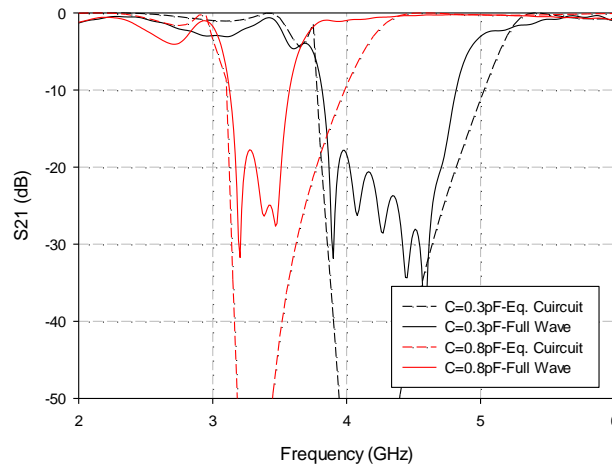
(b)

Fig. 3.1.10　S_{21} response comparison calculated from the equivalent circuit and full-wave analysis for (a) the single slot-patch and (b) the four slot-patch structures for different capacitance values.

3.1.6 Measurements of Fabricated Prototypes

In this Section, measurements of the fabricated prototypes of the proposed tunable EBG structures are presented. Various prototypes have been fabricated and the experimental results validate the concept, giving the expected behavior.

For the case of the single slot-patch, the fabricated prototype is shown in Fig. 3.1.11(a). The patch has been printed on a 130μm thick Rogers RO3010 dielectric substrate, also used in the simulations of the previous sections. The varactor diode used for this structure is the SMV1231 from Skyworks which according to its datasheet has a capacitance range from 0.466pF to 2.35pF for biasing voltages of 15V to 0V respectively. Moreover, two RF choke inductors (L=10nH) have been used.

The measured S_{21} results are presented in Fig. 3.1.11(c) with the corresponding S_{11} shown in Fig. 3.1.11(b). Compared with the simulation results, the measured S_{21} minimum is slightly higher and slightly shifted in frequency for all capacitance values. This can be attributed to a weaker coupling between the patch and the slot due to air gaps formed between the film and the ground during the soldering of the varactor on the thin substrate. The measured tuning range was 25.4%. Finally the losses and possible radiation of the structure have been calculated using the expression $1 - \left| S_{11} \right|^2 - \left| S_{21} \right|^2$ and the results for different voltages are plotted in Fig. 3.1.11(d). It can be observed that there is about 30% to 40% losses/radiation in the proposed structure. However, simulating the structure considering lossless materials only an 8% (0.3dB) of radiation is exhibited. Thus, the rest is losses due to the materials of the prototype, the varactor diode and the soldering of the components.
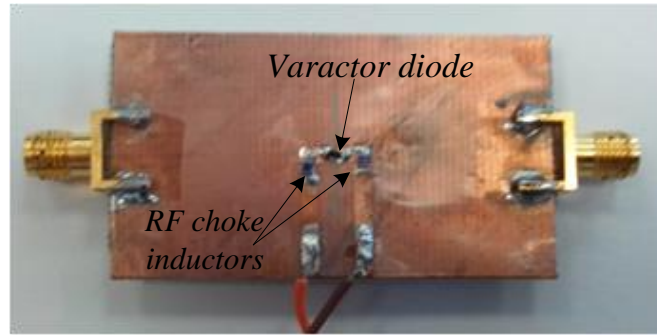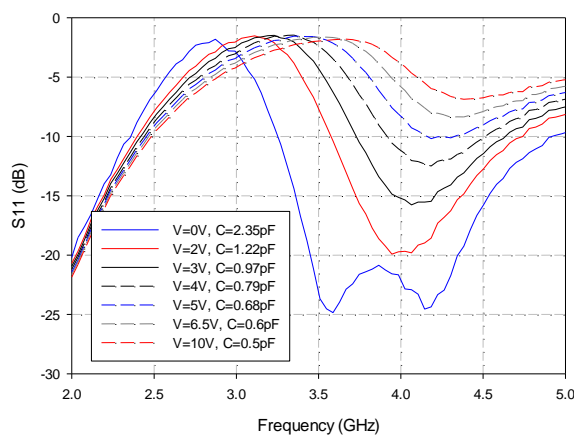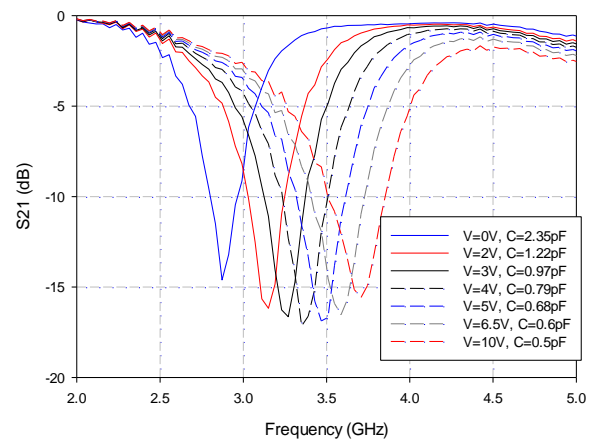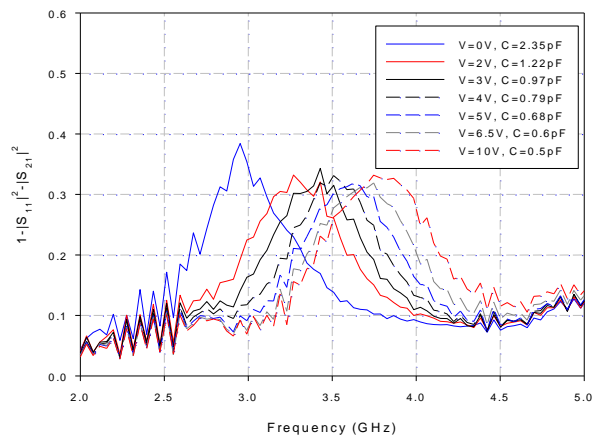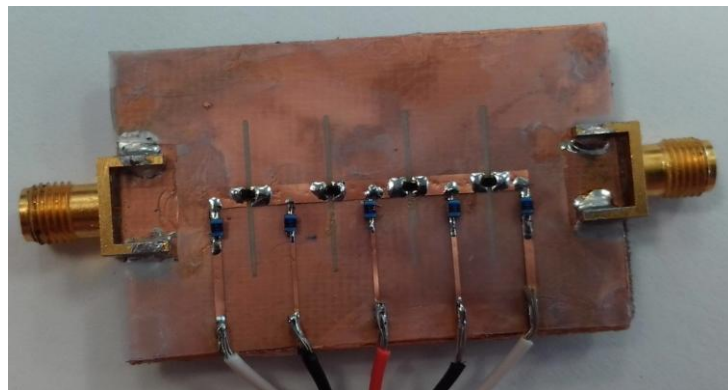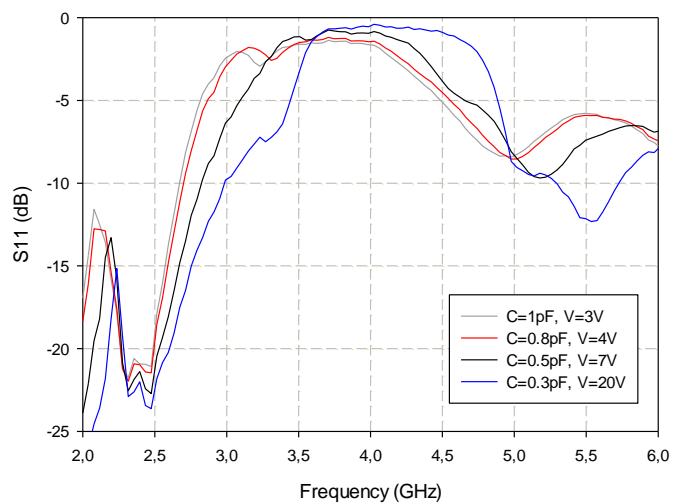
Fig. 3.1.11   (a) Photograph of a fabricated prototype, Measured (b) S_{11} and (c) S_{21} response of the single slot-patch structure for different voltages, and (d) Estimated radiation and losses from measured S-parameters.

Subsequently, the multiple slot-patch EBG structure has been fabricated and measured (Fig. 3.1.12). The varactor diodes used for this structure are the SMV2019 from Skyworks

which have a nominal range of 0.3pF to 2.22pF for biasing voltages of 20V to 0V respectively. The measured S_{11} is depicted in Fig. 3.1.12(b) showing that the structure losses caused from both the varactor diodes and material losses are from 0.7dB to 1.5dB. Fig. 3.1.12(c) shows the comparison between measured and simulated S_{21} for four different applied voltages. Good agreement has been obtained for the cases corresponding to C=0.3pF and C=0.5pF. However, as the capacitance of the varactor diodes increased, two distinct resonances appear. The resonance at the lower frequency end follows the expected behavior while the resonance at the higher frequency end appears to be fixed at 4GHz independently of the biasing voltage. This effect is apparent for both C=0.8pF and C=1pF and it is attributed to a fault in one of the varactor diodes. More specifically, the simulation results shown in the figure correspond to a reduction of one diode's capacitance to C´=0.32pF. The obtained agreement demonstrates that the maximum capacitance of one of the diodes is less than 0.4pF, resulting in the specific obtained resonance. In fact, this perturbation in the elements of the EBG structure actually gives an advantage since it increases the bandwidth of the stop-band. This effect will be exploited later on in section 3.2.1. Nonetheless, the achieved tuning range of the start of the stop-band for C=0.3pF to C=1pF is significant (Fig. 3.1.12d), namely 18.2% while the corresponding simulated tuning range is 24.8%.
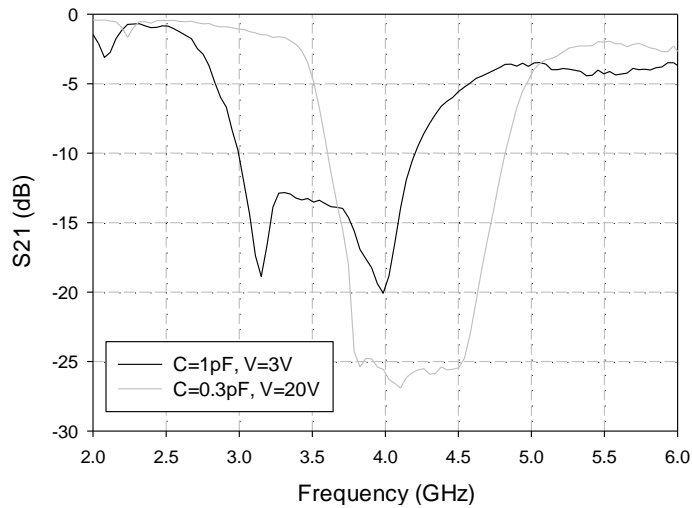

(a)

(b)
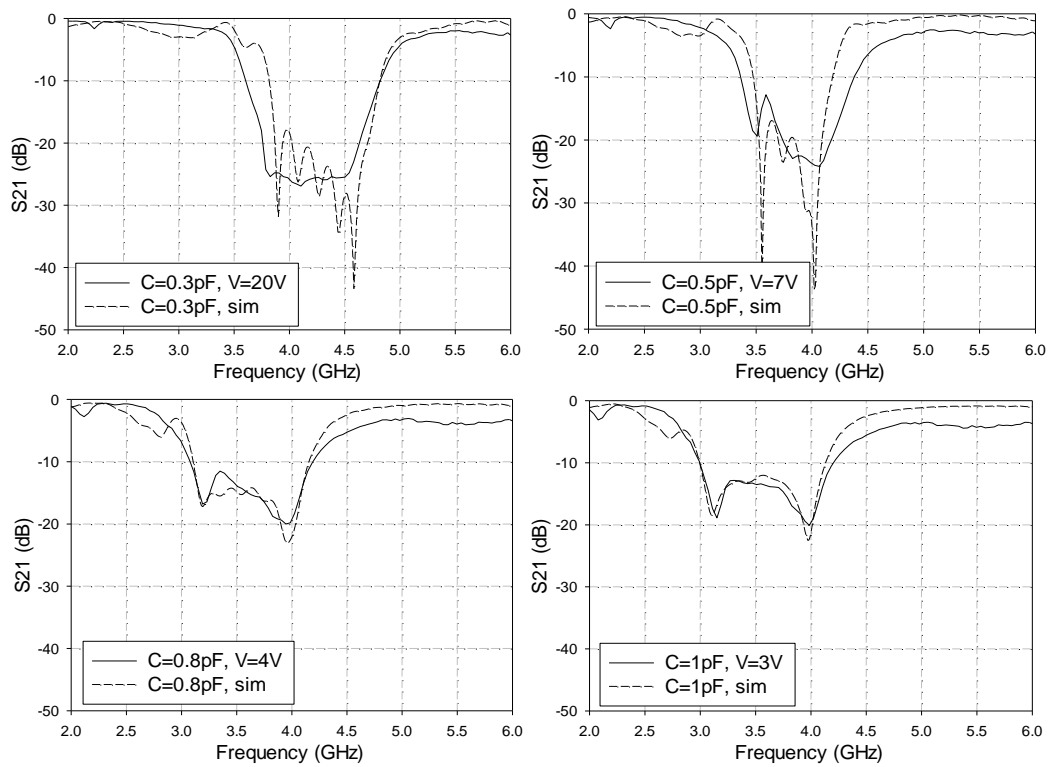
(c)

(d)

Fig. 3.1.12   (a) Photograph of a fabricated prototype, (b) Measured S_{11} response, (c) Comparison of measured and simulated S_{21} response of four slot-patch EBG structure for different voltages and (d) Achieved tuning range for V=3V to V=20V.

3.2 APPLICATION OF TUNABLE SLITS FOR ISOLATION IMPROVEMENT OF CLOSELY SPACED ANTENNAS

As mentioned in the beginning of this Chapter, one of the main applications of EBG structures is the isolation enhancement in multiple antenna systems. Thus, the application of the proposed tunable structures in such cases is investigated for both static and tunable antennas.

3.2.1 Isolation of Closely Spaced UWB Monopoles

An array of two closely spaced ultra-wideband (UWB) monopoles with a common ground plane has been designed, printed on a FR-4 dielectric substrate as shown in Fig. 3.2.1(a). The substrate is 60mm long and 50mm wide, with a thickness of 1.55mm and a dielectric constant ε_r=4.5. A 50Ω Coplanar Waveguide (CPW) microstrip line is employed for the feeding of the

60

antennas. The dimensions for the monopoles are chosen to achieve an operation from about 2.2GHz to 6.3GHz while the distance between them is less than λ/4 at the central operating frequency of the antennas. All the dimensions are shown Fig. 3.2.1(a).

In Fig. 3.2.1(b) the simulated S–parameters of the structure are presented. It can be observed that the coupling between the two monopoles is about −10dB at the lower end of the operating frequency band, and it slowly decreases with frequency, since the electrical separation between the antennas increases.

(a)   (b)
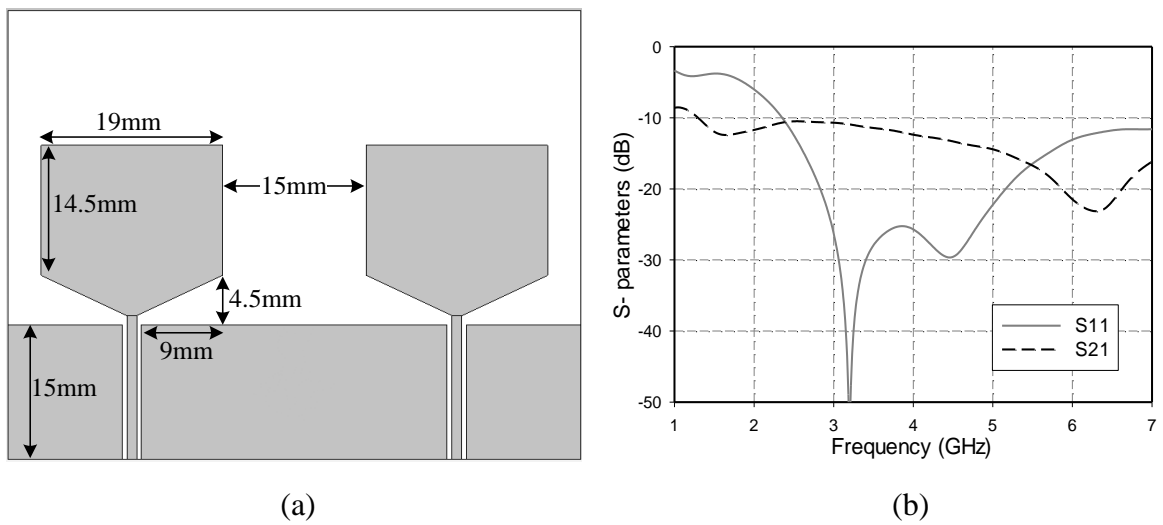
Fig. 3.2.1.   (a) Schematic diagram of the antenna array with common ground plane and (b) simulated S-parameters response for the structure.

3.3.1.1 *Two Printed UWB Monopoles with One Slit-Patch Structure*

To reduce the mutual coupling between the two monopoles, the proposed double layer slit-patch structure is employed. Most of the coupling in these closely spaced monopoles is caused by the strong currents in their common ground plane. Hence, employing the proposed EBG would disrupt these currents and result in an isolation improvement. Initially, a single slit was etched on the ground plane between the monopoles (Fig. 3.2.2a). The slit itself causes a reduction of the mutual coupling at its resonance frequency which for this length is 9GHz.

However, after placing the conductive patch in close proximity to the slit, the effective resonant length is reduced, shifting the S_{21} minimum in the frequency range of interest. The conducting patch is printed on the 55μm thick polyester dielectric sheet separating it from the slit and the ground, as shown in Fig. 3.2.2(b). The dimensions of the patch are the ones given in section 3.1.2 (length p_x=8mm and width 2mm) and are also shown in the same figure. The resonance of the element causes a transmission minimum in the S_{21} response which could be tuned in the frequency band of interest changing the length of the patch as demonstrated in section 3.1.1. Employing the proposed tunable structure, dynamic tuning of this transmission zero is produced. It should be pointed out again at this point that the electrical isolation of the diode from the ground plane of the antennas makes the biasing very straightforward eliminating the need for additional slots in the ground and the use of DC blocking capacitors.

(a)   (b)
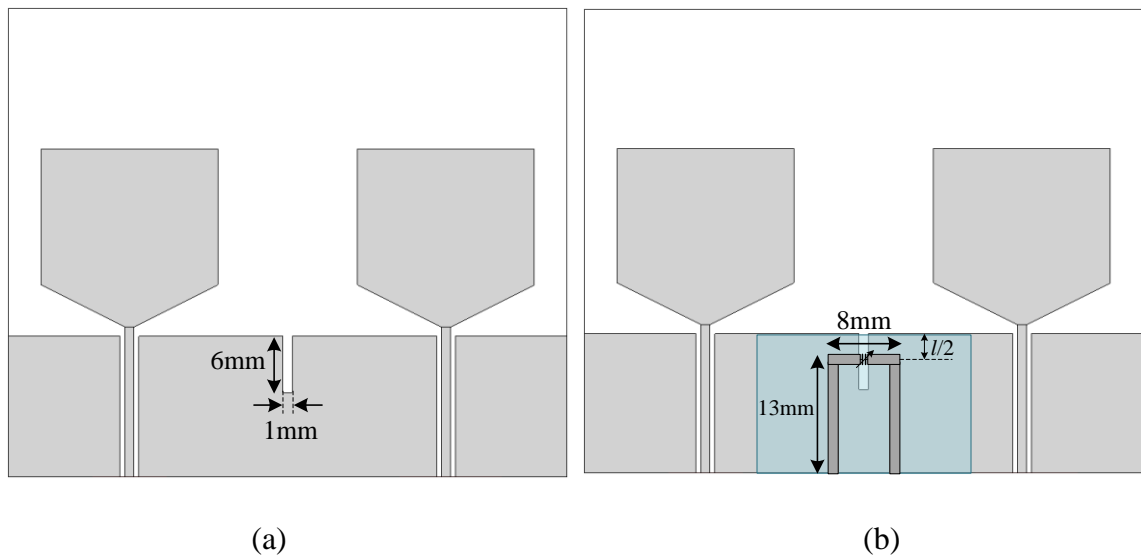
Fig. 3.2.2.   Schematic diagram of the antenna array with: (a) one slit etched in the middle of the ground, (b) one slit-patch structure.

Simulation results of the tuning of the S_{21} minimum for capacitance values between 0.3pF and 1.2pF are presented in Fig. 3.2.3(b) and the respective S_{11} response is shown in Fig. 3.2.3(a). More than 30% tuning of the transmission minimum is achieved, from 2.9GHz to

4GHz with an isolation of about 20dB. As the capacitance increases, the null shifts to lower frequencies. Further tuning could be achieved for higher values of capacitance but the tuning range is limited by the S_{11} response which is affected, assuming values over −10dB at the lower frequency band. The simulated total antenna efficiency is above 80% for capacitances up to 1pF and is better than the efficiency of the antenna array without the slit-patch as shown in Table I.
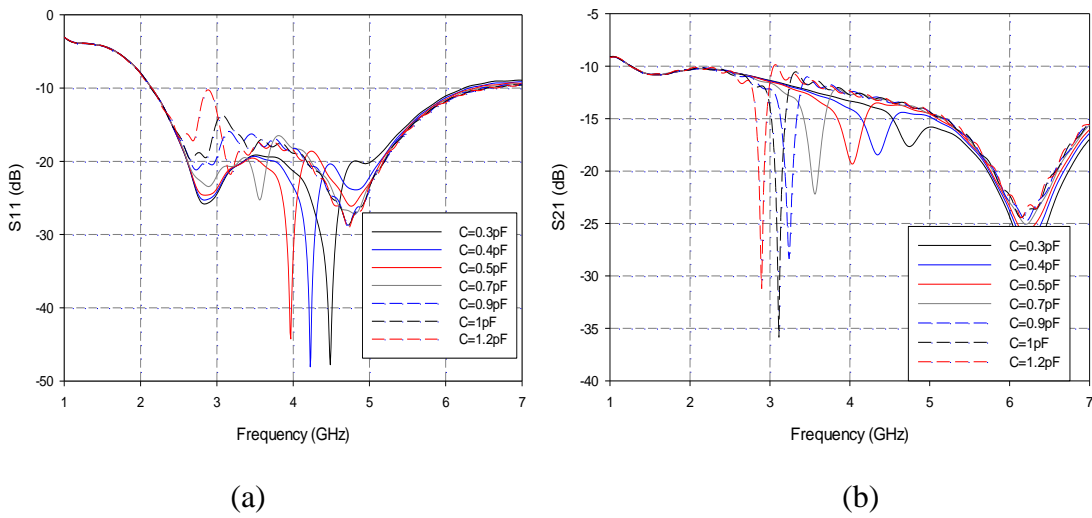

(a)   (b)

Fig. 3.2.3.   Simulated scattering parameters for the UWB antennas with one slit-patch structure for different capacitance values: (a) S_{11} and (b) S_{21}.

TABLE I
SIMULATED ANTENNA EFFICIENCY WITH AND WITHOUT THE PROPOSED SLIT-PATCH
STRUCTURE

| f(GHz) | C(pF) | Total Antenna Efficiency % | |
		Without slit	With slit-patch structure
4.744	0.31	82.02	84.58
4.352	0.41	82.53	86.53
4.032	0.51	81.5	87.77
3.776	0.6	80.8	87.8
3.56	0.7	79.6	86.8
3.392	0.8	78.57	84.5
3.24	0.9	77.6	81.9
3.112	1	76.4	78.56
2.896	1.2	72.9	71

3.3.1.2 *Two Printed UWB Monopoles with Multiple Slit-Patch Structure*

The configuration described in the previous section achieved a reduction of the mutual coupling between the two antennas, but in a narrow frequency range. In order to obtain a more broadband isolation for each of the dynamic tuning states, two slit–patch elements have been employed, resembling more closely the EBG type structure presented in section 3.1.4. The number of slit–patch elements can be further increased to obtain even more broadband isolation, however, in the present work; it is limited to two for simplicity, as a proof of concept. The two slit-patch structures are situated in the ground plane as shown in Fig. 3.2.4. The periodicity of the resulting EBG structure is 10mm and the geometry of each unit cell is the same as the one of the single slit–patch structure.
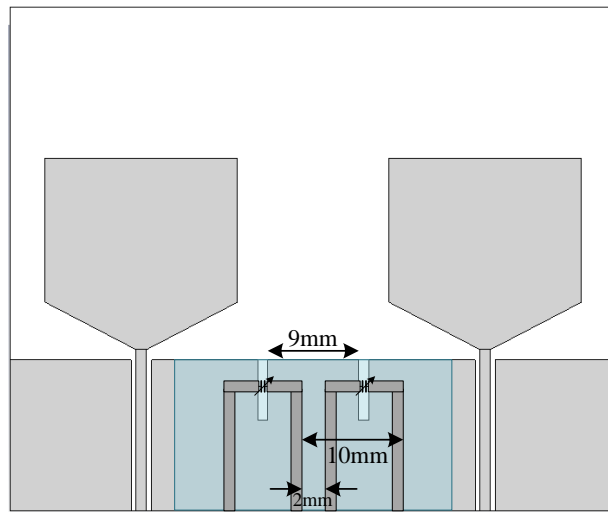
Fig. 3.2.4.   Schematic diagram of the antenna array with two slit-patch structures.

Two cases have been investigated. The first consists of two same length slits, while the second is perturbed where one slit has length l_1=6mm and the second has length l_2=6.5mm. The perturbed case has been inspired from the measured result in Fig. 3.1.12(c), where one varactor had different capacitance value resulting in a more broadband band-gap. The simulated S–parameters for three capacitance values are presented in Fig. 3.2.5 for both cases.

It can be observed from Fig. 3.2.5(b) that the transmission zero produced in the S_{21} response is more broadband than the one obtained from the single slit-patch structure, while it is evident that the perturbed case results in an even more broadband reduction of the mutual coupling. Moreover, the achieved tuning of the unperturbed case for the selected capacitance values is from 3.4GHz to 4.5GHz while for the perturbed case it is from 3.28GHz to 4.3GHz. Further tuning towards higher frequencies could be achieved for smaller capacitance. On the contrary, the use of higher capacitance affects the S_{11} as in the case of a single slit–patch. Fig. 3.2.6 illustrates a better comparison in terms of achieved bandwidth for the three different structures. The instantaneous bandwidth for each capacitance/voltage value is presented in Fig. 3.2.7 for the three configurations. The bandwidth has been defined as the frequency range with isolation of at least 17.5dB while without the slit-patch structures the obtained isolation in the area of interest is between 10dB and 15dB. It is evident from the graph that the configuration that gives more broadband reduction is the one with the two perturbed slits. The simulated total efficiency for the two slit-patch structures is 80% or more in the region of the mutual coupling reduction and is better than the case of no slit-patch structure.
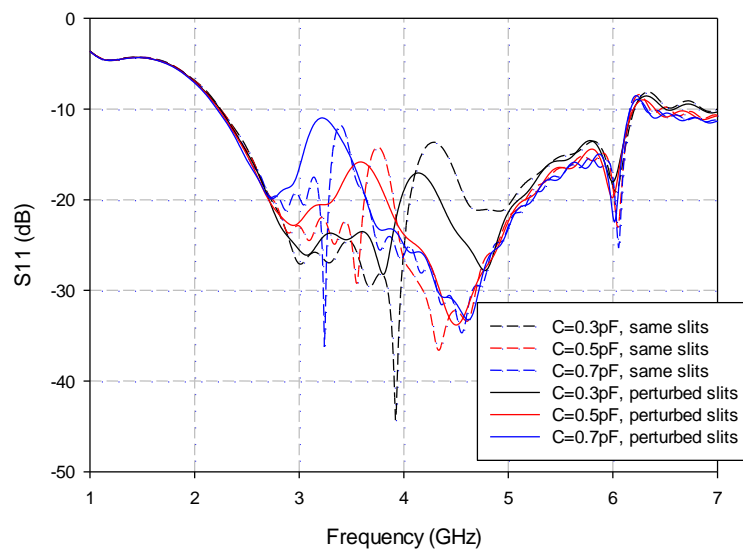
(a)
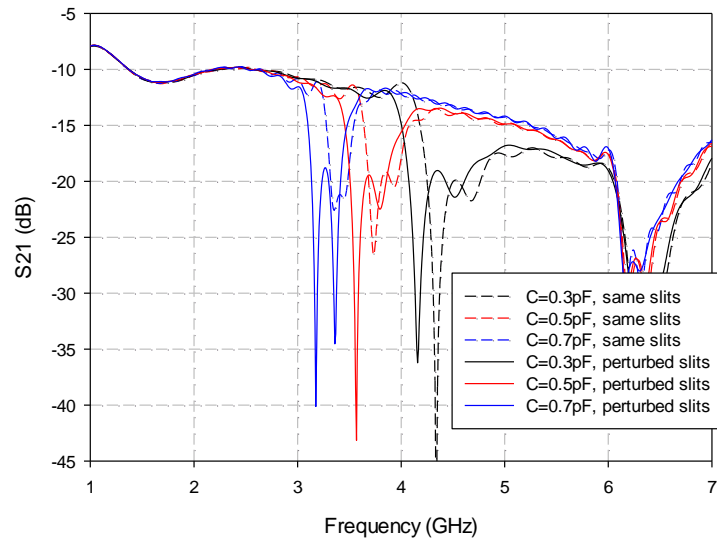
(b)

Fig. 3.2.5.   Simulated scattering parameters for the UWB antennas with two slit-patch structures with the same and different length slits, for different capacitance values: (a) S_{11} and (b) S_{21}.
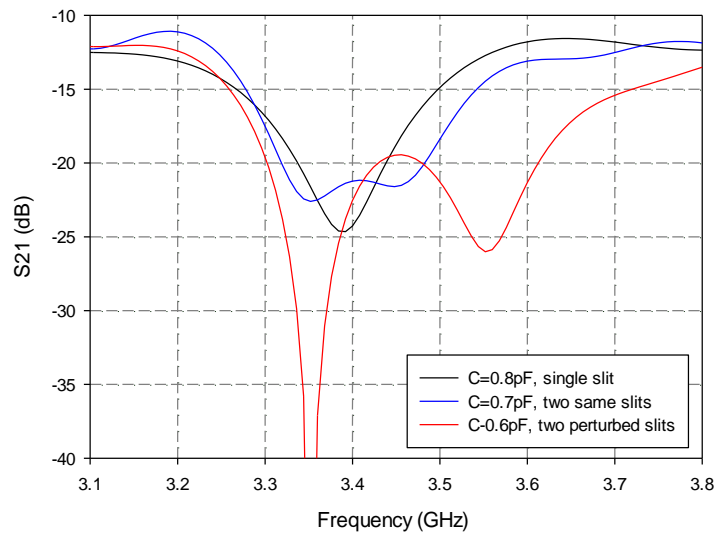

Fig. 3.2.6.   Comparison of S_{21} for the UWB antennas with one slit-patch structure and two slit-patch structures with the same and different length slits.
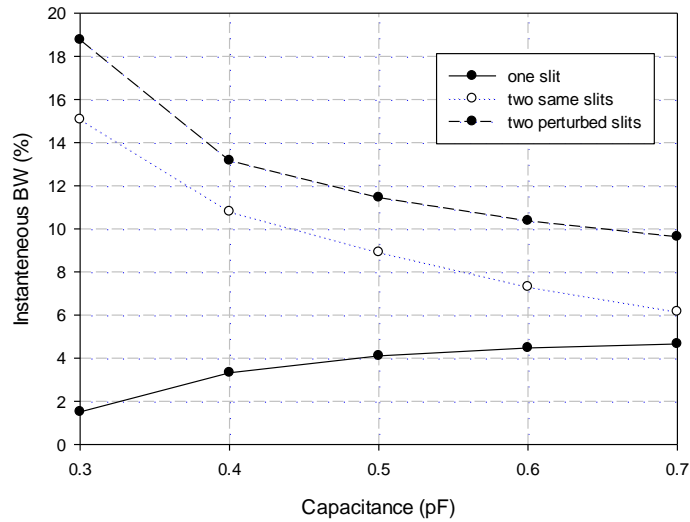
Fig. 3.2.7.   Comparison of isolation bandwidth versus capacitance for the UWB antennas with one slit-patch structure and two slit-patch structures with the same and different length slits.

3.2.1.3 *Measurements of Fabricated Prototypes*

Prototypes of the antenna array with the single slit element (Fig. 3.2.8) and the two perturbed slits (Fig. 3.2.10) have been fabricated in order to validate the simulation results. Initially, the configuration with the single slit was measured. Before the measurements, the polyester film has been aligned with the FR-4 board and glued to it. The varactor used for this prototype was the SMV1231 from Skyworks. The S-parameters of the monopoles have been measured and the S_{21} for five capacitance values is shown in Fig. 3.2.9(b). As expected, a transmission minimum is observed which is tuned when the biasing voltage changes. An isolation of at least 18dB is obtained throughout the tuning range. Compared with the simulation results, the measured S_{21} minimum is slightly higher and slightly shifted in frequency for all capacitance values. This can be attributed to a weaker coupling between the patch and the slit as explained in section 3.1.6 due to air gaps formed between the film and the

ground during the soldering of the varactor on the thin film. Furthermore, the presence of the glue slightly alters the thickness of the film. Indeed, new simulation results have been produced for this configuration assuming an air gap of 38μm and a 70μm thick polyester film, yielding a good agreement with the measured results (Fig. 3.2.9b). For the capacitance range used, the antennas are well matched with S_{11} values below −10dB as can be observed from Fig. 3.2.9(a).
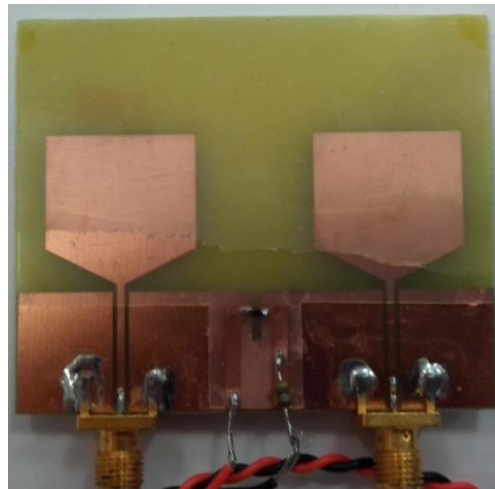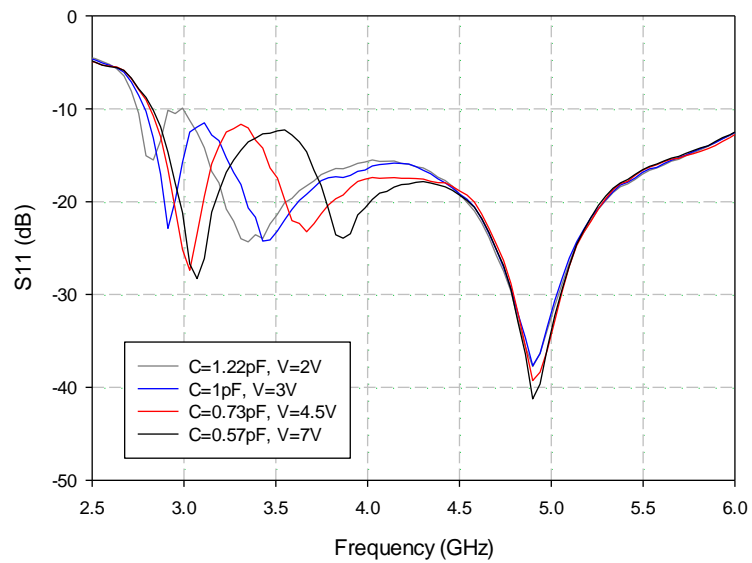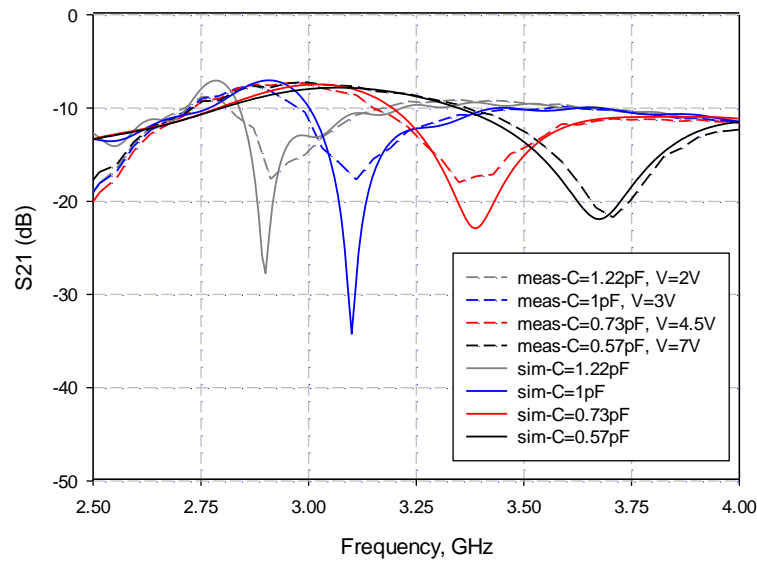

Fig. 3.2.8. Photograph of the fabricated prototype of the structure with the UWB antennas and one slit-patch structure.

(a)

(b)

Fig. 3.2.9.   Measured S-parameters of the UWB antennas with one slit-patch structure for different voltages: (a) S_{11}, (b) S_{21}.

Subsequently, the antenna array with two perturbed slit-patch structures shown in Fig. 3.2.10 has been measured. The varactor diodes used in this case were the SMV2019 from Skyworks. The measured S_{11} for three biasing voltages is illustrated in Fig. 3.2.11(a), along with the corresponding simulation results. It can be seen that the antennas are well matched with S_{11} values below −10dB. From the measured S_{21}, shown in Fig. 3.2.11(b) it is evident that a broadband isolation is obtained of at least 19dB. Moreover significant tuning is achieved which is in good agreement with the simulation results, also included in the graph.
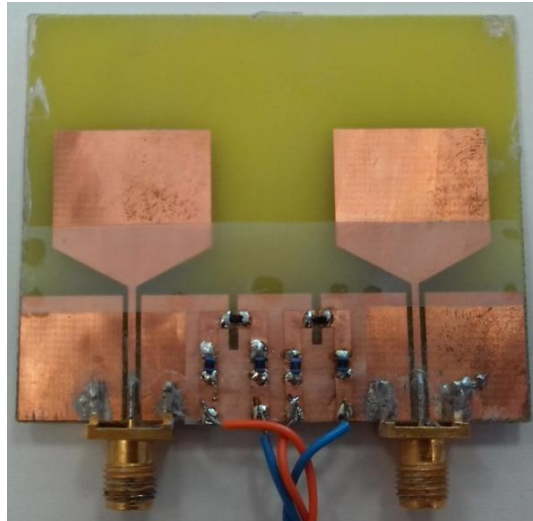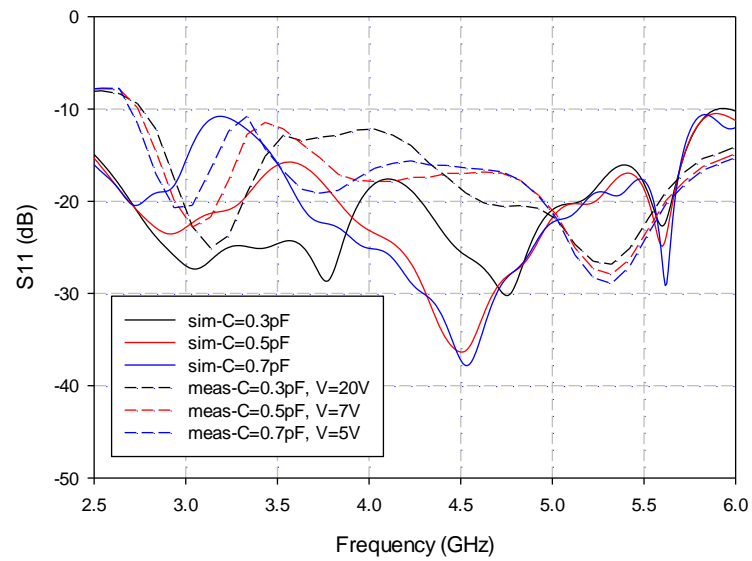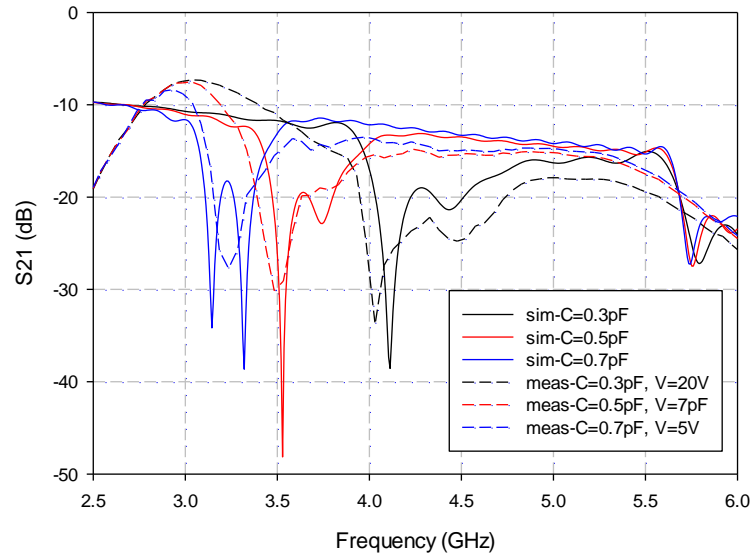
Fig. 3.2.10.   Photograph of the fabricated prototype of the structure with the UWB antennas and two slit-patch structures with different length slits.

(a)

(b)

Fig. 3.2.11.   Measured and simulated S-parameters of the UWB antennas with two perturbed slit-patch structures for different voltages: (a) S_{11}, (b) S_{21}.

3.2.2 Tunable Closely Spaced Monopoles with Tunable Isolation

In the previous section it has been proven via simulation and experimental results that the proposed tunable EBG structures can be employed to achieve a tunable isolation enhancement for closely spaced antennas. UWB monopoles were employed in order to demonstrate the tuning range of the EBG structures. However, the proposed tunable structures can be also employed for the mutual coupling reduction of tunable antennas in a practical system. Significantly, the proposed two-layer biasing technique can also be employed to design tunable antennas with a simplified biasing network. Here, tunable monopole antennas have been designed utilizing the two-layer biasing technique and are used to replace the UWB monopoles of the previous section.

71

3.2.2.1 *Design of Tunable Monopole Antenna*

The concept of the antenna design is based on the idea presented in [10, 11] and later extended in [12]. Initially, one antenna has been designed starting from the UWB monopole design employed thus far in this Chapter. Two slits have been etched off the ground plane of the monopole antenna as shown in Fig. 3.2.12(a). The dimensions of the slits are included in the figure. These slits affect the antenna's impedance matching and thus create a narrowband response as illustrated in Fig. 3.2.13(a). The figure presents a comparison of the S_{11} response for one UWB monopole and the narrowband monopole produced with the introduction of the slits. It can be seen that for the specific dimensions the monopole's operating frequency is around 6.8GHz. This response is then tuned by employing the concept of a closely coupled, varactor-loaded patch. The schematic diagram of the structure is depicted in Fig. 3.2.12(b) while the corresponding S_{11} response for different values of the varactor is presented in Fig. 3.2.13(b). It can be observed that with the introduction of the varactor-loaded patch the operating frequency assumes lower values (between 3GHz and 5GHz for the specific capacitances) due to the coupling of the slits and the patches, as expected.
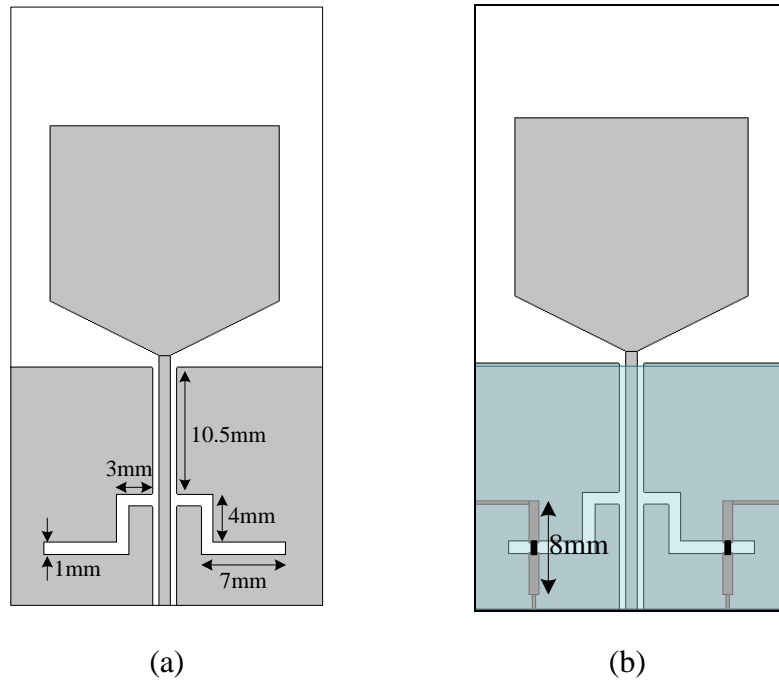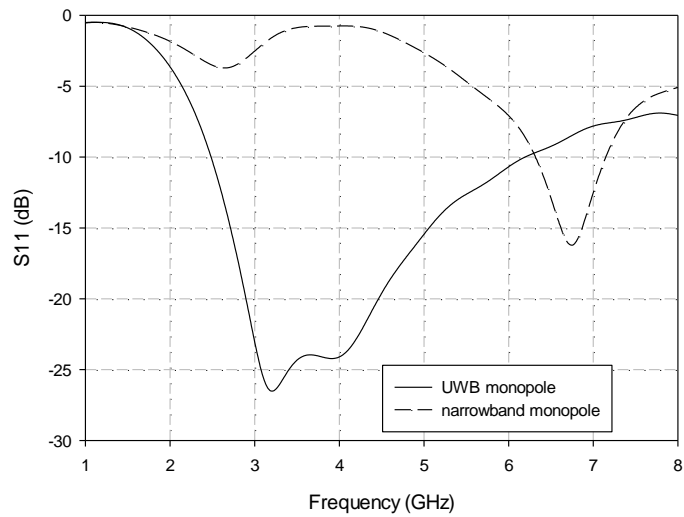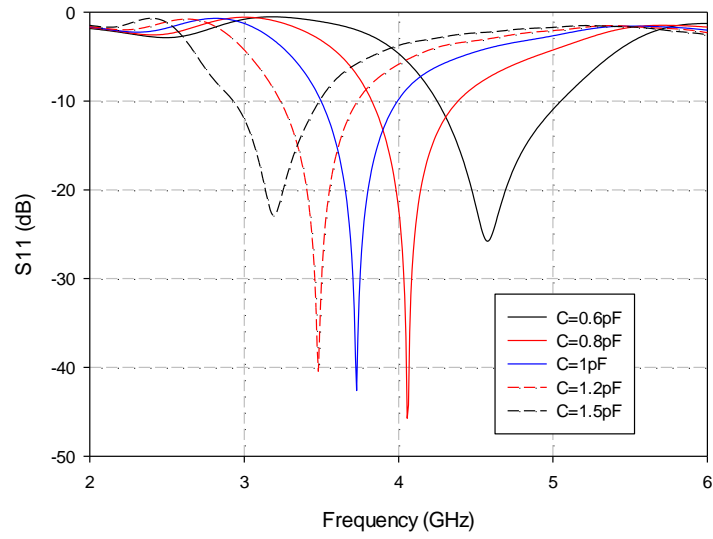
Fig. 3.2.12. Schematic diagram of (a) static narrowband antenna with slits etched off the ground and (b) tunable narrowband antenna using varactor loaded patches.

(a)

(b)

Fig. 3.2.13.   Simulated S_{11} response for (a) one UWB monopole and one static narrowband antenna and (b) one tunable narrowband antenna for different capacitance values.

3.2.2.2 *Array of Two Tunable Monopoles with Tunable Slits*

The two tunable monopoles are placed at the same distance as the UWB monopoles in the previous section, employing two equal length slit-patch structures in their common ground. A schematic diagram of the complete structure including the biasing lines for all 6 used varactors (two in the EBG structure and two for each antenna) is presented in Fig. 3.2.14. It must be noted that the biasing network for each antenna in this structure is significantly simplified compared to the corresponding single layer varactor-loaded tunable antennas and slots presented in [10-12]. In Fig. 3.2.15, the S_{11} of the antennas is shown for different capacitance C_2, achieving a wide tuning range from 4.6GHz to 3.1GHz (central frequency of each band). It should be pointed out that in order to achieve the optimum isolation in each operating band, different capacitance values were used for the EBG structure than the antennas, referred to with the parameter C. The values of C and C_2 in each case are shown in the legend of the graph. The range of capacitances for the EBG structures is from 0.3pF to
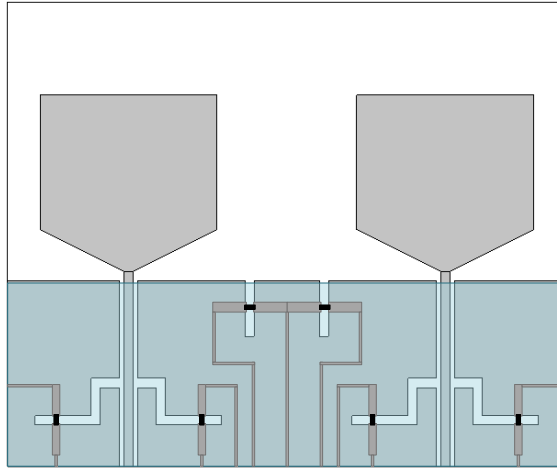
74

about 0.9pF.

Fig. 3.2.14.   Schematic diagram of the tunable closely spaced antennas with two slit-patch structures.
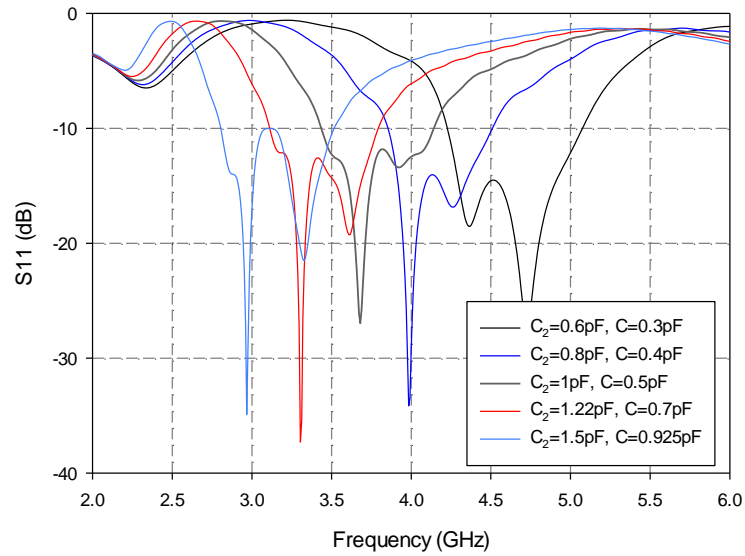

Fig. 3.2.15.   Simulated S_{11} of the tunable antennas with two slit-patch structures for different capacitance values.

Fig. 3.2.16(a), (b), and (c) illustrate the S_{11} and corresponding S_{21} response with and without the tunable EBG structure for three states, namely for C_2=0.6pF, C_2=1pF and C_2=1.5pF. It can be observed from the figures that the operating bandwidth of the monopoles

in each case is slightly increased with the presence of the EBG structure while the isolation is significantly enhanced in the corresponding band. More specifically, the in band isolation for $0.6pF \leq C_2 \leq 1.5pF$ has been improved by at least 7dB while in some cases the improvement has been of 20dB. A more detailed comparison of the proposed tunable antennas with and without the tunable slit-patch structures is given in Table II in terms of isolation and efficiency.
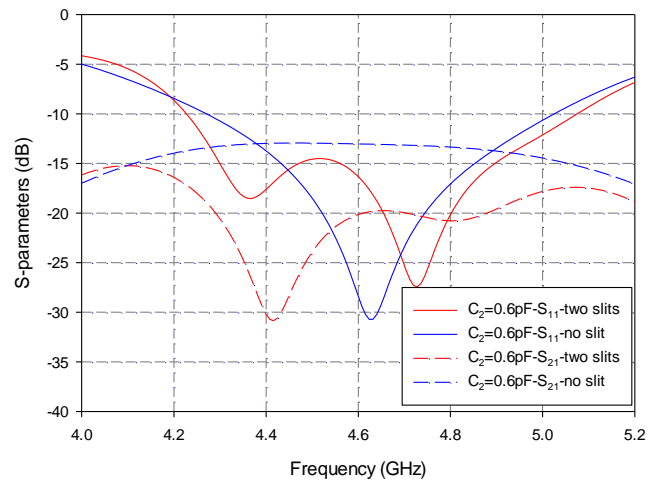
(a)
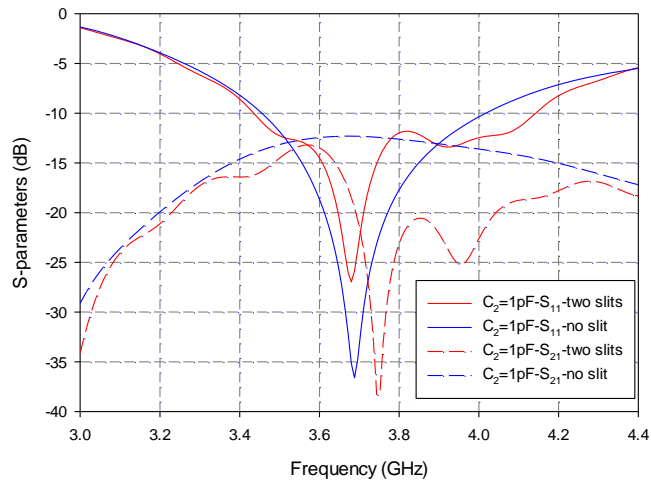
(b)
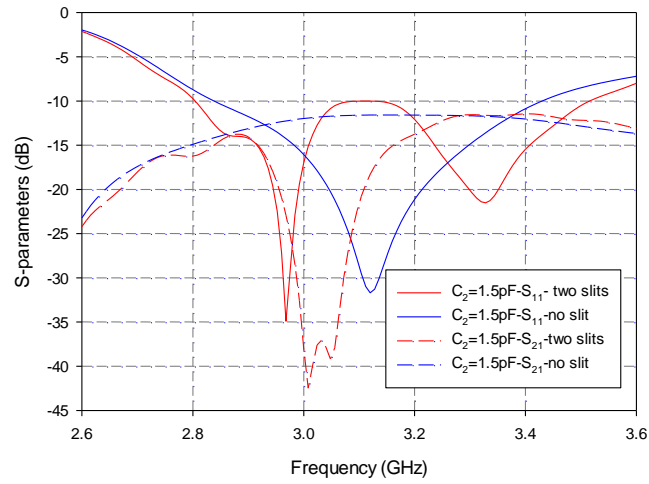
(c)

Fig. 3.2.16. Comparison of S_{11} and S_{21} with and without the proposed EBG structures for
(a) C_2=0.6pF, (b) C_2=0.1pF and (c) C_2=1.5pF.

TABLE II
SIMULATED TOTAL EFFICIENCY FOR TUNABLE ANTENNA WITH AND WITHOUT THE PROPOSED
SLIT-PATCH STRUCTURE

f_c (GHz)	C_2 (pF)	C (pF)	no slit-patch S_{21} at f_c (dB)	2 slit-patch S_{21} at f_c (dB)	η_{tot} % without slit-patch at		η_{tot} % with 2 slit-patch at	
					f_c	f_{S21min}	f_c	f_{S21min}
4.65	0.6	0.3	-13.1	-19.8	77.7	76.1	83.6	81.8
4.4	0.7	0.35	-13	-20.1	77.9	79.2	85.5	79.8
4.18	0.8	0.4	-12.8	-20	78.5	80.1	85.9	80.4
3.98	0.9	0.45	-12.8	-20.6	78.1	79.8	85.6	77.7
3.79	1	0.5	-12.6	-25	78.9	80.1	80.3	77.2
3.62	1.1	0.625	-12.3	-24.5	79	80.7	83.6	77.1
3.45	1.22	0.7	-12	-26.8	80.6	79.8	82.5	77.2
3.27	1.4	0.8	-11.6	-30.1	81.2	81.4	79.7	81
3.16	1.5	0.925	-11.6	-15.1	79.3	77.2	78.7	79.4

Although the above results consist in estimated and no experimental performance, the design dimensions and the capacitance values can be achieved. Moreover, the agreement of the measured and simulated results of the other configurations investigated in this thesis

77

suggests the same for the proposed closely spaced tunable monopoles with tunable mutual coupling reduction.

3.3 CONCLUSIONS

Novel tunable two-layer slot-patch Electromagnetic Band-Gap (EBG) structures have been presented in this Chapter with significantly simplified biasing network. A wide tuning of the EBG's stop-band has been achieved by changing the voltage applied to the varactors incorporated to the structure which are electrically isolated from the metallic plane. As a practical application, the proposed tunable EBG structures have been employed in the common ground plane of two closely spaced printed wideband monopole antennas, significantly reducing the mutual coupling between them. Simulation results and measurements of fabricated prototypes have been presented. Moreover, tunable monopoles have been designed using the proposed two-layer biasing technique and an isolation between them has been achieved using the proposed tunable EBG structures. The proposed tunable EBG structures, tunable antennas and the simplified two-layer biasing technique presented in this Chapter can be applied to a number of different applications involving electrically tunable structures with simplified biasing networks.

REFERENCES

[1] G. Exposito-Dominguez, J. M. Fernandez-Gonzalez, P. Padilla, M. Sierra-Castaner, "Mutual Coupling Reduction Using EBG in Steering Antennas," *IEEE Antennas Wireless Propag. Lett.*, vol. 11, pp. 1265-1268, 2012.

[2]   P. N. Fletcher, M. Dean, and A. R. Nix, "Mutual coupling in multi-element array antennas and its influence on MIMO channel capacity," *Electron. Lett.*, vol. 39, no. 4, pp. 342–344.

[3]   S. Lu, T. Hui, and M. Bialkowski, "Optimizing MIMO channel capacities under the influence of antenna mutual coupling," IEEE Antennas Wireless Propag. Lett., 2008, 7, pp. 287–290.

[4]   C.-Y. Chiu, C.-H Cheng, R.D. Murch, and C. R. Rowell, "Reduction of mutual coupling between closely packed antenna elements," *IEEE Trans. Antennas Propagat.*, vol. 55, no. 6, pp. 1732–1738, Jun. 2007.

[5]   T. Kokkinos, E. Liakou, and A. P. Feresidis, "Decoupling antenna elements of pifa arrays on handheld devices," *Electron. Lett.*, vol. 44, no. 25, pp. 1442-1444, Dec. 2008.

[6]   F. Yang, and Y. Rahmat-Samii, "Microstrip antennas integrated with electromagnetic band-gap (EBG) structures: a low mutual coupling design for array applications," *IEEE Trans. Antennas Propagat.*, vol. 51, pp. 2936-2944, Oct. 2003.

[7]   N. Llombart, A. Neto, G. Gerini and P. de Maagt, "Planar circularly symmetric EBG structures for reducing surface waves in printed antennas," *IEEE Trans. Antennas Propagat.*, vol. 53, no. 10, pp. 3210-3218, Oct. 2005.

[8]   E. Rajo-Iglesias, O. Quevedo-Teruel, L. Inclan-Sanchez, "Mutual coupling reduction in patch antenna arrays by using a planar EBG structure and a multilayer dielectric substrate," *IEEE Trans. Antennas Propagat.*, vol. 56, no. 6, pp. 1648-1655, Jun. 2008.

[9]   Q. Li, A. P. Feresidis, M. Mavridou, P. S. Hall, "Miniaturized double-layer EBG structures for broadband mutual coupling reduction between UWB monopoles," *IEEE Trans. Antennas Propagat.,* in press.

[10] M. R. Hamid, P. Gardner, P. S. Hall, and F. Ghanem, "Switched-band Vivaldi antenna," *IEEE Trans. Antennas Propagat.*, vol. 59, no. 5, pp. 1472–1480, May 2011.

[11] M. R. Hamid, P. Gardner, P. S. Hall, and F. Ghanem, "Vivaldi antenna with switchable band pass resonator," *IEEE Trans. Antennas Propagat.*, vol. 59, no. 11, pp. 4008–4015, Nov. 2011.

[12] A. Tariq and H. Ghafouri-Shiraz, "Frequency-reconfigurable monopole antennas," *IEEE Trans. Antennas Propag.*, vol. 60, no. 1, pp. 44–50, Jan. 2012.

CHAPTER 4.

TUNABLE HIGH IMPEDANCE SURFACES FOR LOWER MILLIMETRE-WAVE FREQUENCIES

High Impedance Surfaces (HIS), as briefly explained in Chapter 1, are eligible for numerous applications such as ground planes in printed antennas [1] or in resonant cavity antennas for reducing their profile [2, 3]. Other applications of HIS type structures include reflectarrays [4], polarisation converters [5] and holographic surfaces [6]. Furthermore, several tunable HIS structures have been proposed in the past few years using active components such as varactor diodes [7-9]. These components have been successfully employed for applications at low microwave frequencies, but are not suitable for higher frequencies mainly due to high losses and parasitic effects.

As an effort to overcome these limitations, new designs of tunable HIS are studied in this Chapter, for low millimetre-wave frequencies. A novel low-loss technique for tuning HIS is presented and experimentally demonstrated. The tuning is achieved by virtue of employing a small number of piezoelectric bender actuators that can achieve a displacement under a DC bias. It is important to note that the actuators are placed around the HIS arrays, thereby not interfering with its radiation performance and hence resulting in a particularly low loss structure, which is especially challenging at mm-wave frequencies. The displacement produced by the actuators when they are biased with a DC voltage, alters the distance between the periodic arrays and the ground plane forming the HIS structures. This results in a change of the reflection phase response of the structures under investigation. Three designs are being investigated, operating at 15GHz and at 30GHz. Simulation results demonstrate that the proposed configurations can be employed as dynamic impedance surfaces obtaining

significant phase shift with a low-loss performance. Moreover, measurements are presented for the first design validating the simulated results. Finally, as a practical application, a dipole antenna is presented, placed above the proposed tunable HIS, obtaining a significant tuning of its operational frequency.

4.1 TUNABLE HIS STRUCTURES

Each of the three investigated HIS structures, consists of a doubly periodic array of metallic elements printed on a dielectric substrate which is placed at close proximity over a ground plane. In typical implementations of HIS structures, the substrate is grounded, creating a dielectric filled cavity between the array and the ground plane. Nevertheless, in the proposed configurations, an air cavity is created giving an extra degree of freedom for controlling the HIS reflection phase response. The first two designs exhibit a single resonance for a specific cavity thickness, while the third is multi-resonant. The tuning is achieved by means of piezoelectric bender actuators which support the upper layer (dielectric substrate with periodic array) of the structure (Fig. 4.1.1). A displacement is produced by the actuators when they are biased with a DC voltage, changing thus the cavity distance. This results in a dynamic tuning of the reflection phase response of the structure which is strongly dependant on this parameter as expected from (2.1-7), since as explained in section 2.1.3 the HIS performance is related to the resonance of the open cavity formed between the periodic array and the ground.
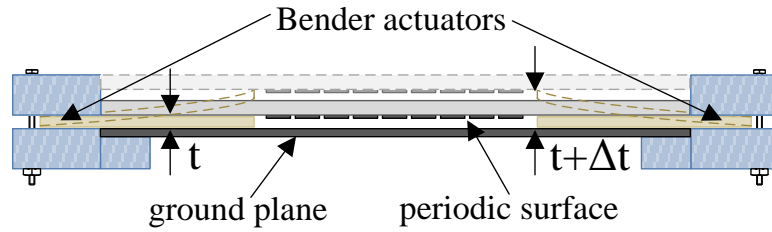
Fig. 4.1.1.   Schematic diagram of proposed tunable HIS (dimensions are not to scale).

4.1.1 Design of HIS for Operation at 15GHz

Initially, a tunable HIS operating around 15GHz is designed. The proposed High Impedance Surface consists of a doubly-periodic array of square loop metallic elements printed on a 0.055mm thick dielectric substrate with $\varepsilon_r=3$ and $\tan\delta=0.0018$ placed at distance t from a ground plane. The unit cell of the proposed tunable HIS is shown in Fig. 4.1.2(a, b). The periodicity of the structure is $p=6.5$mm, the outer dimension of the square loop is $d_l=5.57$mm, the inner square loop dimension is $d_a=3.34$mm and the initial cavity thickness is set to $t=0.6$mm. The dimensions and the geometry of the structure have been chosen so that a reflection phase of zero is obtained at around 15GHz with a fast variation of the reflection phase with frequency which makes the structure more sensitive to changes of the cavity distance. This means that a large phase shift can be achieved. Nevertheless there is a trade-off between the bandwidth and the losses that should be taken into account when designing the surface. A quick response in the phase of the reflection coefficient, i.e. a narrow bandwidth, results in a low value of the reflection magnitude which in turn corresponds to more losses.
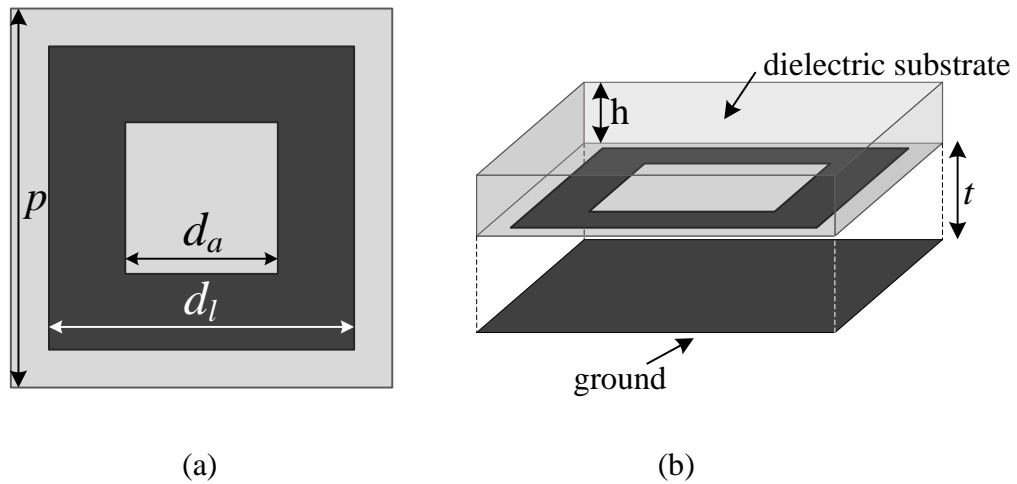
Fig. 4.1.2.   Unit cell of the HIS array: (a) top view, (b) perspective (dimensions are not to scale).

As mentioned above, the periodic surface is supported by bender piezoelectric actuators placed between the ground plane and the periodic surface. A change in the biasing voltage of the bender actuators is translated to a bending of the actuators and thus a vertical displacement of the surface with respect to the ground plane as illustrated in Fig. 4.1.1. In order to evaluate the tuning range and the maximum phase shift that can be achieved from the proposed HIS, simulations have been carried out in CST Microwave Studio[TM] simulation software. The displacement achieved by the bender actuators is modeled in the software as a parametric change of the cavity thickness t.

Periodic boundary conditions have been employed to reduce the calculations of an infinite structure into a single unit cell and full wave analysis has been carried out in CST with normally incident plane wave excitation to extract its reflection characteristics. The simulated phase of the reflection coefficient is shown in Fig. 4.1.3(b) for different cavity distances which correspond to a displacement from zero (t=0.6mm) to 1.6mm (t=2.2mm). The corresponding reflection magnitude is shown in Fig. 4.1.3(a). For a displacement Δt of just 0.4mm, a 142$^\text{o}$ phase shift has been obtained for operation at 15GHz while for Δt=1.6mm the

obtained phase shift at the same frequency is about 190°. The maximum phase shift for this displacement is 243° at 13.46GHz (Fig. 4.1.3c). Furthermore, the frequency where the AMC response occurs, i.e. where the reflection phase is equal to zero, is tuned from 15.53GHz to 10.85GHz for $\Delta t = 1.6$mm.

It is worth noting that as the cavity thickness increases, the HIS resonance is weaker and the slope in the reflection phase is decreased (increased bandwidth). This results in a non linear tuning of the phase response. This is shown more clearly in Fig. 4.1.3(c) where the phase shift $\Delta\varphi$ versus the displacement Δt is depicted for frequencies 13.46GHz and 15GHz. In the same figure the fractional bandwidth of the HIS is shown for each displacement, which increases significantly for larger displacement. It is evident that there is a tradeoff between the tunability and the bandwidth, since for example at 15GHz from Δt=1mm to Δt=1.6mm the phase shift increases just by 11.4^{o} while the bandwidth of the AMC resonance is over 30%.
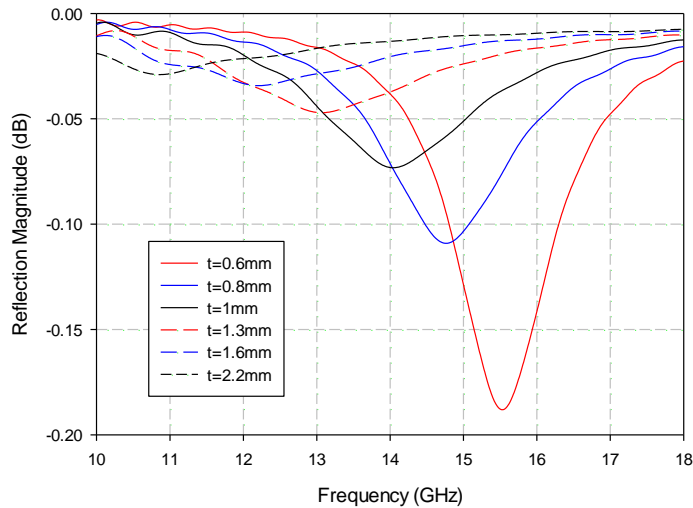
(a)
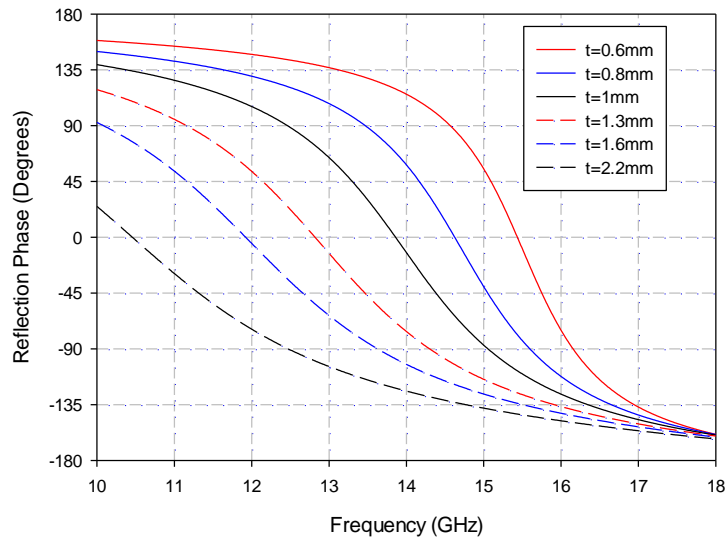
(b)
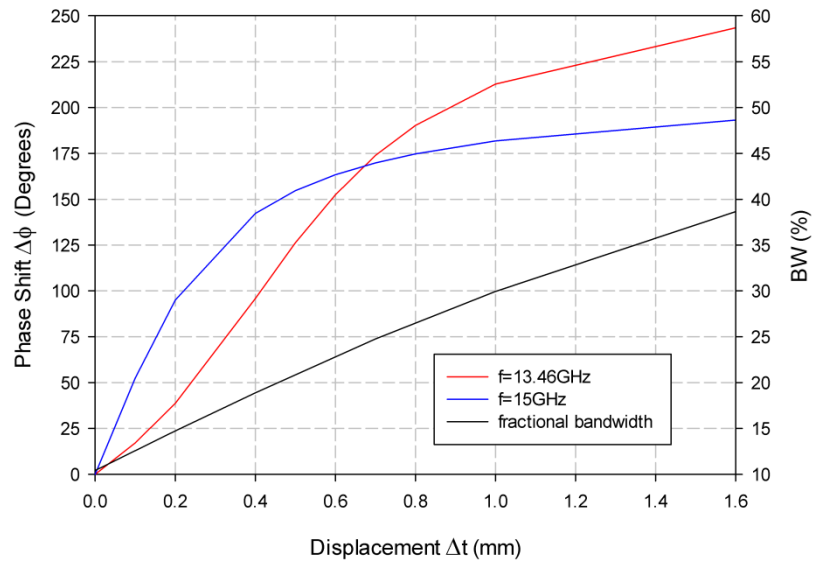

(c)

Fig. 4.1.3.   Simulated reflection (a) magnitude and (b) phase of the proposed HIS for different cavity thicknesses. (c) Phase shift for f=13.46GHz and f=15GHz and fractional bandwidth of the AMC resonance versus displacement.

4.1.2 Design of HIS for Operation at 30GHz

In this section a scaling of the proposed structure is presented for operation at the mm-wave region. The HIS is composed from the same type of elements (Fig. 4.1.2a, b) printed on a 0.8mm thick dielectric substrate with ε_r=2.2 and tanδ=0.009 (TLY-5 from Taconic^{TM}). The dimensions have been changed with the aim of obtaining an HIS resonance at around 30GHz. The new dimensions are p=1.8mm, d_l=1.6mm and d_a=1.3mm. The initial cavity thickness is set to t=0.3mm.

The unit cell of the new structure has been simulated to extract the reflection characteristics of the HIS. The magnitude of the reflection coefficient for different cavity thicknesses from t=0.3mm to t=0.9mm is presented in Fig. 4.1.4(a). The corresponding reflection phase is shown in Fig. 4.1.4(b). In this case, at 30GHz, a phase shift of 185.8^o is obtained for a displacement Δt of 0.3mm, while for Δt=0.6mm the obtained phase shift is 220°. It can be observed that although there is a great dependence between the cavity distance and the frequency of the AMC response, the other geometry parameters significantly affect the phase response. This argument can be supported if one observes the resonant frequency for t=0.6mm, which for the new structure is 26.85GHz. Moreover, a low-loss operation is obtained with the magnitude of the reflection coefficient being over -0.3dB for all cavity thicknesses.
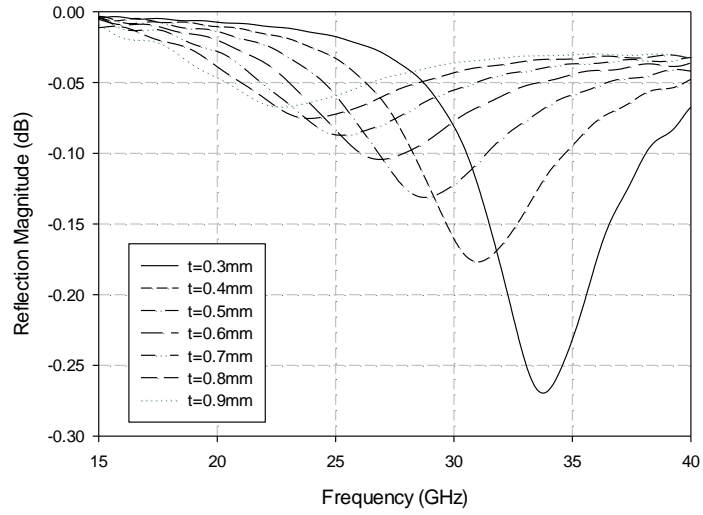
(a)
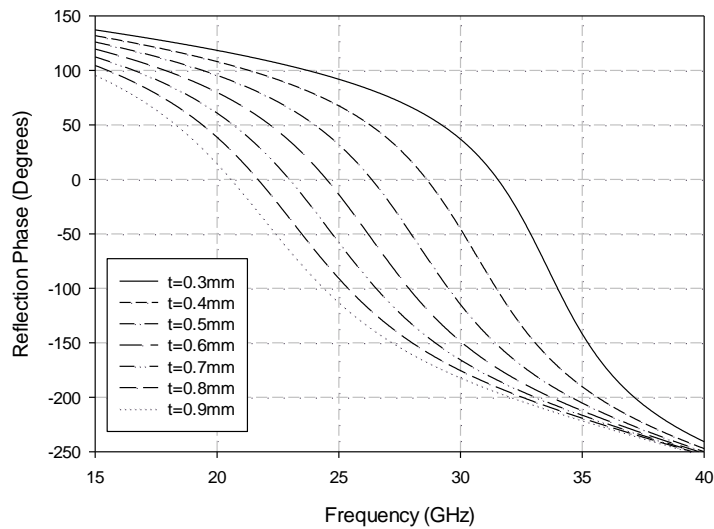
(b)

Fig. 4.1.4.   Simulated reflection (a) magnitude and (b) phase for different cavity thicknesses for operation at 30GHz.

This study demonstrates that the proposed configuration operating around 30GHz achieves larger tuning range compared with the 15GHz design with the same or even less displacement from the actuators. This is also evident from Table I which shows the maximum phase shift $\Delta\varphi$ obtained for a displacement Δt=0.4mm from the two proposed tunable HIS structures.

Furthermore, it validates the concept of employing the piezo-tunable HIS for operation at higher frequencies.

TABLE I
COMPARISON OF TWO TUNABLE HIS DESIGNS IN TERMS OF ACHIEVED PHASE SHIFT FOR FIXED DISPLACEMENT (ΔT=0.4MM)

Tunable HIS	f(GHz)	Δφ (Degrees)
Design 1	15	142°
Design 2	30	202.7^o

4.1.3 Multi-Resonant Elements for Broadband Tunable HIS

The two tunable HIS designs that have been presented in this Chapter so far, exhibit a single resonance response for a specific cavity thickness. This implies that although they achieve a significant phase shift, they can be operated as phase shifting surfaces at a specific frequency or for a very narrow frequency range depending on the required phase shift. In this section, a multi-resonant HIS design is investigated. The unit cell of the structure is shown in Fig. 4.1.5. It consists of two metallic dipole elements of same width, but different lengths printed on a thin dielectric substrate with thickness h=0.055mm, permittivity ε_r=3 and tanδ=0.0018, placed over a ground plane at distance t. The linear dipole geometry was chosen due to its simplicity. However, due to the geometry, this structure is dependant on the polarisation of the incident wave, in contrast to the designs presented thus far which were symmetric for both planes and hence polarisation independent. The dimensions of the structure's geometrical parameters are l_1=8.8mm, l_2=8.4mm, p_x=7.7mm, p_y=10.6mm, and w=0.5mm as illustrated in Fig. 4.1.5(a), while the initial cavity distance is set at t=0.6mm. The same tuning technique is used, employing the bender actuators in order to dynamically change the cavity distance and obtain a phase shift.
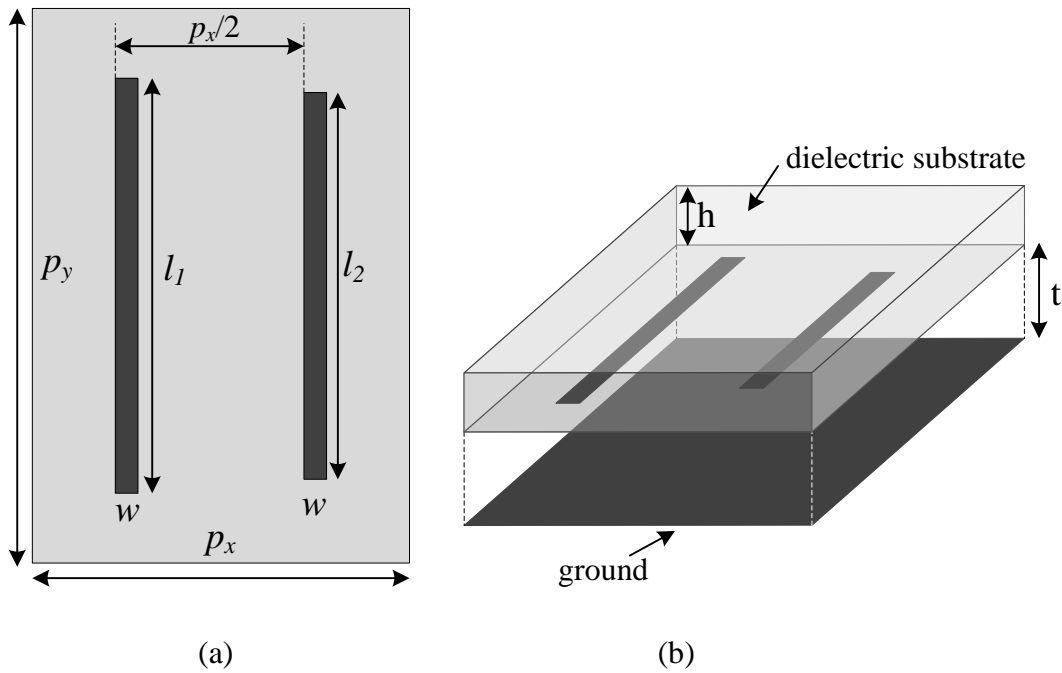
Fig. 4.1.5.   Unit cell of the multi-resonant HIS array: (a) top view, (b) perspective (dimensions are not to scale).

The structure is simulated applying periodic boundary conditions in CST to extract the reflection characteristics of the multi-resonant HIS. The magnitude of the reflection coefficient for different cavity thicknesses from t=0.6mm to t=1.6mm is presented in Fig. 4.1.6(a) with the corresponding reflection phase shown in Fig. 4.1.6(b). Due to the small difference in the length of the two dipoles, two AMC resonances occur at different but close frequencies. This is evident from Fig. 4.1.6, especially for t=0.6mm where the two resonances occur at 14.73GHz and 15.27GHz. As the cavity thickness increases the resonances are shifted to lower frequencies as expected, and they tend to converge. This is caused from the fact that the difference in length of the two dipoles becomes less significant as the frequency decreases. The achieved maximum phase shift from the proposed multi-resonant HIS is 487° for Δt=1mm at 14.38GHz and 280.8^o for Δt=0.4mm at 14.88GHz. The latter is almost doubled compared to the one obtained for the same displacement from the single resonant

HIS presented in section 4.1.1. It should be pointed out that although a $\Delta\varphi=487^o$ does not have a physical meaning since it is over 360°, the obtained result indicates that a phase shift of 360° can be obtained for a range of frequencies. Indeed this can be extracted from Fig. 4.1.7 which presents the phase shift versus frequency for different displacements Δt. It can be observed that a $\Delta\varphi=360^o$ can be obtained for frequencies between 14.18GHz to 14.87GHz, while a $\Delta\varphi=180^o$ can be obtained from 13.39GHz to 15.26GHz by adequately adjusting the biasing voltage of the actuators.
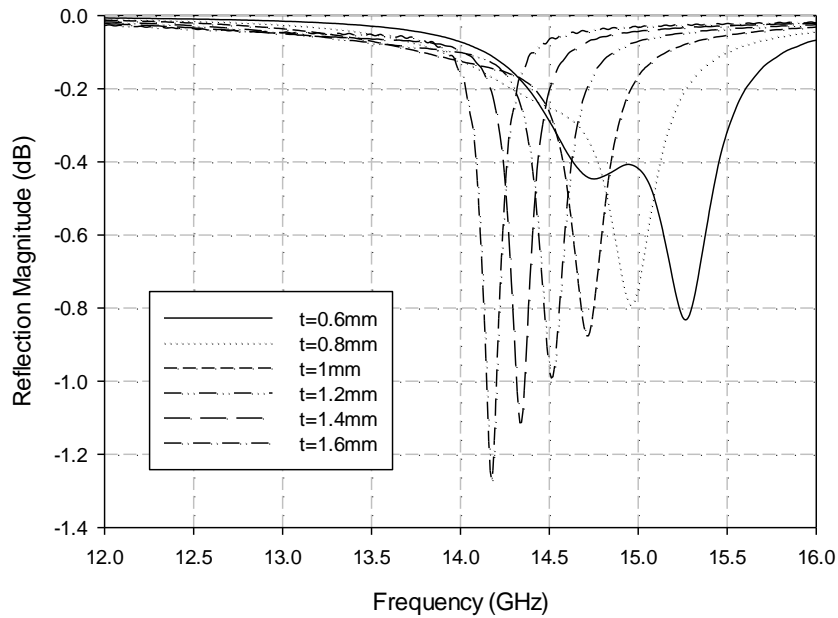
(a)
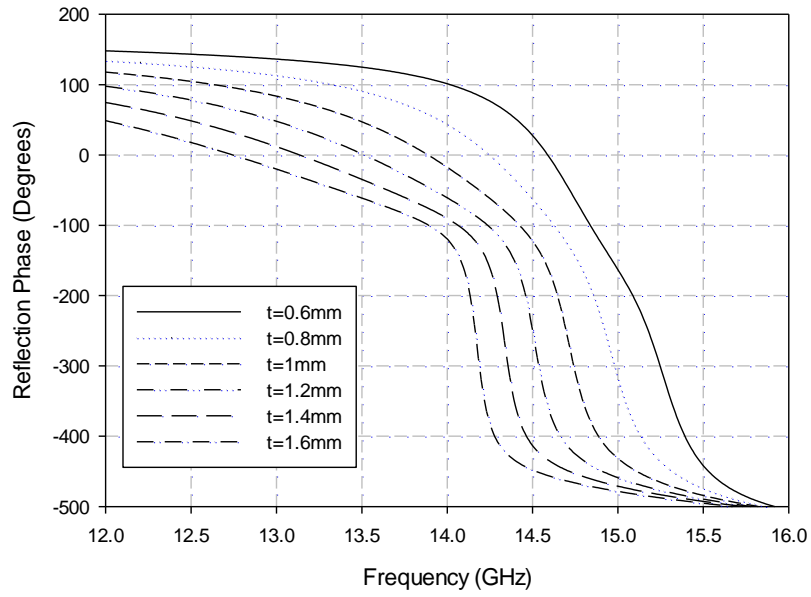
(b)

Fig. 4.1.6.   Simulated reflection (a) magnitude and (b) phase for different cavity thicknesses for the proposed multi-resonant HIS.
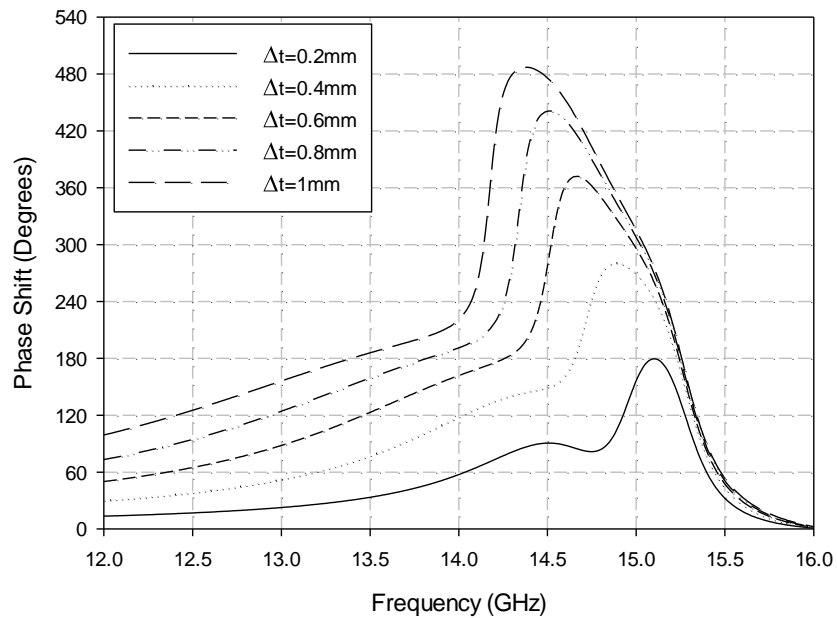

Fig. 4.1.7.   Phase shift versus frequency for different displacement (with respect to t=0.6mm).

4.1.4 Measurements

A prototype of the tunable HIS structure presented in section 4.1.1 has been fabricated and tested to validate the simulation results. A periodic array of 38×38 copper square loop elements printed on a 0.055mm thick, polyester film (ε_r=3) with overall dimensions 240mm×240mm (~12λ×12λ) has been used for the measurement (Fig. 4.1.8a). The periodic surface has been glued to polystyrene foam (ε_r≈1) to make it rigid while keeping it light-weight, and then positioned on top of the ground plane supported by the piezoelectric actuators.

In practice, the maximum tuning range of the structure depends on the maximum displacement produced by the actuators. The operation of the bender actuators proposed for this application has been described in Chapter 2. The particular actuators that have been employed for the measurements are the commercial actuators PL140.11 from Physik Instrumente[TM] (PI) (Fig. 4.1.8b). They are 45mm long, 11mm wide and 0.6mm thick and can achieve a maximum displacement of 1mm for a biasing voltage of 60V with a nominal error of ±20% [10]. Consequently, the initially cavity distance between the ground plane and the periodic array has been set from the thickness of the actuators (~0.6mm) and has then increased by applying voltage to the electrodes.

Two horn antennas have been used to measure the reflection characteristics of the proposed HIS, one as a transmitter and one as a receiver, aiming the structure under test with a small angle of incidence/reflection as illustrated in Fig. 4.1.9. The measured reflection phase for biasing voltages V=0V−60V is presented in Fig. 4.1.10. Significant tuning has been achieved with the AMC (zero phase) frequency shifting from 15.2GHz to slightly less than 13GHz. In addition a significant phase shift (Δφ) has been obtained from the proposed tunable HIS with the maximum Δφ of 177.4$^{\mathrm{o}}$ observed at about 14GHz. The corresponding magnitude

is not shown here, since due to the very low losses of the structure, there was no prominent resonance but just a 0.5dB ripple below zero over the measured frequency range caused by standing wave reflections during the measurement. Although the concept of the proposed design has been validated from the measurements, a comparison with the simulated performance (also included in Fig. 4.1.10) has shown that the actual displacement that has been achieved from the actuators was about 0.8mm instead of 1mm, which is within the initial expected error of the supplied actuators.

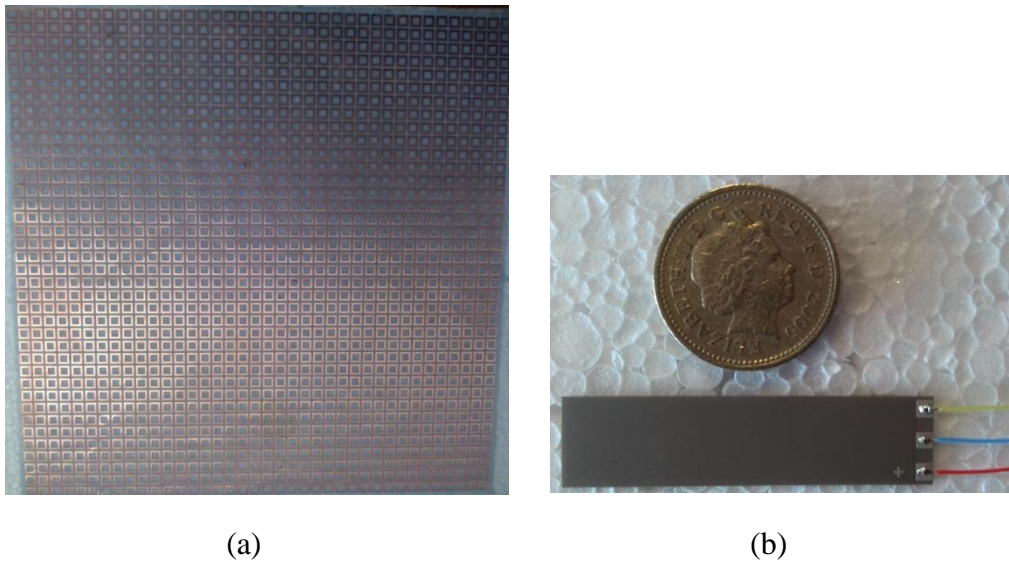(a)   (b)

Fig. 4.1.8.   Photograph of (a) fabricated periodic surface and (b) of a bender actuator.
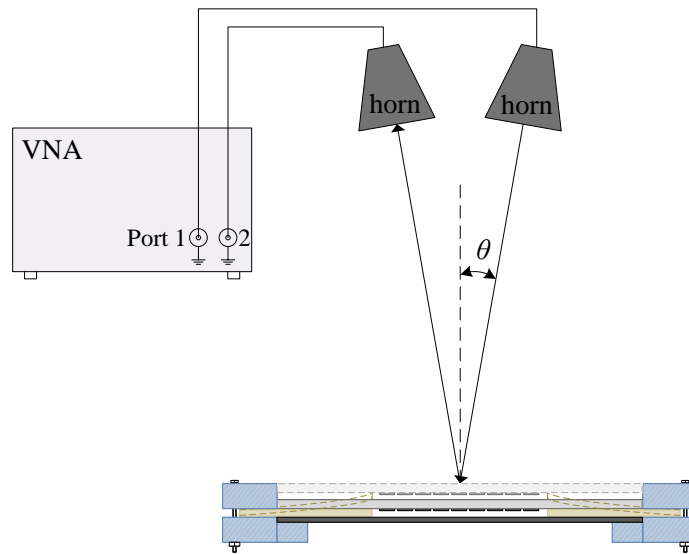
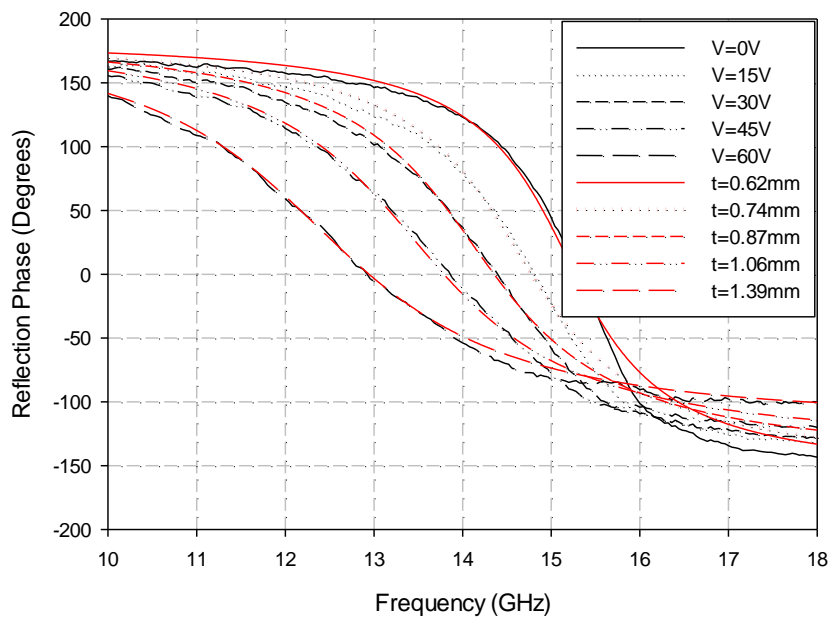Fig. 4.1.9.   Schematic representation of measurement set up.

Fig. 4.1.10.   Simulated and measured reflection phase of the proposed tunable HIS for different biasing voltages (V=0V – 60V).

4.2 TUNABLE DIPOLE ANTENNA WITH TUNABLE HIS GROUND PLANE

As an initial practical application of the proposed tunable HIS structures, a frequency tunable dipole antenna is presented. The antenna is placed above the proposed single resonant tunable HIS which acts as an active ground plane. Due to image theory, if a dipole antenna is placed at close proximity above a PEC surface, reverse image currents are produced which depending on the distance of the antenna from the PEC surface could result in cancelling out the radiation. On the other hand, if a PMC surface is placed below the antenna positive image currents are produced enhancing the radiation again depending on the distance (i.e. the phase shift between the dipole antenna and its image). The HIS acts as a PMC at a specific frequency and thus can reduce the profile of the structure and improve the matching. Tuning of the HIS response changes the antenna's impedance matching, obtaining a significant tuning of its operational frequency. A schematic diagram of the structure is shown in Fig. 4.2.1. The concept of employing a tunable HIS as a ground plane of an antenna has already been proposed for low frequency operation (~2.5GHz) where varactor diodes have been employed to tune the HIS response. These required a biasing network and also produced non-linearities, limiting the antenna's performance [8]. The aforementioned disadvantages are avoided with the configuration presented here.
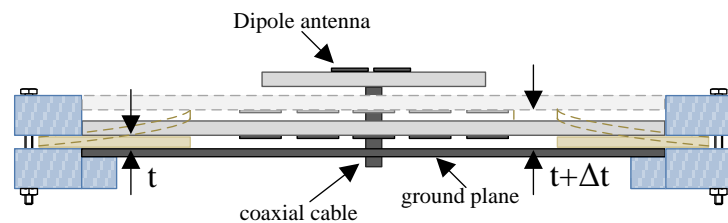

Fig. 4.2.1.   Schematic diagram of tunable dipole antenna with active HIS ground plane.

4.2.1 Design of Broadband Bow-tie Dipole Antenna

Initially, a broadband bow-tie dipole antenna has been designed, operating in the frequency range of interest, i.e. the tuning range of the HIS. The antenna is printed on a 0.8mm thick TLY-5 Taconic^{TM} dielectric substrate (ε_r=2.2, tanδ=0.0009) placed at distance 4.5mm above a ground plane, and is fed by a coaxial cable. A top view of the structure with all the dimensions of the antenna design is presented in Fig. 4.2.2. As can be observed from the figure, the feeding points have been chosen with a small offset in order to optimize the antenna's matching. The simulated S_{11} of the broadband antenna is depicted in Fig. 4.2.3, showing a good matching from 10.1GHz to 14.5GHz.
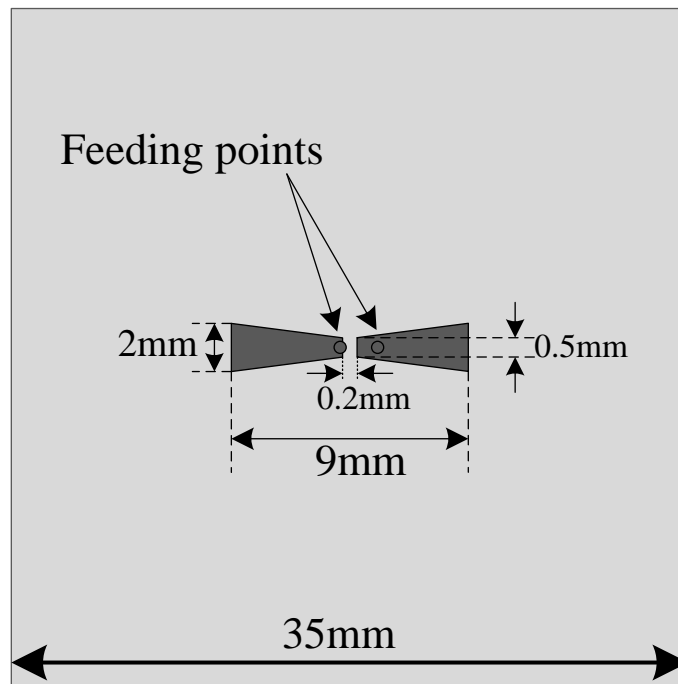

Fig. 4.2.2.   Top view of bow-tie dipole printed on dielectric substrate.
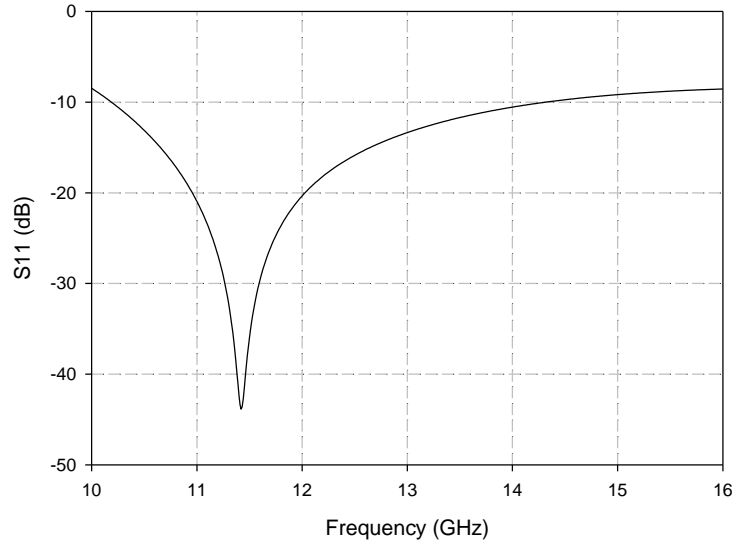
Fig. 4.2.3.   Simulated S_{11} response for the broadband bow-tie dipole antenna.

4.2.2 Tunability Evaluation of Dipole Antenna with Tunable HIS Ground Plane

Subsequently, the ground plane of the antenna presented in the previous section is replaced with the square loop element tunable HIS structure proposed in section 4.1.1, as shown in Fig. 4.2.1. A 5×5 array of metallic square loop elements placed at distance t above a ground plane has been employed in this configuration with the dimensions described in section 4.1.1 (p=6.5mm, d_l=5.57mm and d_a=3.34mm). The periodic array has been perforated in the middle of the central element, to allow the coaxial cable to pass through it. The initial HIS cavity distance is t=0.6mm and the distance between the ground plane and the substrate of the dipole antenna is S=2mm (Fig. 4.2.1). Hence, the profile of the structure is reduced with the introduction of the HIS. As the HIS cavity thickness changes due to the displacement produced from the actuators, the frequency of the AMC resonance is tuned. Consequently, the impedance matching of the dipole antenna is altered, resulting in a more narrowband response which is tuned along with the AMC resonance. This is evident from the simulated S_{11} shown in Fig. 4.2.4 for different HIS cavity thicknesses.
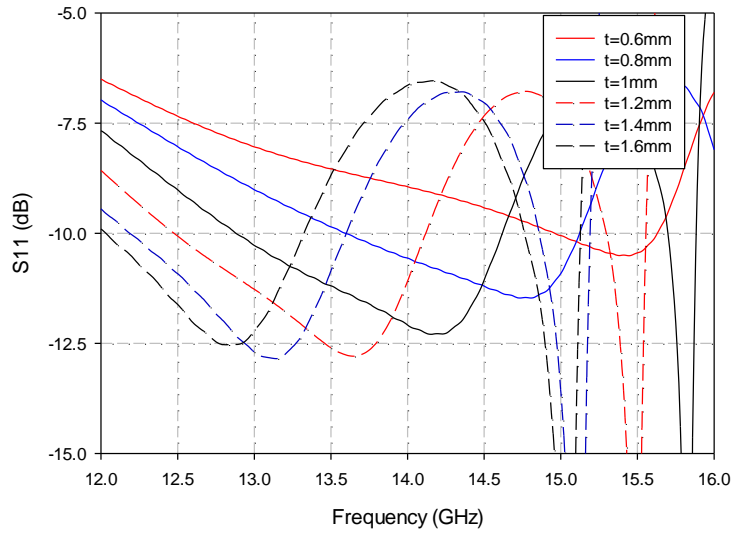
Fig. 4.2.4. Simulated S_{11} response of tunable bow-tie dipole antenna for different HIS cavity distances.

TABLE II
AMC AND DIPOLE ANTENNA OPERATING FREQUENCY FOR DIFFERENT HIS CAVITIES

t (mm)	f_{AMC} (GHz)	f_C (GHz)
0.6	15.44	15.3
0.8	14.63	14.4
1	13.86	13.75
1.2	13.15	13.3
1.4	12.51	12.9
1.6	11.92	12.6

A better comparison of the frequency of the AMC resonance and the central frequency of the antenna for each HIS cavity thickness is presented in Table II. It can be observed that there is good agreement between the frequency where the HIS reflection phase is zero (f_{AMC}) and the central operating frequency of the dipole antenna, especially for small cavity distances. Moreover, E- and H-plane radiation patterns are presented in Fig. 4.2.5 for different frequencies, corresponding to different HIS cavity thicknesses. An asymmetry is observed for the E-plane patterns, probably due to the offset of the dipole feeding. The simulated response

99

of the antenna validates the expected frequency reconfiguration of the dipole antenna with a tuning range of 19.4%.
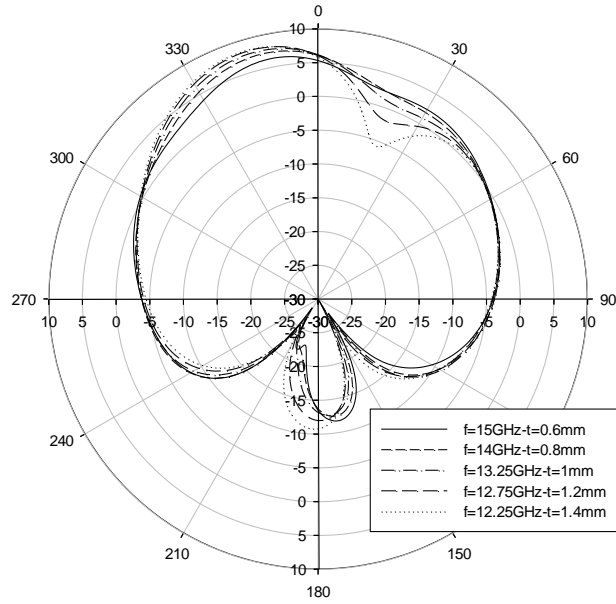
(a)
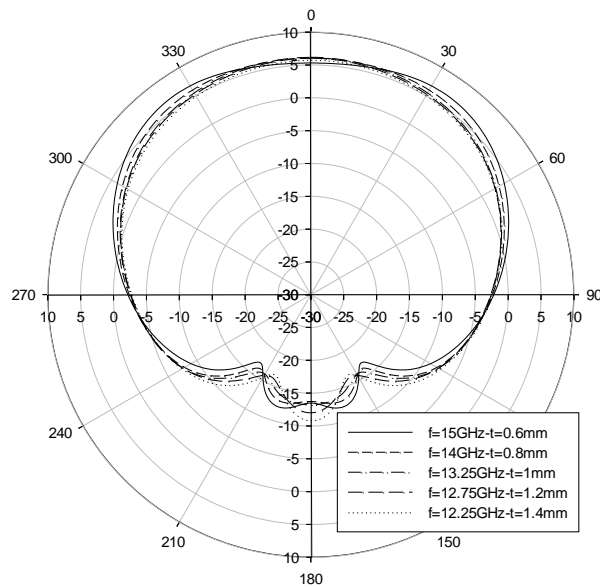
(b)

Fig. 4.2.5.   Simulated (a) E-plane and (b) H-plane radiation patterns for different frequencies corresponding to different HIS cavities.

4.3 CONCLUSIONS

In this Chapter, dynamically tunable low-loss High Impedance Surfaces based on piezoelectric bender actuators for operation at 15GHz and 30GHz have been demonstrated through simulation and experiments. Each of the proposed HIS structures, consists of an air cavity created between a periodic surface and a ground plane. Piezoelectric bender actuators are employed to support the periodic surface and produce a displacement between the surface and the ground plane. The displacement is produced by the actuators when they are under DC bias, and changes the cavity thickness resulting in a significant tuning of the reflection phase response. A significant advantage of the proposed structures is that since the actuators are not interfering with the radiation performance of the HIS array, the losses are very low.

Initially three different tunable HIS structures have been designed. Measurements for the first structure have been presented, giving a phase shift of 177.4^o at 14GHz. Finally, a tunable dipole antenna with an active HIS ground plane has been presented, as an application of the proposed structures. The proposed structures and tuning technique are directly scalable to higher mm-wave frequencies as is demonstrated in the next Chapter of this thesis, paving the way for a new class of low-loss tunable mm-wave metamaterial structures.

REFERENCES

[1] D. Sievenpiper, L. Zhang, R. F. J. Broas, N. G. Alexopolous, and E. Yablonovitch, "High-impedance electromagnetic surfaces with a forbidden frequency," *IEEE Trans. Microw. Theory Tech.*, vol. 47, no. 11, pp. 2059–2074, Nov. 1999.

[2] S. Wang, A.P. Feresidis, G. Goussetis, J.C. Vardaxoglou, "Low-Profile Resonant Cavity Antenna with Artificial Magnetic Conductor Ground Plane", *Electron. Lett.*, vol.40, no.7, pp.405-406, 1 April 2004.

[3] A. P. Feresidis, G. Goussetis, S. Wang, and J. C. Vardaxoglou, "Artificial magnetic conductor surfaces and their application to low profile high-gain planar antennas," *IEEE Trans. Antennas Propag.*, vol. 53, no. 1, pp. 209–215, Jan. 2005.

[4] J. Huang and J. A. Encinar, *Reflectarray antennas.* Hoboken, NJ: Wiley, 2008.

[5] E. Doumanis, G. Goussetis, J.-L. Gomez-Tornero, R. Cahill, and V. Fusco, "Anisotropic impedance surfaces for linear to circular polarization conversion," *IEEE Trans. Antennas Propag.*, vol. 60, no. 1, pp. 212–219, Jan. 2012.

[6] B. H. Fong, J. S. Colburn, J. J. Ottusch, J. L. Visher, and D. F. Sievenpiper, "Scalar and tensor holographic artificial impedance surfaces," *IEEE Trans. Antennas and Propag.*, vol. 58, no. 10, pp. 3212–3221, Oct. 2010.

[7] C. Mias and J. H. Yap, "A varactor-tunable high impedance surface with a resistive-lumped-element biasing grid," *IEEE Trans. Antennas Propag.*, vol. 55, no. 7, pp. 1955–1962, Jul. 2007.

[8] F. Costa, A. Monorchio, S. Talarico, and F. M. Valeri, "An active high impedance surface for low profile tunable and steerable antennas," *IEEE Antennas Wireless Propagat. Lett.*, vol. 7, pp. 676–680, 2008.

[9] R. Guzmán-Quirós, J.-L. Gómez-Tornero, A. R. Weily, and Y. J. Guo, "Electronically steerable 1D Fabry-Perot leaky-wave antenna employing a tunable high impedance surface," *IEEE Trans. Antennas Propag.*, vol. 60, no. 11, pp. 5046–5055, Nov. 2012.

[10]   www.physikinstrumente.co.uk

CHAPTER 5.

TUNABLE PERIODIC STRUCTURES FOR HIGHER MILLIMETRE-WAVE FREQUENCIES

Higher mm-wave and submm-wave frequencies present a significant challenge in terms of the development of tunable structures such as metasurfaces. Different tuning techniques compared to those employed in lower RF and microwave frequencies have to be employed. More specifically, for mm-wave frequencies, Micro-Electro-Mechanical Systems (MEMS) have been successfully employed in tunable HIS surfaces acting as reflectarrays [1, 2]. However, in order to obtain tuning, a MEMS component has to be integrated to each element of the periodic structure. This implies an upper frequency limit for the suitability of this technology, as the dimensions of the periodic elements decrease with the frequency, impeding the incorporation of an electrically large component in the unit cell of the array. In addition, tunable materials such as liquid crystals [3-5] at higher mm-wave and submm-wave frequencies have been investigated producing promising results. The main disadvantage of this tuning technique is that liquid crystals exhibit high losses and very low switching speeds.

In this Chapter, we propose a dynamically tunable low-loss phase shifting HIS at mm-wave frequencies based on electromechanical reconfiguration obtained by the use of a small number of piezoelectric actuators whose operation is described in Chapter 2. The actuators exhibit a displacement under a voltage bias which is translated to a dynamic control of the reflection phase. Similarly to the tunable HIS structures presented in Chapter 4, the proposed structure consists of a periodic surface placed above a ground plane at a distance t, creating an air cavity. Alternative designs are investigated using CST Microwave Studio^{TM} simulation software. In addition, experimental results are presented, demonstrating a dynamic impedance

surface performance with a phase shift of over 200° at about 60GHz.

As mentioned in Chapter 2, an important application of HIS surfaces is in Fabry-Perot type Leaky-Wave Antennas (LWA) which have been extensively investigated due to their high gain performance and simple fabrication [6-8]. They are directly scalable to mm-wave frequencies offering a viable solution for operation at this band. Moreover, they have attracted a lot of interest as they are very good candidates for beam-scanning applications due to their dispersive properties as explained in Chapter 2. Thus, static one-dimensional LWAs can achieve beam steering with frequency, if the antenna's source is placed towards the one end of the structure [9], with improved scanning performance when using an HIS as a ground plane [10]. Furthermore, since several applications require beam-scanning for a fixed frequency operation, various topologies have been proposed recently, for electronic reconfiguration of LWAs [11, 12]. Varactor diodes are employed in [11] to achieve scanning of a composite right/left handed leaky-wave antenna. In [12] an active HIS is used as ground plane. The HIS is loaded with varactor diodes that give a tunable reflection response, which in turn achieves scanning of the radiation beam for a fixed frequency. Nevertheless, the use of such tunable components imposes a limit for the operation frequency, as they suffer from high losses, non-linearities and parasitic capacitance at mm-wave frequencies.

In this Chapter, an application of the proposed tunable HIS structures in dynamically beam steered mm-wave Leaky-Wave Antennas (LWA) is presented. The structure consists of a periodic Partially Reflective Surface (PRS) and the proposed tunable HIS acting as an active ground plane. The significant change in the reflection phase of the HIS for a fixed frequency alters the resonant condition of the LWA and thus controls the pointing angle of the antenna's radiation beam for a fixed frequency.

5.1 DESIGN OF TUNABLE HIS FOR OPERATION AT 60GHz

The proposed structure is designed to operate around 60GHz and is presented in Fig. 5.1.1(a). It consists of a 2D periodic metallic array placed above a ground plane at a distance *t*, creating an air cavity. The unit cell of the proposed tunable HIS is depicted in Fig. 5.1.1(b, c). The structure is formed by the periodic surface and the ground and acts as a HIS reflecting the impinging waves with zero phase shift at a specific frequency and a wide range of reflection phases at other frequencies. In typical implementations of HIS structures, the substrate is grounded, creating a dielectric filled cavity between the array and the ground plane. Nevertheless, in the proposed configuration an air cavity is created giving an extra degree of freedom for controlling the HIS reflection phase response which is strongly related to the cavity thickness. Consequently, tuning of the reflection phase can be obtained by mechanically changing the distance between the ground plane and the periodic surface. For a dynamic tuning of the reflection phase, piezoelectric actuators are employed supporting the ground plane. Biasing the actuators induces their vertical expansion which is translated to a movement Δt of the ground plane (Fig. 5.1.1a). The cavity thickness is subsequently decreased, changing the reflection phase response of the structure. A plastic supporting base is used to hold in place the actuators, and the two surfaces. As will be discussed in section 5.2, the choice of plastic affects the performance of the prototype and a rigid material is used. It should be noted that the actuators are positioned below the ground thereby not interfering with the reflected radiation.
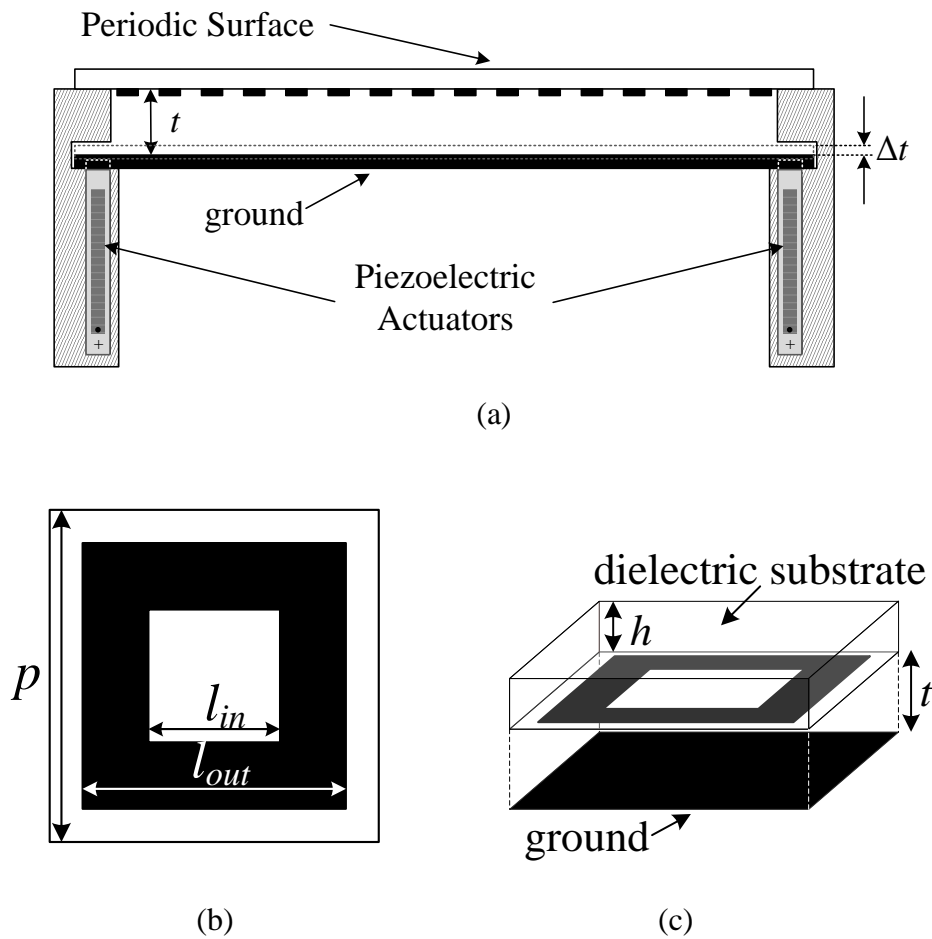
(a)

(b)

(c)

Fig. 5.1.1.   (a) Schematic of the proposed tunable HIS with the supporting base (dimensions not to scale), (b) unit cell of the proposed periodic surface (top view), (c) unit cell of the proposed HIS (perspective view).

5.1.1 Evaluation of Tuning Range

The maximum tunability of the presented concept depends largely on the maximum achievable displacement from the piezoelectric actuators. The piezo-actuators proposed for the design under investigation, are commercial stack multilayer actuators whose operation has been described in section 2.3.2.2. The particular model has a length of 18mm and can achieve a nominal maximum displacement of 18μm for an applied voltage of 120V (see section 5.2).

Based on the information of the actuators' displacement, the unit cell of the structure has been designed, choosing the geometry and dimensions so that a maximum phase shift could be obtained from the structure by changing the actuators' biasing voltage. Different geometries have been considered for the proposed configuration and a square loop metallic element has been chosen for the HIS array based on the fast variation of its reflection phase with the frequency. This characteristic is the key aspect of the design, in order to make it more sensitive to small variations of the cavity thickness and achieve a large phase shift. In Fig. 5.2.2, the reflection phase for a square loop element and a simple square patch with the same periodicity are shown for comparison. It is evident that the slope for the square patch has a smaller gradient, which results in a smaller phase shift for the same variation of the cavity thickness. This is in line with the variations of the reflection characteristics of free-standing Frequency Selective Surfaces (FSSs) [13].
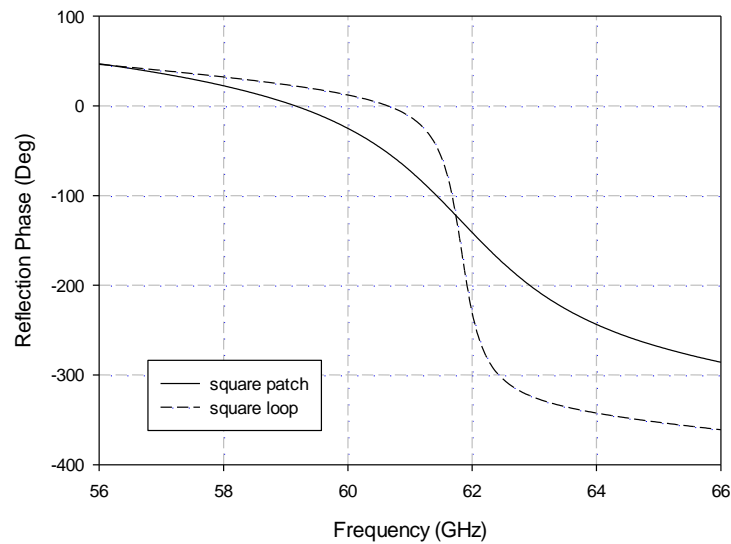

Fig. 5.1.2.   Reflection phase comparison for a square patch array and the proposed square loop design.

The elements of the array were printed on a dielectric substrate with ε_r=2.2, $tan\delta$=0.0009 and thickness h=0.8mm (Fig. 5.1.1c). In order to evaluate the tuning range of the structure,

two slightly different square loop geometries have been considered. The periodicity and the outer dimension of the square loop are p=1.75mm and l_{out}=1.5mm respectively for both cases while the inner dimension of the square loop l_{in} is 0.9mm in the first case and 1mm in the second (Fig. 5.1.1b). Moreover, two cases have been investigated for the cavity distance, one producing a first order cavity resonance and another producing a second order resonance in the frequency range of interest. Full wave analysis has been carried out in CST to extract the reflection characteristics of the proposed configurations for normal incident plane waves, applying periodic boundary conditions at the unit cell which assume an infinite structure.

5.1.1.1 *Sub-wavelength Cavity Distance*

Initially, the cavity distance between the ground plane and the periodic array is set at 70μm which corresponds to about λ/70 at 60GHz. The simulated phase and magnitude of the reflection coefficient for the case of l_{in}=0.9mm is shown in Fig. 5.1.3 for different cavity thicknesses. The magnitude of the reflection coefficient (Fig. 5.1.3a) shows that for t=70μm the AMC cavity resonance occurs at 56.7GHz, which is tuned towards higher frequency by reducing the cavity thickness. It should be noted that a minimum occurs at the frequency of the cavity resonance. However, the periodic surface design proposed here is based on closely spaced sub-wavelength (less than λ/3) square loop elements which yield low losses. The simulated phase of the reflection coefficient is shown in Fig. 5.1.3(b) for different cavity thicknesses which correspond to a displacement Δt from zero (t=70μm) to 20μm (t=50μm). It can be observed that a significant phase shift of $\Delta\varphi$=120.8^{o} at 57.4GHz for Δt=20μm (which is slightly more than the maximum displacement the actuators can produce) is obtained with this design.

Subsequently, the geometry with l_{in}=1mm is studied. The simulated phase and magnitude of the reflection coefficient for this case is shown in Fig. 5.1.4 for cavity thicknesses ranging

from 70μm to 50μm. For a displacement of Δt=15μm and Δt=20μm, a phase shift of 115° and

140° has been obtained respectively, for operation at 54.3GHz. Hence, compared to the

previous design, for the same displacement a larger phase shift is obtained but for a slightly

lower frequency. Furthermore, as can be seen from Fig. 5.1.4(a) the frequency of the AMC

resonance, is tuned from 53.5GHz to 55.2GHz for Δt =20μm. However, it should be pointed

out that in both designs the reflection phase at the inflection point (i.e. maximum slope) is not

0° as would be typically expected by an HIS surface, but ~ -150°. This is because of the

additional phase shift that the impinging waves undergo when travelling in the dielectric

substrate of the periodic surface, which can be easily calculated from the optical path length.

If the reference plane in the simulation had been chosen at the square loop array and not at the

top of the dielectric substrate, this additional phase would not be present.

So far, all the presented reflection coefficients correspond to normally incident plane

waves. However, in Fig. 5.1.4 the case of 30° incidence is also shown for t=50μm. It can be

observed that due to the sub-wavelength cavity the response is affected but not significantly

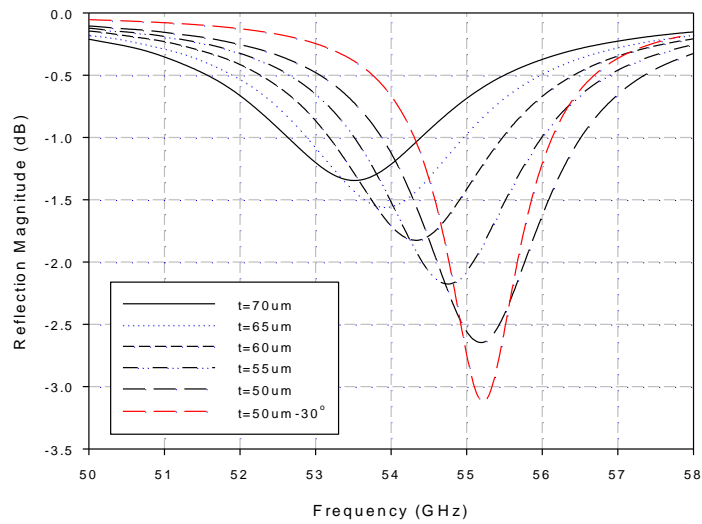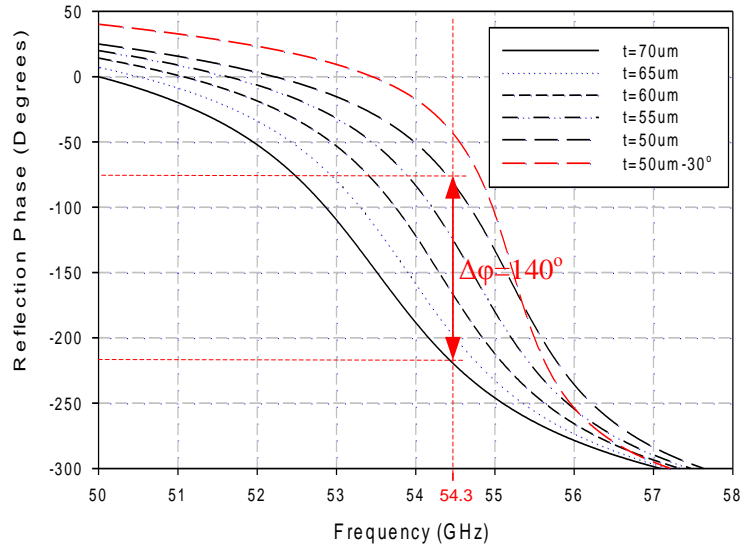compared to the half-wavelength case discussed later on.
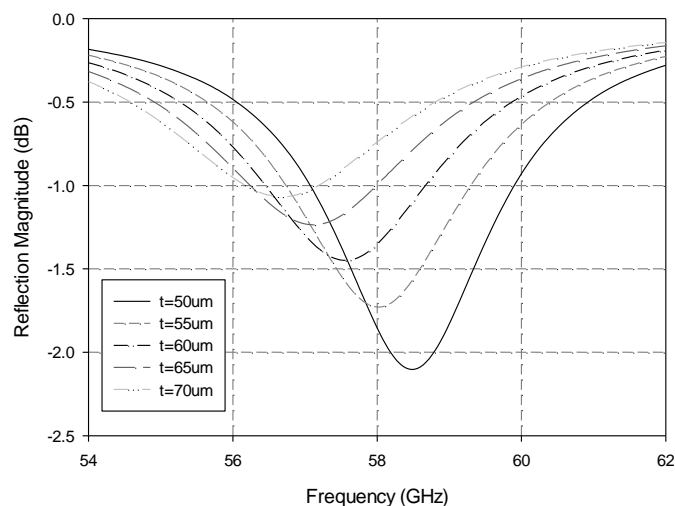
(a)
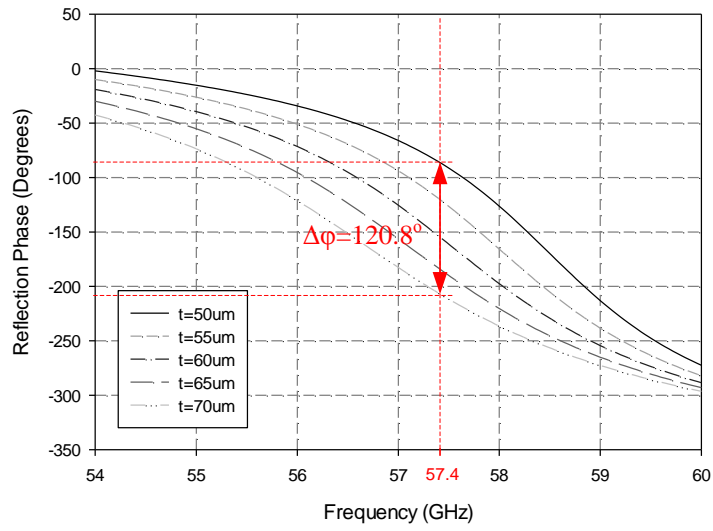
(b)

Fig. 5.1.3. Simulated reflection characteristics of the proposed periodic surface with l_{in}=0.9mm for different cavity thickness (50μm–70μm) (a) reflection magnitude, (b) reflection phase (for normal incidence).
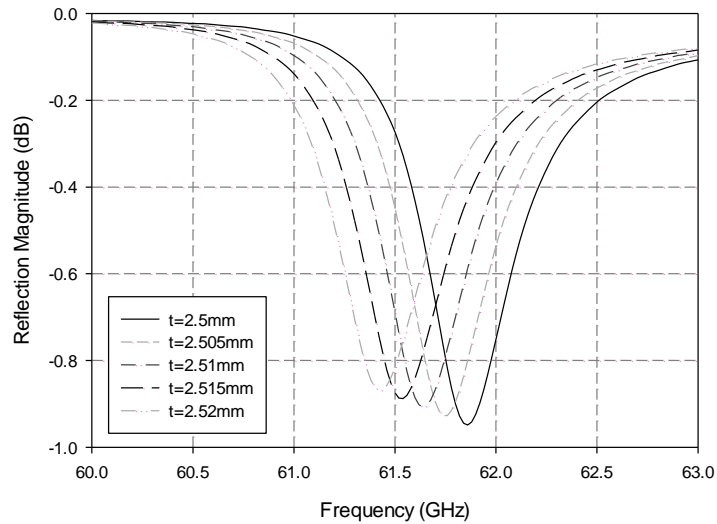

(a)

(b)

Fig. 5.1.4.   Simulated reflection characteristics of the proposed periodic surface with l_{in}=1mm for different cavity thickness (50μm–70μm) (a) reflection magnitude, (b) reflection phase (for normal incidence and for 30° incidence in the case of t=50μm).

5.1.1.2 *Half-wavelength Cavity Distance*

Although a significant phase shift has been obtained with the configurations that have been investigated in the previous subsection, the small height of the cavity leads to practical difficulties during the measurements since positioning and aligning the periodic surface at such a small distance from the ground plane proved to be non trivial for the first experiment as described in section 5.2. This led us to investigate a second set of designs where the HIS cavity has been increased to about λ/2. For the case of l_{in}=0.9mm the cavity thickness has been changed to t=2.52mm. For this thickness, a maximum slope of the reflection phase at about 62GHz is obtained. This is the second resonance of the cavity with that particular thickness while the first resonance occurs at about 10GHz. In the case of the new cavity, for a displacement of Δt=10μm and Δt=20μm, a phase shift of 90° and 126° has been obtained

111

respectively for operation at 61.8GHz which is approximately the frequency of the inflection point of the phase curves (Fig. 5.1.5b). Furthermore, from Fig. 5.1.5(a) it can be observed that the reflection magnitude is higher with the half-wavelength cavity, i.e. the losses are smaller, compared to the initial cavity thickness, which is a useful feature for our design. This is due to the lower currents induced on the elements of the periodic surface for increased cavity thickness, as has been observed in simulations.
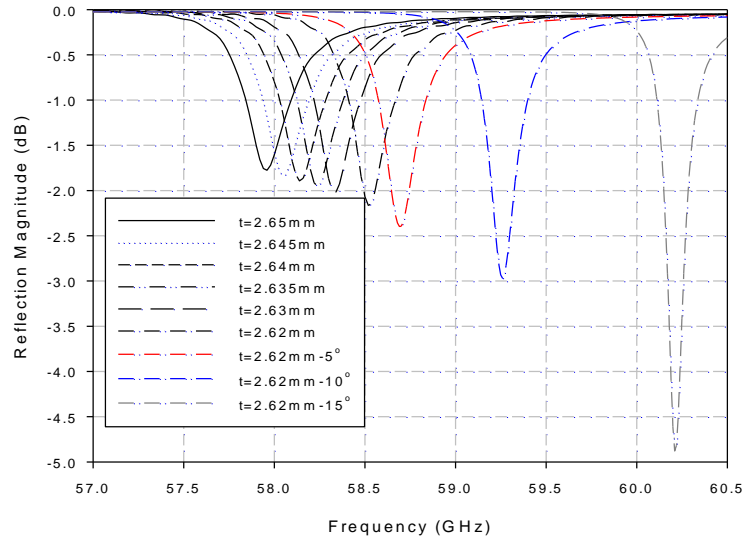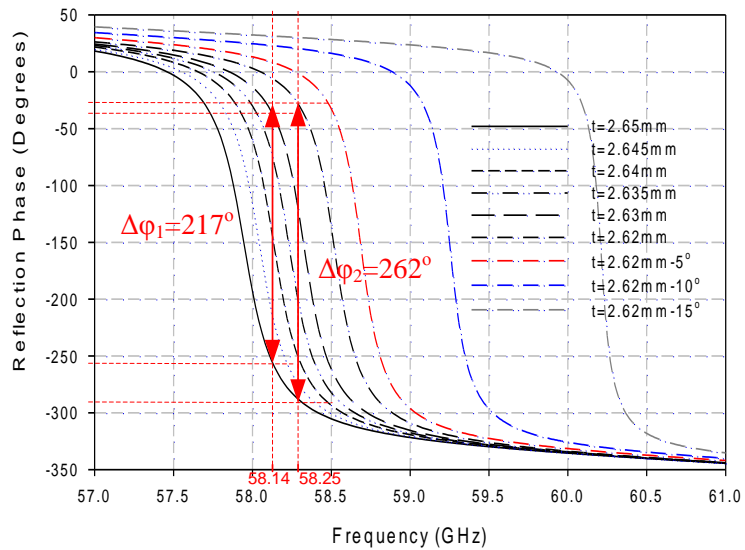

(a)
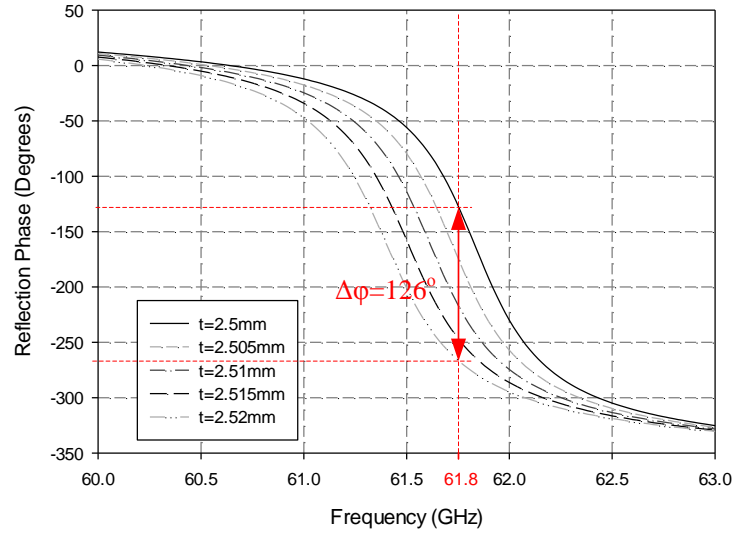
(b)

Fig. 5.1.5.   Simulated reflection characteristics of the proposed periodic surface with l_{in}=0.9mm for different cavity thickness (2.5mm–2.52mm) (a) reflection magnitude, (b) reflection phase (for normal incidence).

Similarly, for the design with l_{in}=1mm the HIS cavity has been increased to about $\lambda/2$, resulting in a second order resonance around 58GHz. The simulation results for different cavity thicknesses from t=2.65mm to t=2.62mm are presented in Fig. 5.1.6. Again, high reflectivity values, and hence low losses, slightly lower than the corresponding design of the previous subsection, are obtained with the proposed design (Fig. 5.1.6a). Moreover, as shown in Fig. 5.1.6(b), an even greater phase shift is achieved, compared to the design with sub-wavelength cavity, with a maximum of $\Delta\varphi_1$=217° at 58.14GHz for a displacement Δt=20μm, which is close to the maximum displacement the selected actuators can produce. From the same figure it can be observed that with the use of a different actuator, providing a displacement of Δt=30μm, a maximum phase shift of $\Delta\varphi_2$=262° can be obtained at 58.25GHz. It should be pointed out that significant more phase shift is obtained with this design than the one with l_{in}=0.9mm.

113

(a)

(b)

Fig. 5.1.6.   Simulated reflection characteristics of the proposed periodic surface with l_{in}=1mm for different cavity thickness (2.62mm–2.65mm) (a) reflection magnitude, (b) reflection phase (for normal incidence and for small angles of incidence for t=2.62mm).

In addition, comparing the two half-wavelength designs (with l_{in}=0.9mm and 1mm) it can be observed that there is a trade off between the maximum phase shift that can be achieved

and the bandwidth. More particularly, from Fig. 5.1.5(b) and Fig. 5.1.6(b) it can be seen that more phase shift leads to less bandwidth. However, if a more broadband performance is desired, the multi-resonant elements technique described is the Chapter 4 (section 4.1.3) can be applied.

Finally, the angular stability of the half-wavelength structure has been assessed for the design with l_{in}=1mm (Fig. 5.1.6). As expected, the increased cavity distance results in an angularly unstable structure, even for small angles of incidence from 5° to 15°.

5.1.2 Losses Evaluation

In this section an investigation is being carried out on the main factors contributing to the losses in the proposed configuration and on whether a more appropriate design could have been chosen instead, exhibiting less loss.

This study has been performed for the half-wavelength design with l_{in}=0.9mm. Initially, simulations have been carried out for the unit cell of the structure for three different cases. First, taking into account both dielectric and metal losses, then only dielectric losses with lossless metal and finally only metal losses with the dielectric considered lossless. The magnitude of the reflection coefficient for all three cases is depicted in Fig. 5.1.7. It can be observed that the minimum for lossy materials is −0.95dB while for lossy dielectric only and lossy metal only it is −0.07dB and −0.88dB respectively. This means the losses are mainly attributed to the metal with only a very small part related to the dielectric substrate.

Subsequently, another study has been carried out to evaluate the losses for two other possible configurations. The first case that has been considered comes from placing the periodic surface upside-down, so that the array is on top and the AMC cavity is formed partly from the dielectric substrate and partly from air as depicted in Fig. 5.1.8(b). In order to achieve a resonance at the same frequency the air cavity is now set at 1.382mm. In this case

the minimum of the reflection magnitude is −1.8dB as opposed to −0.95dB which corresponds to the original configuration. Furthermore, a dielectric filled cavity is also simulated with the cavity thickness now set at 1.694mm. The dielectric that has been employed is the same one used for the original configuration i.e. TLY-5 with dielectric constant ε_r=2.2 and $tan\delta$=0.0009. The minimum in this case is equal to −2.4dB. The reflection coefficient magnitude for all the aforementioned configurations is presented in Fig. 5.1.9. It is evident that the proposed design is greatly advantageous in terms of losses compared with the two other configurations.

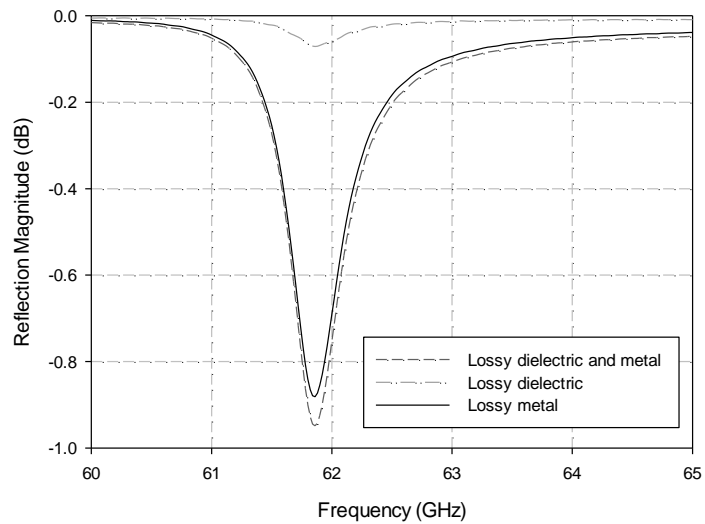Fig. 5.1.7.   Magnitude of the reflection coefficient for lossy and lossless materials.

(a)   (b)   (c)
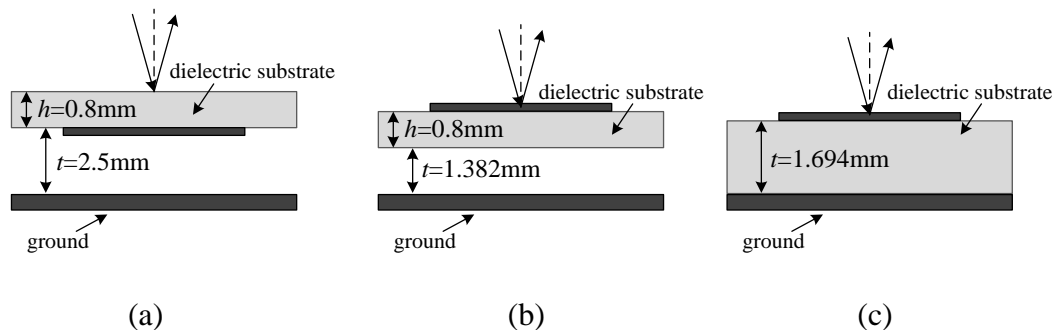
Fig. 5.1.8.   Unit cell of (a) original design, (b) design with air and dielectric and (c) design with dielectric filled cavity.
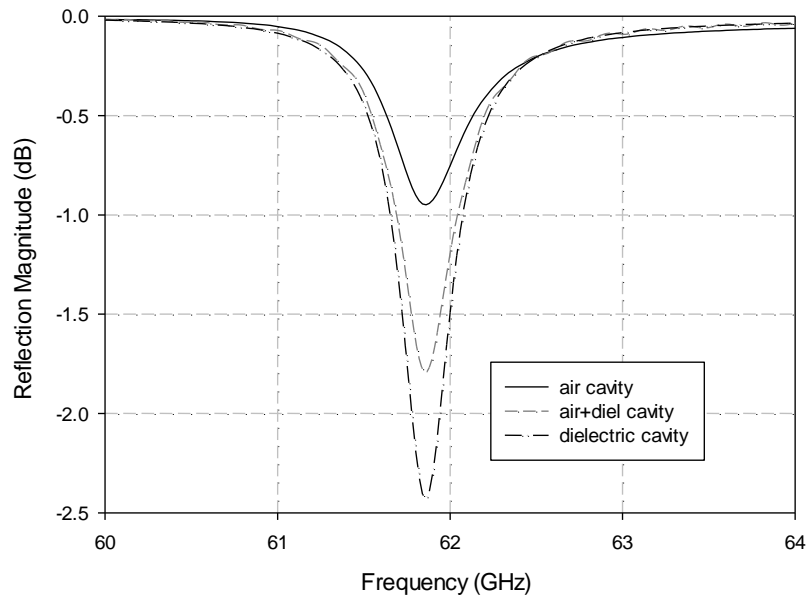
Fig. 5.1.9.   Magnitude of the reflection coefficient for the configurations of Fig. 5.1.8.

5.2 FABRICATION AND MEASUREMENTS

So far in this Chapter simulation results have been presented, demonstrating the concept of the proposed tunable HIS for higher mm-wave frequencies. In order to validate the simulation results, two prototypes have been fabricated and measured using piezoelectric actuators to provide the tuning of the proposed HIS. The actuators that have been employed for these high frequency configurations are the P-885.51 commercial stack multilayer actuators from Physik Intrumente (PI). The particular model has a length of 18mm and can achieve a nominal maximum displacement of 18μm for an applied voltage of 120V [14] as mentioned in section 5.1.1. The photograph in Fig. 2.3.5(b) shows one of the actuators without the wires used to apply the DC voltage, which are carefully soldered to one of the small metallic bits visible in the picture. The "+" sign indicates the positive polarization. The measurement results are presented in this section. Moreover, some of the problems that have been encountered are discussed as well as possible ways to address them.

117

5.2.1 Initial Measurements

Initially, a prototype of the proposed design with l_{in}=0.9mm and half-wavelength cavity has been fabricated and measured. A 23×23 (8λ×8λ) square loop element array printed on a 60×60mm^2 TLY-5 dielectric substrate has been fabricated as shown in Fig. 5.2.1(a). In order to support the actuators and the ground plane a plastic base has been made. The plastic that has been used was nylon, which was proven to be unsuitable for the experiment as explained later on. It was designed so that two actuators would exactly fit on each side of a plane surface where the ground plane (40×60mm^2) is mounted. The starting position of the actuators is adjustable with screws to achieve the desired cavity thickness which in this case is 2.5mm. Finally, the periodic surface has been secured on top of the two actuators. A photograph of the complete structure is shown in Fig. 5.2.1(b).
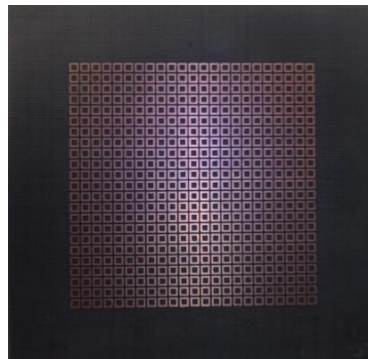
(a)

(b)

Fig. 5.2.1.   Photograph of (a) fabricated 23×23 element array and (b) of the complete structure.

Before starting the measurement, a characterization of the two actuators has been carried out to validate their expansion properties and also to test the operation of the biasing and their integration in the plastic base used for supporting the structure. An optical interferometer has been used in order to measure the displacement which is in the order of micrometers. The displacement of both actuators for voltages from 0 to 120V has been measured and the results are presented in Table I. As it can be observed from the table, each actuator achieved different displacement for the same applied voltage. For voltage values up to 20V no measurable displacement occurred while the maximum ΔL was 14.3μm and 10.5μm for actuators 1 and 2 respectively. Although a slight difference was expected between them, the fact that actuator 2 achieved less displacement, is attributed to the way the negative electrode has been soldered on it. As can be seen from Fig. 5.2.1(b), there is excessive soldering on the left actuator (actuator 2) that may prevent the proper expansion of the ceramic disk that lies in the specific position. Furthermore, due to possible deformation of the plastic base not even actuator 1 has reached the nominal maximum ΔL (18μm).

TABLE I
PIEZO-ACTUATORS DISPLACEMENT MEASUREMENT FOR DC VOLTAGES FROM 30 TO 120V

DC Voltage (V)	Actuator 1 ΔL (μm)	Actuator 2 ΔL (μm)
30	1.6	0.7
40	3.5	0.9
50	4.5	1.4
60	6	2.9
70	7.4	3.7
80	8.5	4.1
90	10.8	5.5
100	11.8	8.5
110	12.9	9.1
120	14.3	10.5

Once the structure was complete, two standard gain V-band horn antennas were employed in order to measure the magnitude and phase of the reflection coefficient from the periodic surface. Both antennas were fed from a Vector Network Analyzer (VNA). One was connected to channel 1 and served as the transmitter and the other was connected to channel 2 and served as the receiver. Before starting the measurement, a full two-port calibration of the VNA was carried out for the frequency range of interest. The horns were positioned aiming towards the periodic surface at a distance of more than 20cm away from it and at an angle of incidence/reflection of about 15°. A schematic representation of the measurement set up is shown in Fig. 5.2.2. The reflection has been measured through the S_{21} between the two horn antennas for different applied voltage at the actuators.
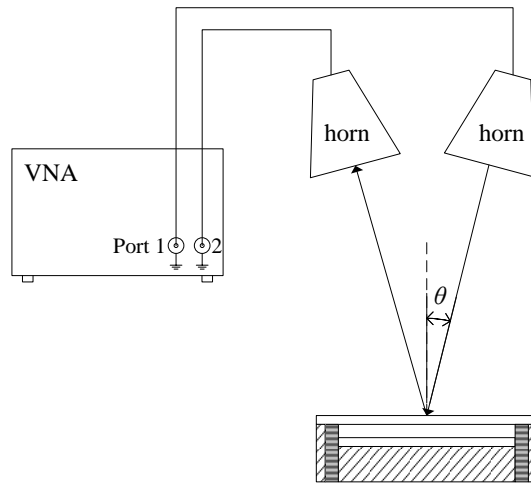

Fig. 5.2.2.   Schematic representation of measurement set up.

The phase response for voltages 0V, 60V and 120V is presented in Fig. 5.2.3 after being normalized with respect to a measurement of a flat metallic surface placed in the same position as the array. It can be seen that a phase shift of about 30° is obtained at about 58.2 GHz when 120V are applied to the piezo-actuators with respect to the unbiased state. It should be pointed out that with the particular mounting of the structure, the cavity distance is

increased when the voltage is applied to the actuators, since they support the periodic surface and not the ground plane as assumed in the simulations.

Although the concept of the design, which was to obtain a dynamic phase shifting surface, has been validated, there is a disagreement with the simulation results. In particular, the obtained phase shift is significantly less than what was expected from the periodic simulations. Even considering a maximum displacement $\Delta t=10\mu$m, which is a valid assumption from Table I, the achieved phase shift was expected to be 90°. The disagreement can be attributed to two major factors. First, the most important factor for this discrepancy is the finite size of the measured periodic surface. Indeed, we have carried out a full wave simulation of a finite size structure in CST (Fig. 5.2.4), and it was found that the phase shift for $\Delta t=10\mu$m is about 60° which is closer to the measured one than the infinite size simulation result. The finite structure simulation also produced the sharp peak that appears in the measurements just above the cavity resonance (over 58.3GHz). Inspection of the electric field inside the cavity showed that this effect is due to a resonance across the lateral dimensions of the finite array which distorts the field distribution in this direction. Second, the disagreement can also be attributed to the imperfect flatness of the two surfaces and the approximate alignment between them which is particularly crucial at mm-wave frequencies and should ideally be performed using quasi-optical techniques. Finally, the measured frequency of the cavity resonance (where the slope in the phase is maximum) is 58.2GHz while the simulated one is 61.8GHz. This is because the actual cavity thickness was slightly more than 2.5mm which resulted in a resonance at a lower frequency. This has been taken into account at the simulation of the finite size array where, as can be seen from Fig. 5.2.4, the cavity thickness is varied between 2.68mm and 2.69mm ($\Delta t=10\mu$m) and the cavity resonance occurs at the same frequency as the measurement.
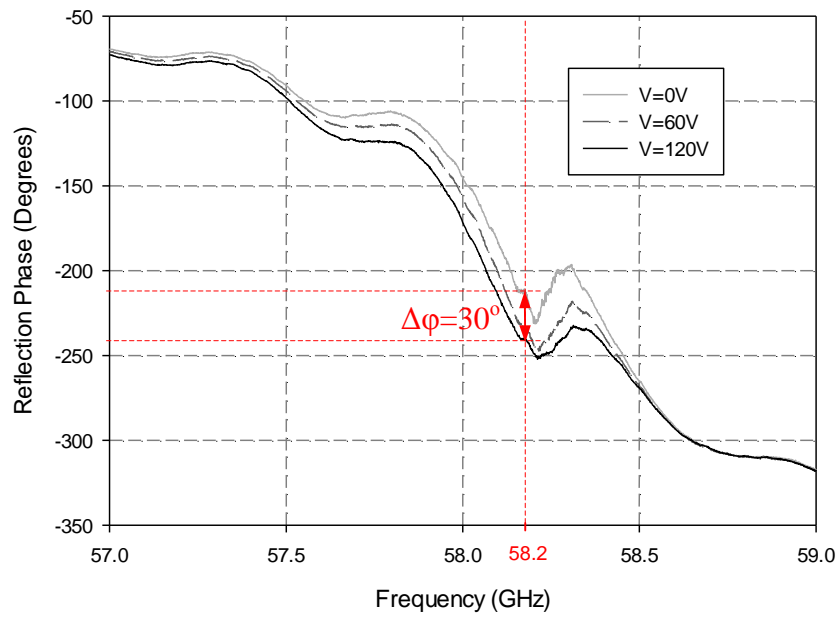
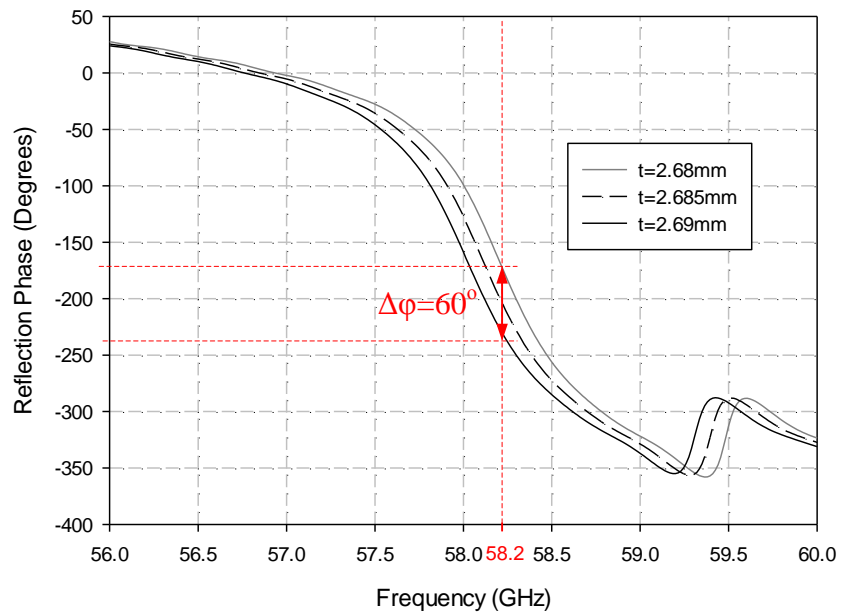Fig. 5.2.3.   Measured reflection phase of the fabricated prototype for three different voltages.

Fig. 5.2.4.   Simulated reflection phase for finite size structure.

5.2.2 Improved Measurements

Subsequently, a prototype of the proposed structure with l_{in}=1mm has been fabricated and measured. According to the investigation carried out in section 5.1.1, this design is expected to give more phase shift compared to the alternative one with l_{in}=0.9mm. The configuration that has been selected is the one with half-wavelength distance again, since it has proven in practise to be significantly easier to position the periodic array at $\lambda/2$ distance from the ground plane, rather than $\lambda/70$. Moreover, this design is more sensitive to changes of the cavity thickness, thus producing more phase shift.

From the initial measurements presented in the previous section, it has been concluded that a larger size array is necessary in order to obtain results that are closer to those corresponding to the infinite array considered in the simulations. Thus, the periodic array that has been used for this measurement (Fig. 5.2.5a) consists of an array of 46×46 copper square loop elements printed on a 0.8mm thick, TLY-5 Taconic^{TM} substrate with overall dimensions 100mm×100mm (~20λ×20λ). Moreover, a different, more rigid material has been used, and a completely different supporting base has been designed and fabricated. The structure is made of plastic acetal copolymer (POM) material and has been designed in order to support all the individual components of the proposed structure as shown in Fig. 5.2.5(b). The periodic surface has been positioned on the supporting base, on top of the ground plane which in turn is supported by four new piezoelectric actuators (Fig 5.2.5b). The actuators have been placed in specially designed openings within the four vertical posts of the base, which also include the necessary gaps to provide access for the electrodes connected to the actuators.

The same two horn antennas as before have been used for the measurement of the reflection characteristics. The measured reflection phase for different actuation states (V=0V– 120V) is presented in Fig. 5.2.6(a), normalized with respect to a measurement of just a planar

metallic surface placed at the same position as the array. In this configuration, the cavity thickness decreases with the voltage, because the actuators support the ground plane. A maximum phase shift of 200.55^o is obtained at about 58.14GHz, validating the simulated performance of the proposed design. The measured reflectivity and reflection phase versus the DC voltage are depicted in Fig. 5.2.6(b) for the frequency of the maximum phase shift. It can be observed from the graph that the phase changes almost linearly with the applied voltage. However, the reflectivity is lower than expected from the simulation results. This is studied and explained in detail in section 5.2.3.

Finally, a comparison between full wave simulation results and measurements is carried out in Fig. 5.2.6(c) for V=0V and V=120V, corresponding to cavity thicknesses t=2.648mm and t=2.63mm respectively, i.e. to a displacement Δt=18μm. The maximum phase shift obtained from the simulation results for the specific displacement is 208.57^o at 58.16GHz. . It is evident that there is good agreement between the measured and simulated results. The small discrepancies and fluctuations observed in the measurements are due to the fact that the dielectric substrate used for the periodic surface is not perfectly flat and therefore it was not exactly parallel with respect to the ground during the experiment.
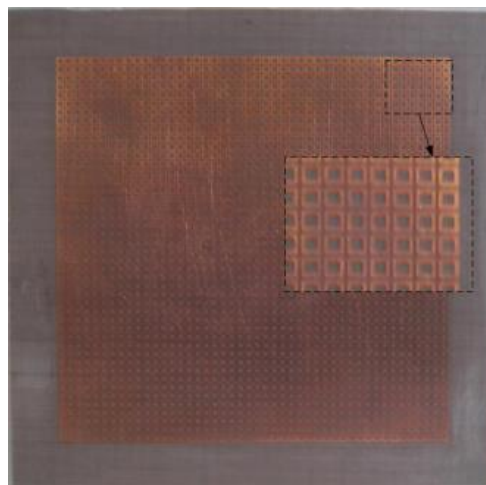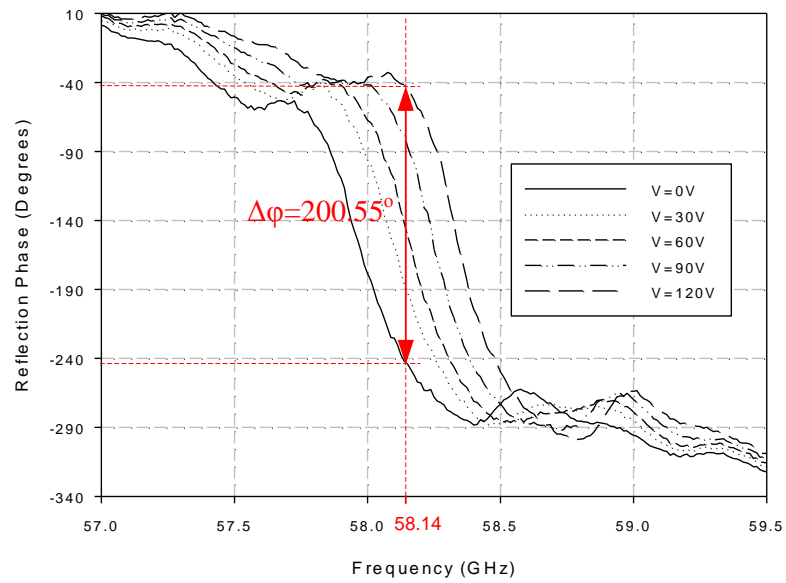

(a)
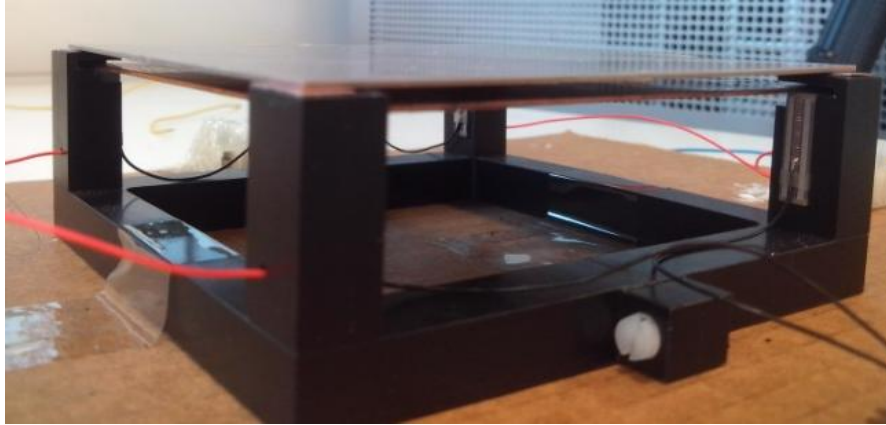
(b)

Fig. 5.2.5.   Photograph of (a) the fabricated periodic surface and (b) the complete structure with the supporting base and the actuators.

(a)
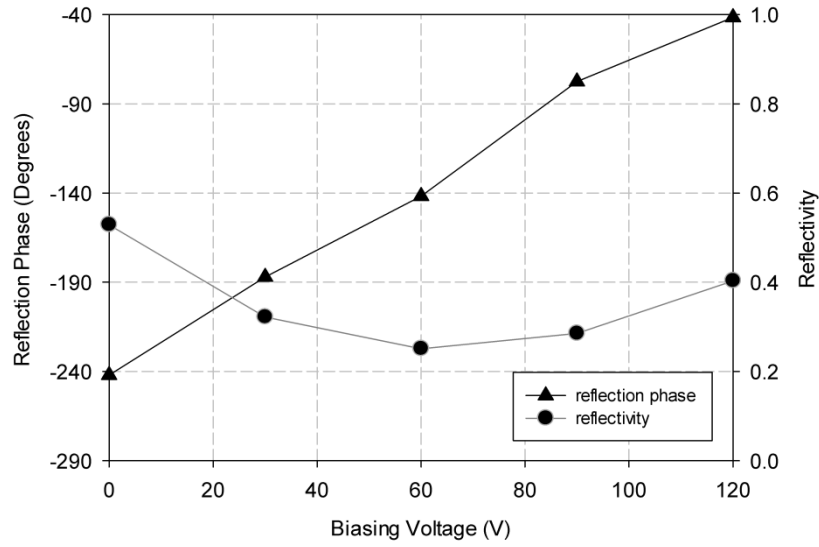
(b)
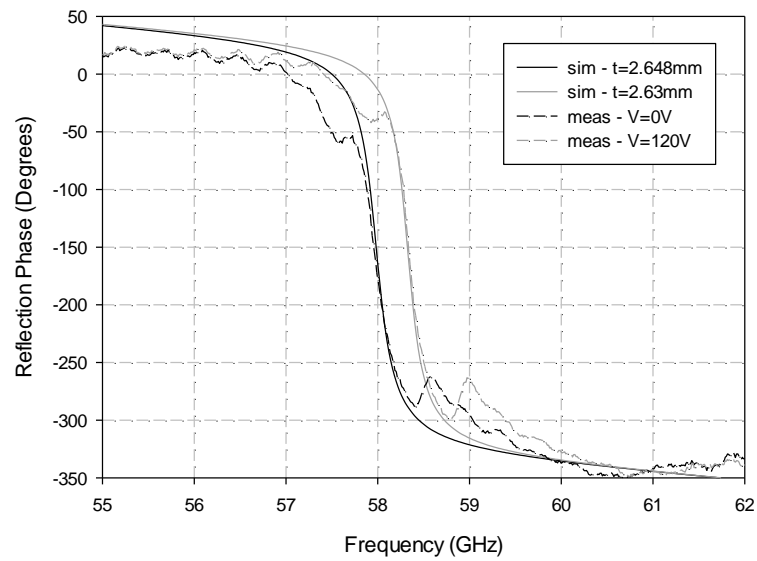
(c)

Fig. 5.2.6.   (a) Measured reflection phase versus frequency for different voltages, (b) Measured reflectivity and reflection phase at the frequency of the maximum phase shift for different voltages and (c) Comparison of simulated and measured reflection phase for V=0V and V=120V.

5.2.3 Effect of Copper Conductivity

Although the improved measurement results presented in the previous section have validated the proposed concept in terms of the achieved phase shift, it can be observed that the measured reflectivity is lower than that expected from simulations. This is attributed mostly to the reduced conductivity of the printed copper elements on the specific substrate experienced at these frequencies.

The reduction of the conductivity occurs because of the roughness of the copper surface. Due to the resonant nature of the proposed structure and the strong currents induced on the elements, the ohmic losses are significantly increased with decreased copper conductivity. Indeed, simulations have been carried out for reduced copper conductivity and for t=2.64mm, presented in Fig. 5.2.7. The simulations show that while a 100% conductivity (5.96×10^7 S/m) gives a reflectivity of 0.81, a 20% conductivity (1.192×10^7 S/m) results in a reflectivity of 0.57, and a 5% of copper conductivity (0.298×10^7 S/m) gives a reflectivity of 0.35 which is in agreement with the measurement results.

The effect of the copper conductivity was further investigated by fabricating and measuring other structures operating at 60GHz, such as a static HIS with the array printed directly on a metal backed substrate of similar type. This was performed to eliminate the possibility of any losses caused by the slight misalignment of the two surfaces (periodic array and ground plane) which could be present in the proposed tunable configuration. The reflection magnitude and phase for the static structure are shown in Fig. 5.2.8. Matching of the simulation and measured results in this case, for a design with a resonance at about the same frequency as the tunable HIS and a slope of the reflection phase comparable to the one obtained from the proposed configuration, have resulted in a copper conductivity of 0.2384×10^7 S/m which is 4% of the ideal value (Fig. 5.2.8a).

However, according to literature on the subject, 4% of the ideal copper conductivity is not reasonable. Typically with a surface roughness of about 5μm, 25% of the ideal value is expected [15]. If the roughness is further increased the value of the conductivity is not affected. This reduced conductivity of 1.49×10^7 S/m (25% of the ideal value) results in 4dBs of losses in our structure. Hence, the rest of the losses can be attributed the thickness variation of the substrate which causes energy loss due to reflection in other directions. The variation of thickness in the two measured prototypes (tunable and static) was ~6%. Nevertheless, this problem could be eliminated by using better quality materials such as optically flat quartz substrate and fabrication processes appropriate for high mm-wave and submm-wave frequencies [4, 5].
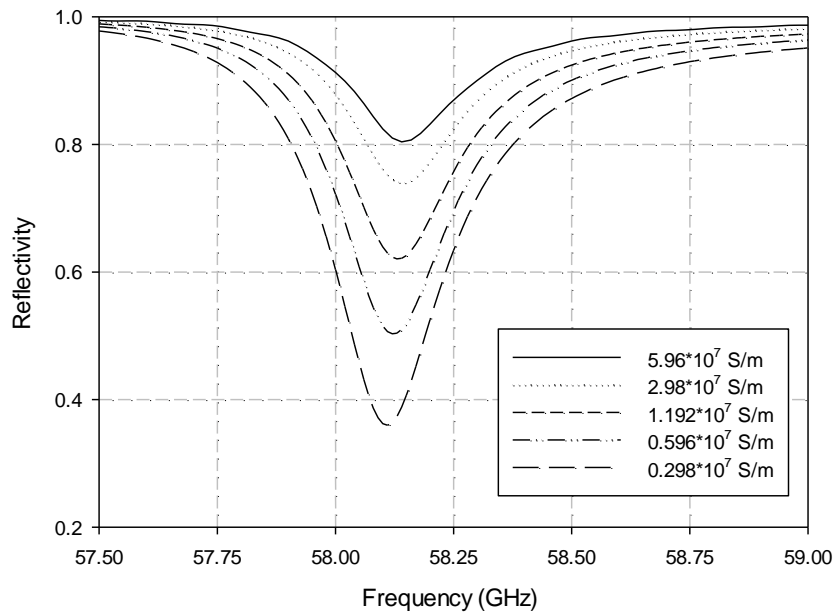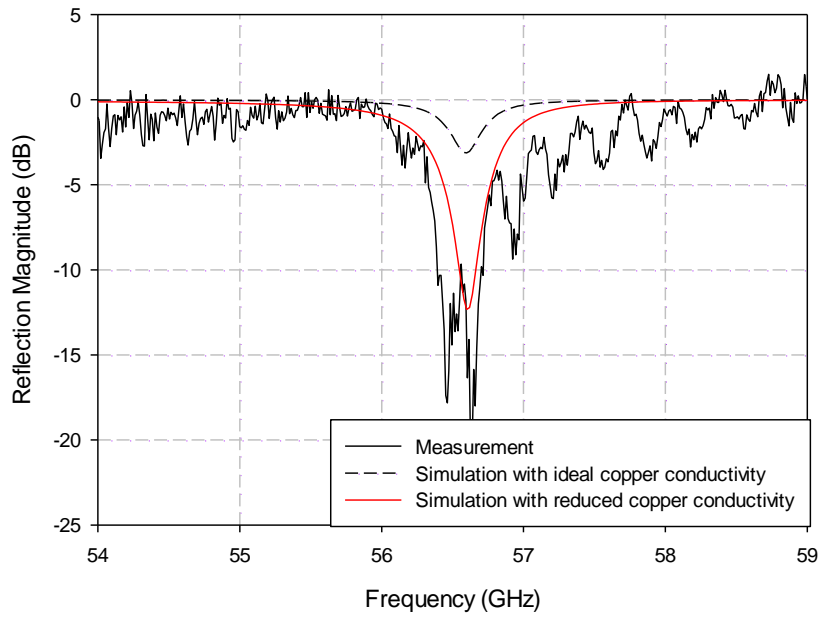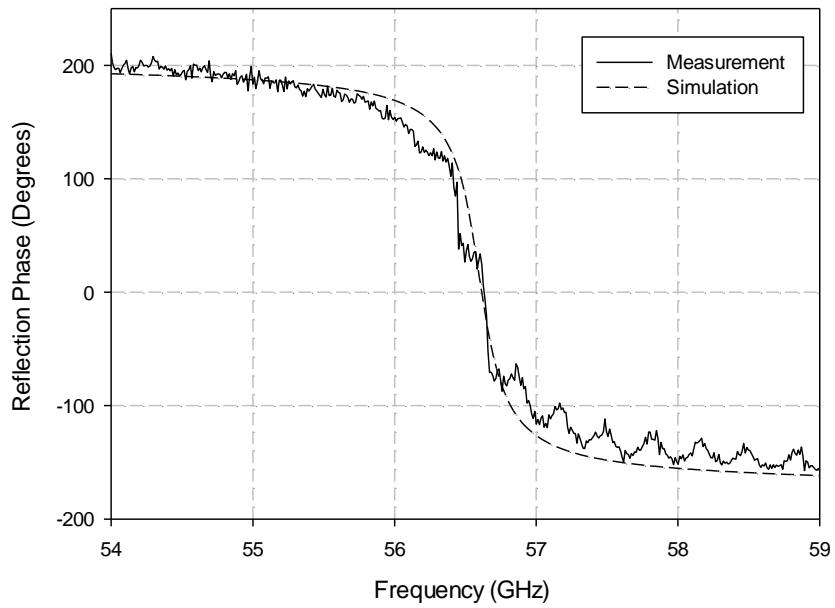

Fig. 5.2.7.   Reflectivity for t=2.64mm for different copper conductivity values.

(a)

(b)

Fig. 5.2.8.   Comparison of simulated and measured reflection (a) magnitude and (b) phase

for static HIS structure.

5.2.4 Alternative Design with Quartz Substrate for Improved Losses Performance

As mentioned in the previous section, the reduced copper conductivity in the proposed HIS has a very significant effect in the exhibited losses of the structure. It also stated that this can be avoided with the appropriate choice of material and fabrication process. Thus, an alternative tunable HIS is proposed in this section, with the periodic array printed on a quartz substrate for an improved losses performance. The unit cell of the structure is as illustrated in Fig. 5.1.1(b, c). However, the dimensions have been modified, compared to the designs presented in section 5.1.1 in order to obtain an HIS response in the desired frequency, since a different substrate is now utilized. Namely, the thickness of the substrate is h=550μm (which is a typical quartz wafer thickness [5]) with ε_r=3.78 and $tan\delta$=0.002. The rest of the dimensions are p=1.35mm, l_{out}=1.15mm and l_{in}=0.79mm. The cavity thickness t is varied from 2.62mm to 2.6mm. The simulated reflection coefficients of the structure are shown in Fig. 5.2.9. It can be observed that the AMC resonance occurs around 58.5GHz and 59GHz and the maximum losses are 1.3dB (Fig. 5.2.9a). Moreover, a phase shift of 203.5^o is obtained for Δt=20μm at 58.76GHz (Fig. 5.2.9b) which is similar to the one obtained from the original design with l_{in}=1mm and λ/2 cavity.
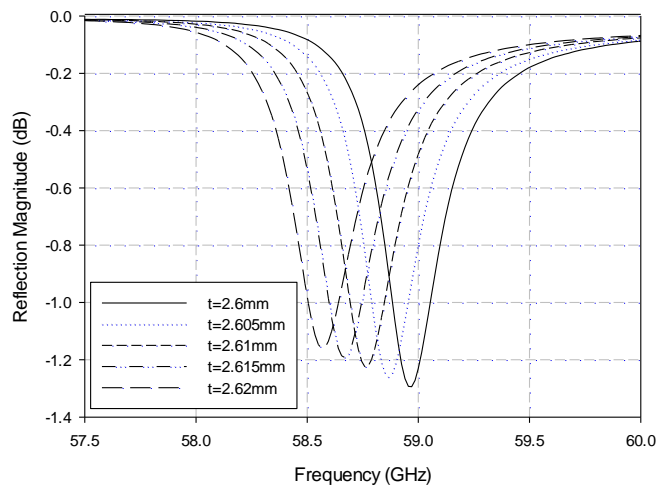
(a)
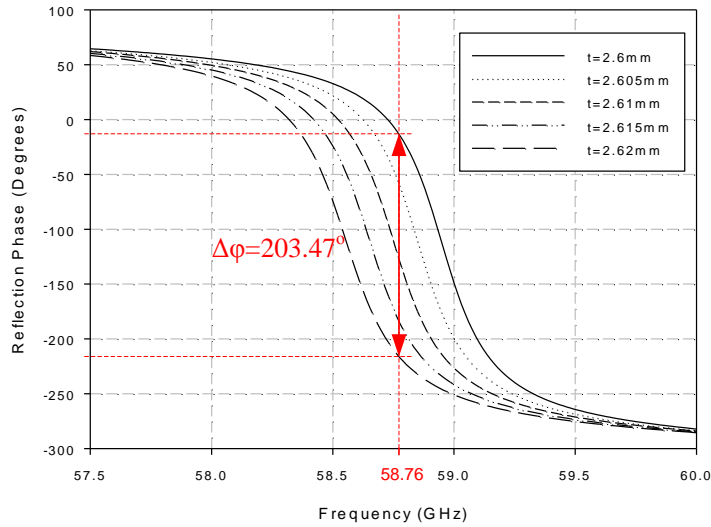
(b)

Fig. 5.2.9.   Simulated reflection (a) magnitude and (b) phase of alternative HIS with quartz substrate for different cavity thicknesses.

5.3 BEAM-SCANNING LEAKY WAVE ANTENNA BASED ON TUNABLE HIS GROUND PLANE

As an application of the proposed tunable HIS structures, a beam-scanning Leaky Wave Antenna (LWA) is designed in this section. LWA have the property to exhibit steering of the direction of the main beam with frequency as explained in Chapter 2. However, a beam-scanning for a fixed frequency is obtained with the proposed configuration. The tunable HIS structure described in section 5.1.1 with l_{in}=1mm is employed in this section as a ground plane in a 1D hollow LWA (Fig. 5.3.1a). The specific HIS design was selected due to its low profile and large tuning range of its reflection phase. A PRS formed by an array of square metallic elements printed on a TLY-5 substrate, is placed on top of the HIS at a distance t_1=1.5mm as depicted in Fig. 5.3.1(a, b) creating a resonant cavity type LWA. The excitation of the antenna cavity is achieved by an ideal dipole placed on one side of the cavity, with a vertical metallic ground closing that side also shown in Fig. 5.3.1. The HIS thickness t is

131

initially 50μm (corresponding to V=120V) and is then gradually increased to 70μm. The total antenna profile is about λ/2. The operation of the antenna can be described employing the ray optics approach explained in [6-8] and is based on satisfying a resonance condition in order to obtain constructive interference and thus high directivity performance. The HIS acts as a tunable ground plane that introduces the required phase shift which in turn alters the resonant condition of the cavity and thus controls the pointing angle of the antenna's radiation beam for a fixed frequency. The unit cell of the PRS is shown in Fig. 5.3.1(c). Its periodicity is equal to the periodicity of the HIS array (p=1.75mm) while the size of the patch is d=1.5mm. The dimensions of the PRS have been chosen so that high reflection magnitude values are obtained from the surface which leads to high directivity as explained in [7].

(a)

PRS array

metallic
wall

dipole

AMC array

p

d

h

t_1

h

t

ground

(b)

(c)
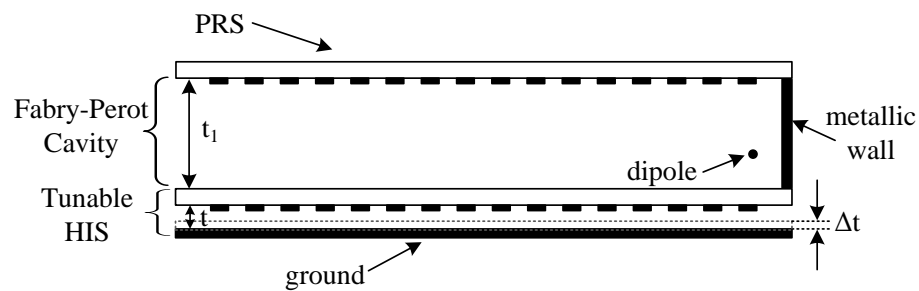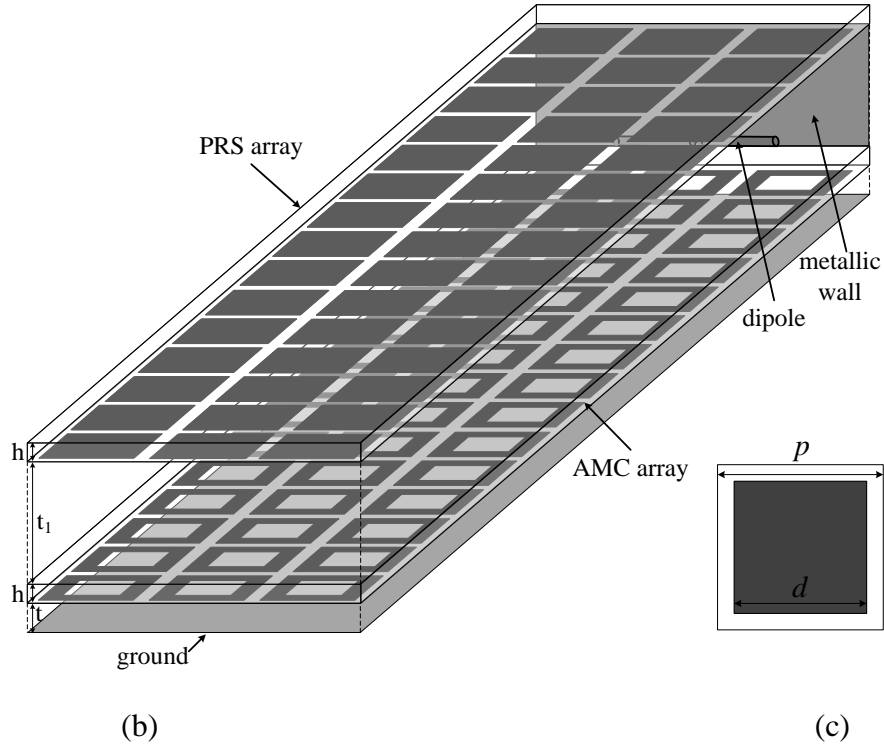
Fig. 5.3.1.   (a) Cross section and (b) perspective view of the proposed LWA with the
tunable ground plane (dimensions are not to scale), (c) Unit cell of the PRS array.

5.3.1 Analysis of Beam Scanning Range

A simple approximate plane wave analysis assuming infinite size arrays can be employed
to provide initial guidelines of the antenna beam scanning range that can be achieved using
the tunable HIS developed in the previous section. Equation (5.3-1) developed in [6, 8] is
used, describing the power pattern of the LWA and considering a tunable reflection phase φ
of the ground:

$$P = \frac{1 - R^2}{1 + R^2 - 2R\cos(\varphi_{PRS} + \varphi - \frac{4\pi}{\lambda} \cdot t_1 \cdot \cos\theta)} F(\theta) \qquad (5.3\text{-}1)$$

where R is the reflection magnitude of the PRS array, φ_{PRS} the reflection phase of the PRS, θ
the angle of incidence on the PRS and $F(\theta)$ the radiation pattern of the primary feed of the

resonant cavity. The excitation of the antenna cavity in our study is achieved by an ideal dipole placed on one side of the cavity, with a vertical metallic ground closing that side, resulting in a uni-directional LWA (Fig. 5.3.1a, b). This is expressed in (5.3-1) by the term F(θ) which is the radiation pattern of a dipole over a ground plane given from (5.3-2):

$$F(\theta) = \cos\left(\theta + \frac{\pi}{2}\right)\cos\left(\frac{1}{2}k \cdot s \cos\left(\theta + \frac{\pi}{2}\right) + \pi\right) \qquad (5.3\text{-}2)$$

where s the distance between the dipole and the metallic wall and k the wave number. The beam angles obtained from this analytical approach for different displacement Δt, which corresponds to different reflection phase values of the HIS ground, are shown in Fig. 5.3.2 for a fixed frequency, f=54.6GHz. It is evident from this theoretical analysis assuming an infinite size structure, that the beam scanning range $\Delta\theta$ is 58$^{\text{o}}$ for Δt=20μm with θ the angle of the main beam. This displacement corresponds to a phase shift $\Delta\varphi$=134.6$^{\text{o}}$ of the active HIS ground plane as can be seen from Fig. 5.1.4(b).

The above analysis assumes that the reflection phase of the HIS does not depend on the angle of incidence. In order to evaluate the angular stability of the proposed HIS, the reflection phase is presented in Fig. 5.3.3 for different HIS distances versus the angle of plane wave incidence θ_i. It can be seen that the reflection phase increases with the angle of incidence, showing that the proposed structure is not angularly stable. This instability can be attributed mainly to the electrically thick dielectric substrate on top of the array which introduces a different optical path depending on the angle of incidence and partly to the proposed design geometry. Consequently, this reflection phase variation of the HIS has been taken into account by expressing φ as a function of θ in (5.3-1) and the radiation patterns have been recalculated. In this case, the beam scanning range at f=54.6GHz for the same displacement is reduced to 41$^{\text{o}}$ as depicted in Fig. 5.3.2. Although the beam scanning

capability would be larger for an angularly stable design as shown from the analysis performed here, the proposed HIS still provides a significant scanning of the main beam. However, alternative designs can be considered with reduced dielectric substrate thickness, which would result in a more stable HIS structure and thus an increased beam scanning range.
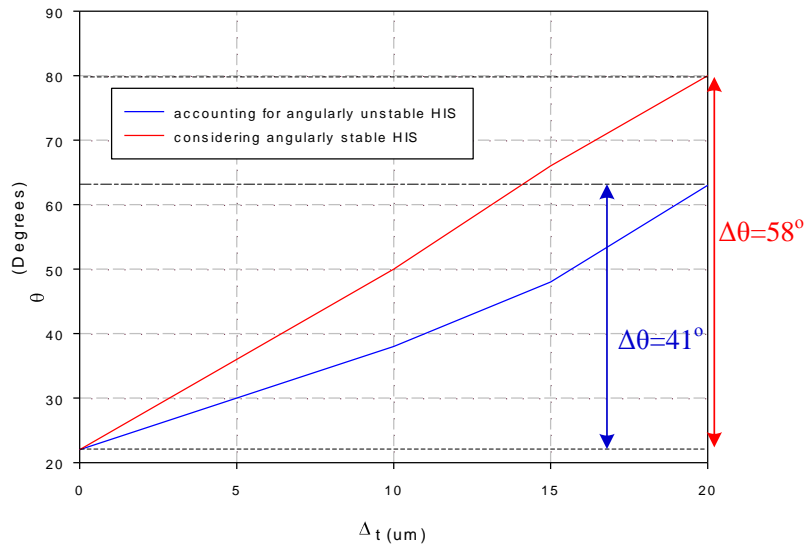

Fig. 5.3.2.   Angle of the radiated beam for operation at 54.6GHz as a function of the displacement Δt (with Δt=0μm corresponding to HIS distance t=50μm and Δt=20μm to t=70μm) considering both angularly stable and unstable HIS.
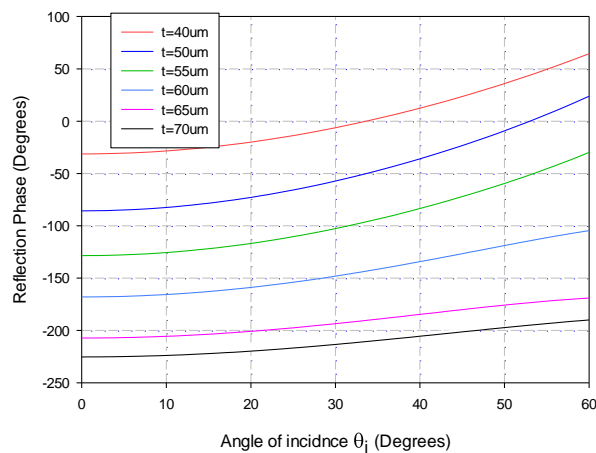

Fig. 5.3.3.   Simulated reflection phase of the proposed HIS at 54.6GHz versus the angle of incidence for different HIS thicknesses.

5.3.2 Finite Size Antenna

A practical finite size implementation of the proposed LWA has been designed and simulated in a full 3D EM software package (CST Microwave Studio™). Both the PRS and the HIS surfaces are formed by arrays of 3×19 elements. The antenna is fed by a dipole which is positioned in the cavity, towards the one end of the antenna. On the same side, a vertical metallic wall is placed where the antenna is terminated (Fig. 5.3.1a, b).

It is worth reminding here that the reflection phase of the proposed HIS was not zero at its resonant frequency (i.e. the frequency of the maximum slope in the reflection phase). The value of the phase has been taken into account in the design of the antenna since it is crucial for the definition of the cavity thickness. The antenna's performance has been simulated for different HIS cavity distances while keeping t_1 constant, and a beam reconfiguration with continuous scanning from 15° to 50° has been obtained for operation at 54.6GHz (Fig. 5.3.4a). The obtained beam scanning range $\Delta\theta=35^o$, corresponds to a phase shift of $\Delta\varphi=134.6^o$ of the tunable HIS ground plane as mentioned earlier for normal plane wave incidence. This phase shift changes the resonance condition of the antenna resonant cavity and thus controls θ for a fixed frequency of operation due to the frequency dispersion properties of LWAs. It should be noted that the operating frequency of the antenna is slightly different to the frequency of the maximum $\Delta\varphi$ achieved from the infinite size periodic HIS in section 5.1.1 (which is 54.3GHz). This is due to the finite size of the structure considered here and the expected discrepancy with the infinite size periodic model considered in section 5.1.1.

A maximum directivity of 16.4dBi has been achieved with the proposed antenna for 32° pointing angle of the main beam which corresponds to t=60um. The variation of the directivity for the other pointing angles is less than 3dB. However, it can be observed from Fig. 5.3.4(a) that for angles close to broadside the beamwidth is wide and it becomes narrower

as the beam is scanned to larger angles. This is a typical behavior of LWAs [9].

Finally, a 1D LWA antenna has been designed with a metallic ground plane (in the absence of the HIS) and a single PRS array, in order to investigate the tunability/sensitivity of such a structure compared to the proposed beam-scanning antenna. The antenna design consists of the 3×19 PRS array described earlier placed at a distance t=3.7mm above the ground plane. The cavity thickness has been selected such that an operation at the same frequency range (around 55GHz) is obtained. The directivity achieved is of similar value to the HIS based design. Following the same concept, the actuators can be employed to support the ground plane of the antenna, and bring it closer to the PRS when they are biased and displacement is produced. This will change the cavity distance and consequently the resonant frequency. The structure has been simulated in CST for three cavity distances, corresponding to a maximum displacement Δt=100μm.

The pointing angle of the main beam is shown in Fig. 5.3.4(b) for operation at 54.6GHz compared with the respective angle of the proposed beam-scanning antenna with the tunable HIS ground. For t=3.7mm, the angle is θ=33$^{\text{o}}$, with a scanning of just 2$^{\text{o}}$ achieved for t=3.6mm. Moreover, for Δt=20μm (from t=3.62mm to 3.6mm) less than 1$^{\text{o}}$ difference in the pointing angle is obtained. This suggests that the particular structure is much less sensitive in small cavity changes. The above study demonstrates the importance of the tunable HIS in the beam scanning LWA design, because the available displacement in the case of the HIS results in an extensive tuning of its reflection phase. The enhancement of the beam-scanning capability of LWA antennas with the introduction of a HIS as a ground plane was expected as it has already been demonstrated in [10].
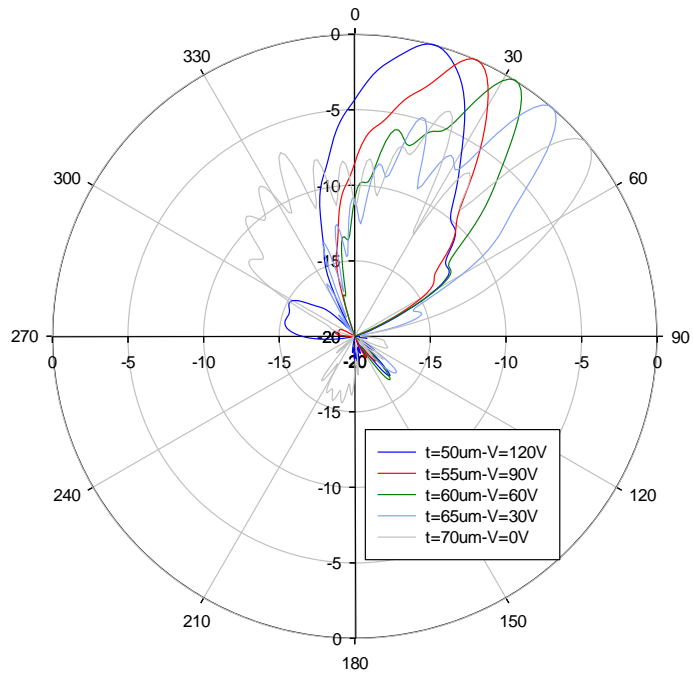
(a)
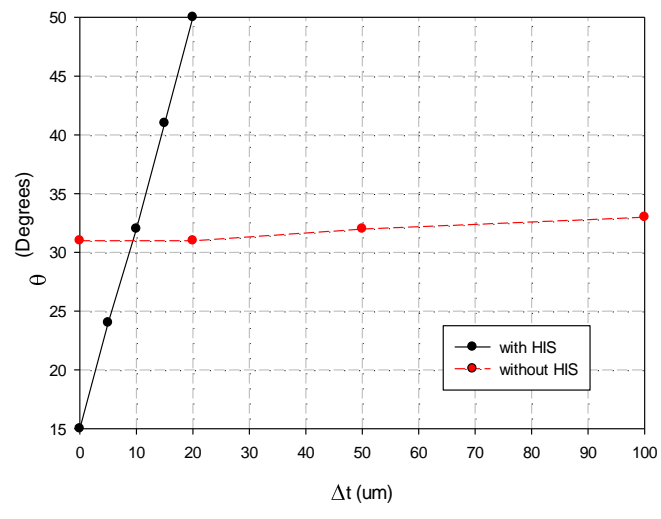
(b)

Fig. 5.3.4. (a) Simulated H-plane radiation patterns at 54.6GHz of the proposed beam-scanning hollow LWA, and (b) Angle the main beam versus the displacement Δt for the LWA with an active HIS ground plane and a conventional ground plane.

5.4 CONCLUSIONS

In this Chapter dynamically tunable low-loss HIS type phase shifting surfaces based on stack multilayer piezoelectric actuators have been demonstrated through simulation and experiments giving a phase shift of over 200° at 58.14GHz. The proposed technique is directly scalable to higher mm-wave and submm-wave frequencies, where more phase shift could be obtained with the same or even less available displacement, paving the way for the realization of a new class of tunable quasi-optical components. Different geometries and cavities have been investigated in terms of tuning range and losses performance. Moreover a continuous beam steering antenna application is proposed based on a 1D hollow Leaky-Wave Antenna (LWA) configuration formed by a Partially Reflective Surface (PRS) placed on top of the proposed tunable HIS. Continuous scanning of a highly directive beam from 15° to 50° is achieved at 54.6GHz.

REFERENCES

[1] O. Bayraktar, O. Civi, and T. Akin, "Beam switching reflectarray monolithically integrated with RF MEMS switches," *IEEE Trans. Antennas Propag.*, vol. 60, no. 2, pp. 854–862, Feb. 2012.

[2] C. Guclu, J. Perruisseau-Carrier, and O. Civi, "Proof of concept of a dual-band circularly-polarized RF MEMS beam-switching reflectarray," *IEEE Trans. Antennas Propag.*, vol. 60, no. 11, pp. 5451–5455, Nov. 2012.

[3] W. Hu, R. Dickie, R. Cahill, *et al.*, "Liquid crystal tunable mm wave frequency selective surface," *IEEE Microw. Wireless Compon. Lett.*, vol. 17, no. 9, pp. 667–669, Sep. 2007.

[4] W. Hu, M. Arrebola, R. Cahill, J. A. Encinar, V. Fusco, H. S. Gamble, Y. Alvarez, and F. Las-Heras, "94 GHz dual reflector antenna with reflectarray subreflector," *IEEE Trans. Antennas Propag.*, vol. 57, no. 10, pp. 3043–3050, Oct. 2009.

[5] G. Perez-Palomino, P. Baine, R. Dickie,M. Bain, J. Encinar, R. Cahill, M. Barba, and G. Toso, "Design and experimental validation of liquid crystal-based reconfigurable reflectarray elements with improved bandwidth in F-band," *IEEE Trans. Antennas Propag.*, vol. 61, no. 4, pp. 1704–1713, Apr. 2013.

[6] G. V. Trentini, "Partially reflecting sheet array", IRE Trans. Antennas Propag., vol. AP-4, pp.666 -671, 1956.

[7] A. P. Feresidis and J. C. Vardaxoglou, "High gain planar antenna using optimised partially reflective surfaces," *IEE Proc. Microw. Antennas Propag*., vol. 148, no. 6, pp. 345-350, Dec. 2001.

[8] A. P. Feresidis, G. Goussetis, S. Wang, and J. C. Vardaxoglou, "Artificial magnetic conductor surfaces and their application to low profile high-gain planar antennas," *IEEE Trans. Antennas Propag.*, vol. 53, no. 1, pp. 209–215, Jan. 2005.

[9] A. Oliner. "Leaky-wave antennas," in Antenna Engineering Handbook, Third Edition, edited by *R. C. Johnson, McGraw Hill*, 1993.

[10] M. García-Vigueras, J. L. Gómez-Tornero, G. Goussetis, A. R. Wiley, and Y. J. Guo, "Enhancing frequency-scanning response of leaky-wave antennas using high impedance surfaces," *IEEE Antennas Wireless Propagat. Lett.*, vol. 10, pp. 7–10, Mar. 2011.

[11] S. Lim, C. Caloz, and T.Itoh, "Electronically scanned composite right/left handed microstrip leaky-wave antenna," *IEEE Microwave and Wireless Components Lett.*, vol. 14, no. 6, pp. 277-279, June 2004.

[12]   R. Guzmán-Quirós, J.-L. Gómez-Tornero, A. R. Weily, and Y. J. Guo, "Electronically steerable 1D Fabry-Perot leaky-wave antenna employing a tunable high impedance surface," *IEEE Trans. Antennas Propag.*, vol. 60, no. 11, pp. 5046–5055, Nov. 2012.

[13]   B. Munk, *Frequency Selective Surfaces: Theory and Design*, Wiley, 2000.

[14]   www.physikinstrumente.co.uk

[15]   E. O. Hammerstad and F. Bekkadal, *A Microstrip Handbook*, ELAB Report, STF 44 A74169, University of Trondheim, Norway, 1975, pp 98-110.

CHAPTER 6.

TUNABLE FREQUENCY SELECTIVE META-SURFACES

The term "meta-surfaces" is used to describe periodic arrays of either metallic elements printed on a dielectric substrate or apertures in a conducting plane. They are normally made of non-resonant unit cells of sub-wavelength dimensions [1] in contrast to the well-known Frequency Selective Surfaces (FSS) which consist of larger resonant unit cell dimensions [2, 3]. As explained in Chapter 1, in order to obtain tuning of an FSS response, a change on the effective size of the element has to be performed. This has been achieved in recent years by introducing varactor [4] or PIN diodes [5] on each element for low frequency applications, or MEMS [6, 7] for mm-wave frequencies. Moreover, tunable substrates have been employed, where by changing the permittivity of the substrate the guided wavelength is changed resulting in a different operating frequency. Such tunable substrates can be ferroelectric substrates [8] for lower microwave frequencies which have the disadvantage of high losses, and liquid crystals which are suitable for higher mm-wave frequencies but also exhibit high losses and very low switching speeds [9].

In this Chapter, tunable Frequency Selective Meta-Surfaces (FSmS) are investigated for both lower and higher mm-wave frequencies applying the tuning techniques described in Chapters 4 and 5 respectively. Initially, a novel design of multi-layer Frequency Selective Meta-Surfaces (FSmS) is presented achieving significant tuning of the pass-band response with low losses, operating at low mm-wave frequencies. The proposed FSmS consist of multiple layers of closely spaced non-resonant sub-wavelength periodic meta-surfaces creating air cavities between them. A pass-band response is produced which is tuned using bender piezoelectric actuators that change the distance between two of the surfaces. This

alters the resonance condition of the complete structure and thus the central frequency of the pass-band. Alternative designs are also being investigated and compared with the proposed FSmS. Finally, a tunable FSmS for higher mm-wave frequencies consisting of two square aperture arrays printed on dielectric substrates and separated by an air cavity is investigated. In this case, tuning of the band-pass filter response of the double layer FSS is achieved using stack piezoelectric actuators positioned below one of the meta-surfaces. The actuators dynamically change the thickness of the air cavity, due to their property of expanding vertically under DC biasing, which results in tuning the transmission characteristics of the structure. Simulation results are presented validating the behaviour of the proposed structures. Moreover, measurements for the multi-layer tunable FSmS (operating at lower mm-wave frequencies) have been carried out and are included in the Chapter.

6.1 TUNABLE FREQUENCY SELECTIVE META-SURFACES FOR LOWER MILLIMETRE-WAVE FREQUENCIES

In this section, tunable Frequency Selective Meta-Surfaces (FSmS) structures for lower mm-wave frequencies are investigated based on bender actuators. Initially, a double layer structure is studied. It comprises two periodic arrays of aperture FSS separated by a half wavelength air cavity. Subsequently, a multi-layer structure is investigated. This is formed by an array of metallic square loops placed between two arrays of square apertures in metallic sheets, separated by sub-wavelength air cavities. The main feature of the proposed FSmS designs is that their operation is based on a resonant cavity effect, and not the resonance of the periodic array elements (which are of sub-wavelength dimensions).

6.1.1 Design of Double-Layer FSmS (λ/2 cavity)

As explained in section 2.1.2, a Fabry-Perot type resonant cavity can be typically obtained

from two periodic arrays acting as Partially Reflective Surfaces (PRS), i.e. FSSs operated at frequencies away from their resonance, placed at half-wavelength distance from each other [10]. This resonant cavity normally produces a pass-band response. Thus, tuning of the pass-band is obtained by changing the resonant cavity thickness which alters the resonance condition. This is achieved using bender piezoelectric actuators as in the case of the tunable HIS structures proposed in Chapter 4.

Initially, a double-layer structure is considered as illustrated in Fig. 6.1.1. It is designed to operate around 15GHz and it consists of two Partially Reflective Surfaces (PRS$_1$ and PRS$_2$ in the figure). Both PRSs are identical, formed by 2D periodic arrays of square apertures etched off metallic sheets, printed on thin dielectric substrates. The unit cell of the structure is shown in Fig. 6.1.2. The substrate thickness is h=0.055mm while its permittivity is ε_r=3. The periodicity of the structure is p=7mm and the dimensions of the square apertures are d_{a1}= d_{a2}=4.5mm (~λ/4 at 15GHz) as illustrated in Fig. 6.1.2. Moreover, the cavity thickness is varied from t=7.5mm to t=8.5mm which is slightly less than half-wavelength at 15GHz. This change in the cavity thickness is performed employing the bender actuators which produce a displacement Δt under DC bias (Fig. 6.1.1). However, in order to evaluate the performance and tunability of the FSmS structure, full wave simulations are carried out in CST applying periodic boundary conditions to the unit cell.
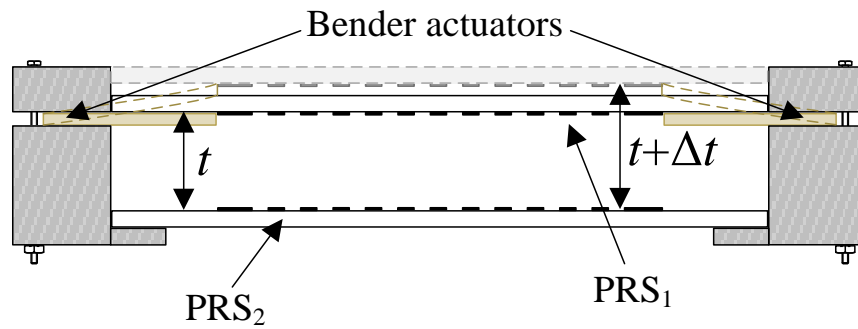
Fig. 6.1.1.   Schematic diagram of proposed tunable double-layer FSmS (dimensions are not to scale).
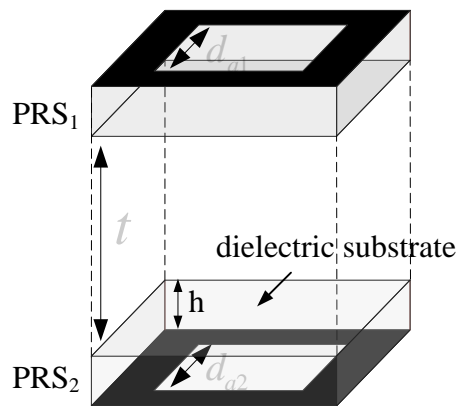

Fig. 6.1.2.   Unit cell of proposed tunable double-layer FSmS.

In the simulation software, the change in the cavity thickness is modelled by parametrically changing the value of t. The extracted transmission magnitude under plane wave normal incidence is depicted in Fig. 6.1.3. It can be observed that a pass-band response is produced as expected with a very low insertion loss. The central frequency of the pass-band is tuned from 17.08GHz to 15.39GHz (Δf=1.69GHz) for a displacement Δt=1mm. Thus, a significant tuning can be achieved from the particular tunable FSmS. However as shown in section 6.1.3, due to the large profile, the structure is very sensitive to changes of the angle of incidence.
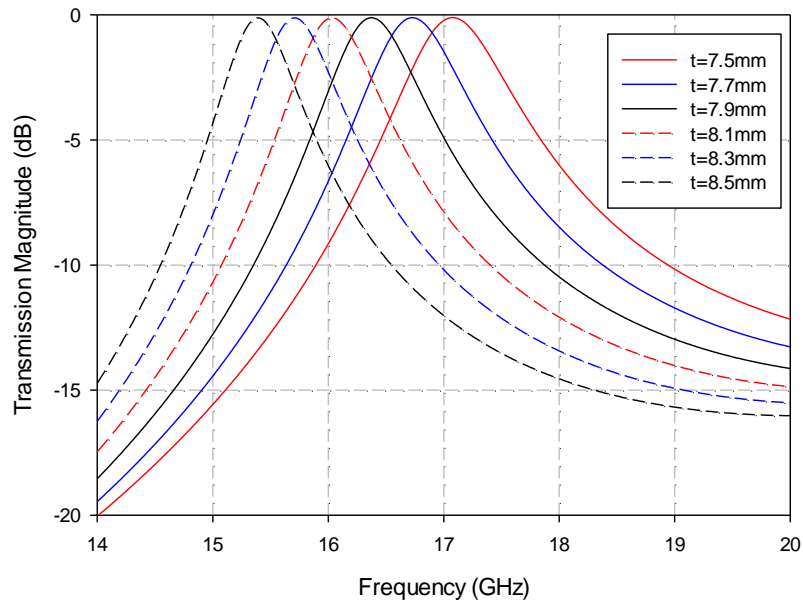
Fig. 6.1.3.   Simulated transmission magnitude of proposed tunable double-layer FSmS for different cavity thicknesses t.

6.1.2 Design of Multi-Layer FSmS (sub-wavelength cavities)

Subsequently, a novel multi-layer Frequency Selective Meta-Surfaces (FSmS) configuration is investigated. The proposed FSmS is based on the double-layer FSmS of the previous section. More particularly, one of the PRSs of the double-layer FSmS is replaced by a composite double-layer structure described in section 6.1.2.1, acting both as a PRS and a HIS. This composite structure will be referred to as High Impedance Partially Reflective Surface (HI-PRS) and it consists of an array of square loop metallic patches printed on a thin substrate and an array of square apertures on a metallic sheet printed on the same type and thickness substrate (Fig. 6.1.4a). The two surfaces are separated by a sub-wavelength air cavity t. Next, the other PRS is placed at a distance S from the HI-PRS (Fig. 6.1.4 a, b). Due to the reflection phase values of the HI-PRS, a significant reduction of the cavity thickness S and therefore the overall profile of the FSmS is achieved as explained in section 6.1.2.2. Tuning of the pass-band response is obtained by changing the HI-PRS cavity t using the

bender actuators which alters the reflection phase and consequently the resonance condition.
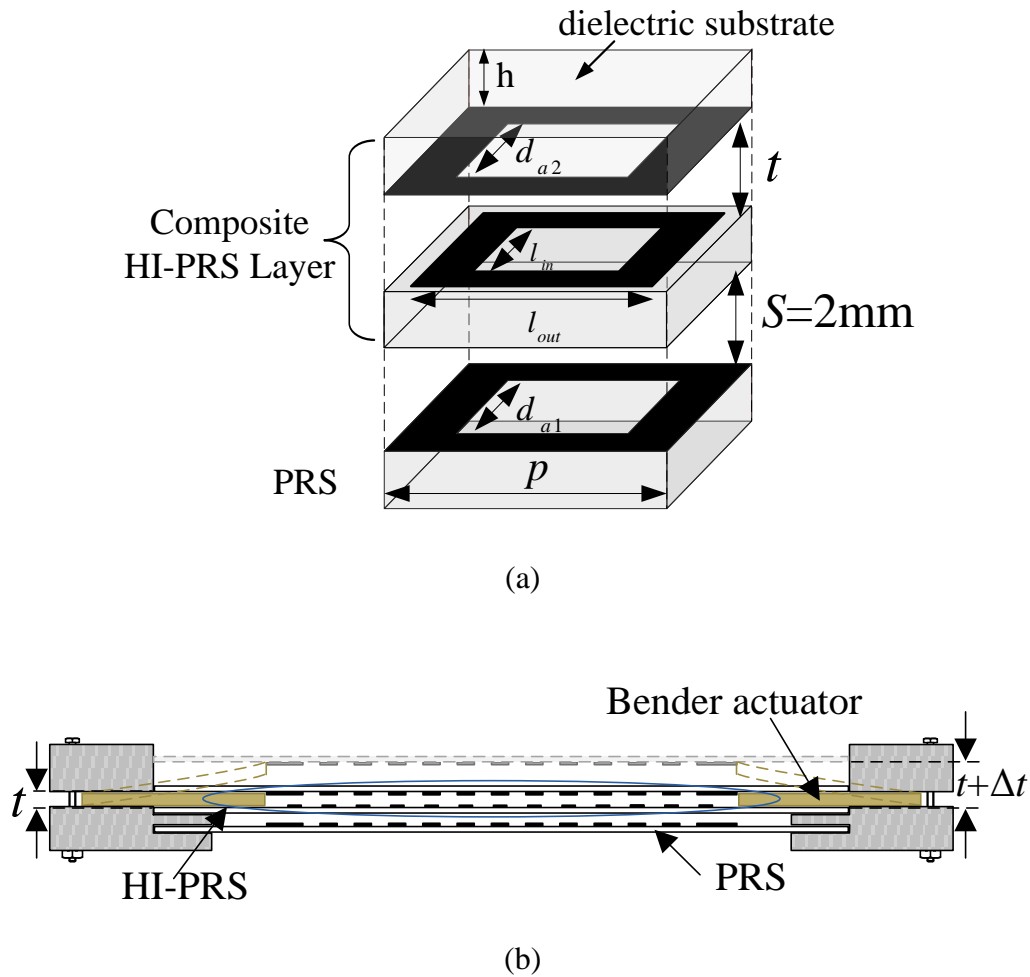

(a)

(b)

Fig. 6.1.4.   Unit cell of the multi-layer FSmS, (b) Schematic diagram of proposed tunable FSmS structure (dimensions are not to scale).

6.1.2.1 *Design of High Impedance Partially Reflective Surface*

It is well known that in order to obtain a HIS response, a periodic surface has to be placed at close proximity to a ground plane or to be printed on a grounded substrate. At such structures no transmission occurs, and total reflection of the incident waves takes place. However, it has been shown in recent works [11] that if the ground plane is replaced with a non-resonant aperture array (inductive surface), the high impedance response is maintained, while obtaining

a partial transmission/reflection of incident waves.

Based on the above, the HI-PRS has been designed starting from the HIS of section 4.1.1. A square loop array is printed on a thin dielectric substrate with thickness h=0.055mm and ε_r=3. The periodicity of the structure and the dimensions of the square loop element are p=7mm, l_{out}=5mm and l_{in}=3.5mm (see Fig. 6.1.4a) which are slightly modified compared to the HIS dimensions of section 4.1.1. Moreover, the ground plane is replaced with a square aperture array of the same periodicity (p=7mm) and aperture size d_{a2}=4.5mm. The array is printed on the same type and thickness substrate and placed over the square loop array at a distance t as shown in Fig. 6.1.4.

The structure has been simulated in CST for different cavity distances t from 1mm to 3mm and the extracted reflection coefficients for normal incidence are depicted in Fig. 6.1.5. It can be seen from the magnitude of the reflection coefficient (Fig. 6.1.5a), that a partial reflection is obtained, while a high impedance operation in terms of the reflection phase is achieved for operation between approximately 10GHz and 15GHz for the particular cavity thicknesses (Fig. 6.1.5b). In Fig. 6.1.5(a), it is shown that the minimum of the reflection magnitude becomes less prominent as the cavity thickness increases corresponding to higher reflection and reduced transmission of the incident plane wave. Moreover, Fig. 6.1.5(b) shows a decreased slope of the reflection phase for increased cavity thickness.
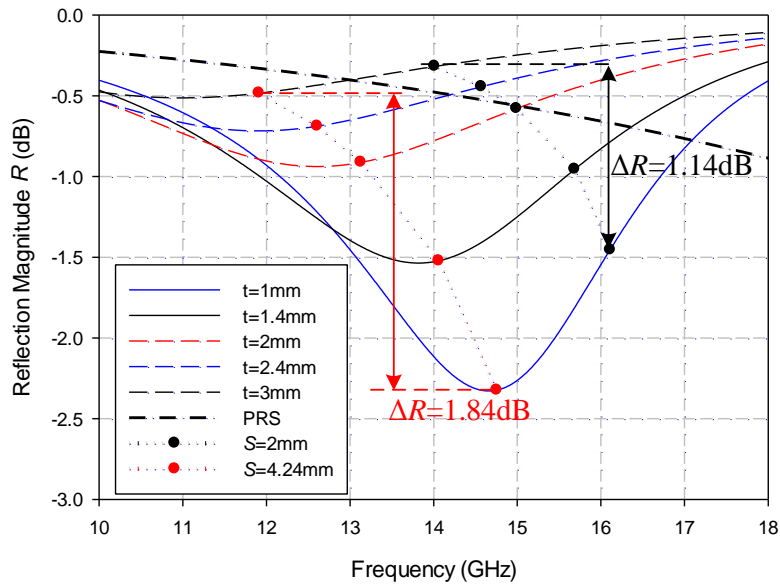
(a)
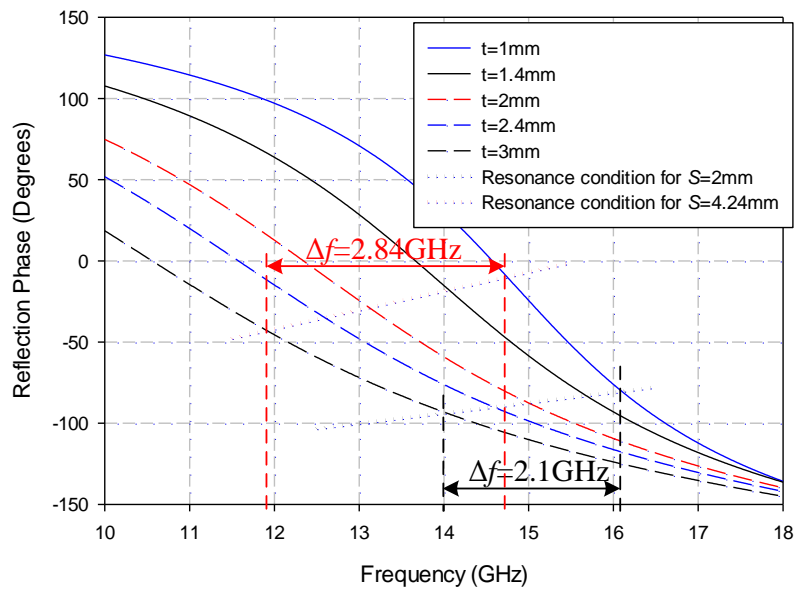
(b)

Fig. 6.1.5.   Simulated reflection (a) magnitude of the HI-PRS and the PRS and (b) phase

of the HI-PRS for different cavity distances *t* for normal incidence. The resonance condition

for two alternative designs is also shown.

### 6.1.2.2 *Frequency Selective Meta-Surfaces Based on High Impedance PRS*

The HI-PRS described in the previous section is subsequently employed to create the proposed FSmS (Fig 6.1.4). The square aperture PRS placed at distance *S* below the HI-PRS has periodicity equal to the periodicity of the HI-PRS array (*p*=7mm), while the size of the aperture is d_{a1}=4.5mm. As explained earlier, the concept of the proposed FSmS is based on a cavity type resonance, which is obtained by satisfying the resonance condition (2.1-5) which is written as:

$$\varphi_{HI-PRS} + \varphi_{PRS} - \frac{2\pi}{\lambda} 2S = \pm 2N\pi , \quad N=0,1,2... \tag{6.1-1}$$

where $\varphi_{HI\text{-}PRS}$ is the reflection phase of the HI-PRS, φ_{PRS} the reflection phase of the PRS and λ the free space wavelength. For operation at 16.11GHz, substituting the reflection phase of the HI-PRS for *t*=1mm which is $\varphi_{HI\text{-}PRS}$=−80.88$^\mathrm{o}$ (Fig. 6.1.5b) and the reflection phase of the PRS which is φ_{PRS}=157.81$^\mathrm{o}$ in (6.1-1), the cavity distance is calculated to be *S*=2mm. Indeed, from the simulated transmission coefficient magnitude of the proposed FSmS for *t*=1mm and *S*=2mm shown in Fig. 6.1.6(a), a pass-band is observed at *f*=16GHz which is very close to the calculated operational frequency from the theoretical analysis.

By employing the same tuning technique as in the case of the tunable HIS structures of Chapter 4, the reflection phase of the HI-PRS can be tuned. This is achieved using the bender actuators to increase the cavity distance *t* by displacing the upper layer of the composite structure, as illustrated in Fig. 6.1.4(b). It is expected that if the cavity distance *S* between the PRS and the HI-PRS is kept constant, then the resonance condition (6.1-1) will be satisfied for lower frequencies as *t* increases and tuning of the pass-band will be obtained. This can be demonstrated from the black dotted line in Fig. 6.1.5(b) which shows the ideal phase for the HI-PRS that satisfies the resonance condition (6.1-1). The points where the dotted line

intersects the simulated reflection phase define the expected tuning range which as can be seen from the figure is 2.1GHz for displacement from t=1mm to t=3mm. Indeed, the transmission response of the proposed tunable FSmS for t between 1mm and 3mm is presented in Fig. 6.1.6(a) and shows a tuning of the pass-band from 16GHz to 14GHz, which is only slightly less than that expected from the theoretical analysis. Moreover, it can be observed that the insertion loss is between 0.28dB (t=2mm) and 0.85dB (t=1mm). The corresponding reflection magnitude of the structure is also shown in Fig. 6.1.6(b). The reflection magnitude is below −10dB for all cavity distances, except from t=1mm where it is slightly higher than −10dB.
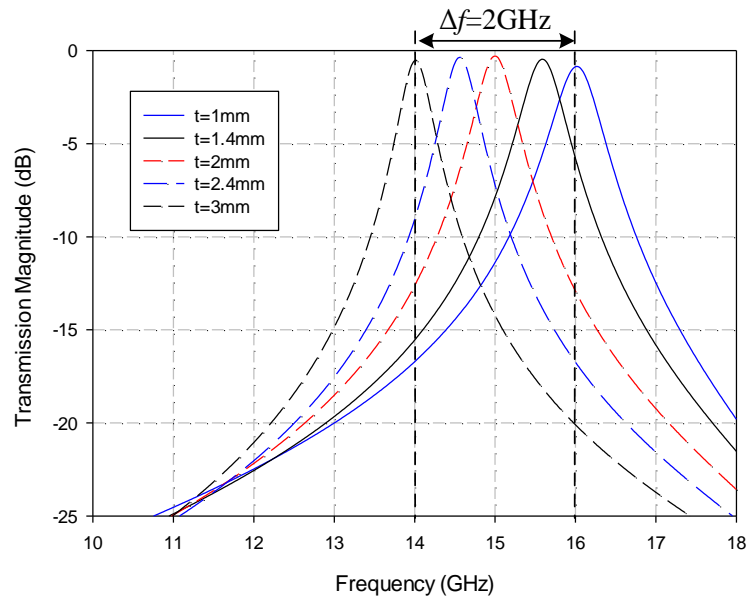

(a)
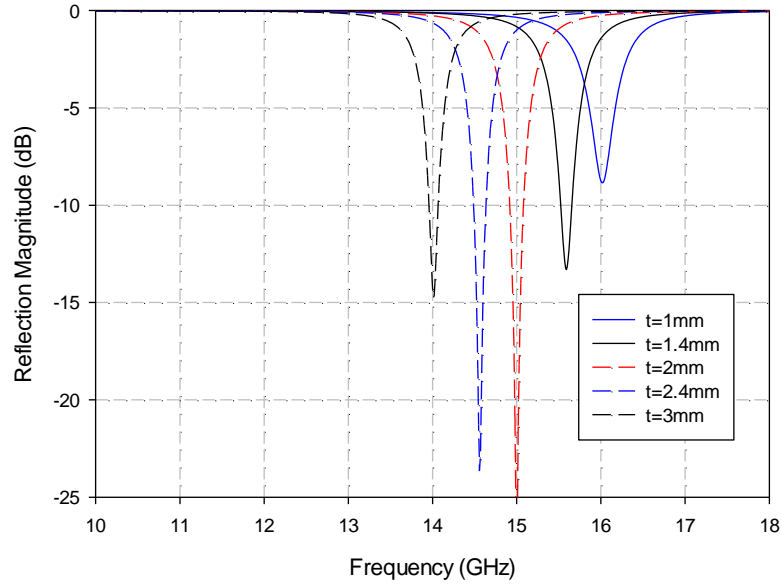
(b)

Fig. 6.1.6.   Simulated (a) transmission and (b) reflection of the proposed tunable FSmS for different cavity distances t (keeping S=2mm).

The slightly increased insertion loss at the extreme cases of t=3mm and more significantly t=1mm is attributed to mismatch effects and becomes more pronounced in the following case. If the HI-PRS is operated close to the AMC frequency, and more specifically where the reflection phase is $\varphi_{HI\text{-}PRS}$=-10°, then from (6.1-1) the cavity thickness S becomes equal to 4.24mm. For this case, the ideal reflection phase $\varphi_{HI\text{-}PRS}$ versus frequency is presented in Fig. 6.1.5(b) with the red dotted line. Consequently, the estimated tuning range of an alternative FSmS structure with S=4.24mm, can be extracted again from the intersection points of the ideal phase with the reflection phase for t=1mm and t=3mm. Therefore, as can be seen from the figure, the expected tuning range is Δf=2.84GHz which is larger than the one obtained from the design with S=2mm. This is also shown from the transmission response of the new structure for t=1mm to t=3mm (Fig. 6.1.7a), with the pass-band tuned from 14.77GHz to 11.92GHz (Δf=2.85GHz). This increase in the tuning range of this particular alternative

structure is expected, since as we move towards the point where the reflection phase is zero, the phase curves for different cavity distances t tend to exhibit higher spectral separation, whereas at higher frequencies the phase curves tend to converge (Fig. 6.1.5b).

However, although the last design has the advantage of a larger tuning range compared to the first design, it exhibits worse performance in terms of the insertion loss, particularly for small values of t. This is evident from the transmission coefficient as well as the reflection coefficient response of the structure (Fig. 6.1.7b). The latter is below -10dB only for the case of $t=3$mm while the insertion loss is 2.33dB for $t=1$mm. This effect is related to the resonant cavity nature of the structure. Such structures should have similar reflectivities between the layers forming the cavity in order to avoid impedance mismatch which causes increased insertion loss [10]. Therefore, a better explanation of the observed insertion loss can be obtained from Fig. 6.1.5(a), showing the reflection magnitude R of the PRS, as well as the values of R of the two HI-PRS designs at each operating frequency (corresponding to the different cavity distances t) with the dotted lines. It can be observed that the reflection magnitude of the HI-PRS with $S=4.24$mm (red dotted line) exhibits a large variation for $t=1$mm to $t=3$mm with respect to that of the PRS. In contrast, in the case of the proposed HI-PRS with $S=2$mm (black dotted line) the total variation of the reflection magnitude is significantly less ($\Delta R=1.14$dB as opposed to 1.84dB for the case of $S=4.24$mm) and follows closer the reflection magnitude of the PRS, resulting in better performance in terms of insertion loss. The losses have also been assessed using the expression $1 - \left|S_{11}\right|^2 - \left|S_{21}\right|^2$ and it has been observed that the maximum losses at resonance are between 2% for $t=1$mm to 5% for $t=3$mm. In fact the $t=1$mm case has less losses, so indeed the insertion loss is caused by the impedance mismatch.
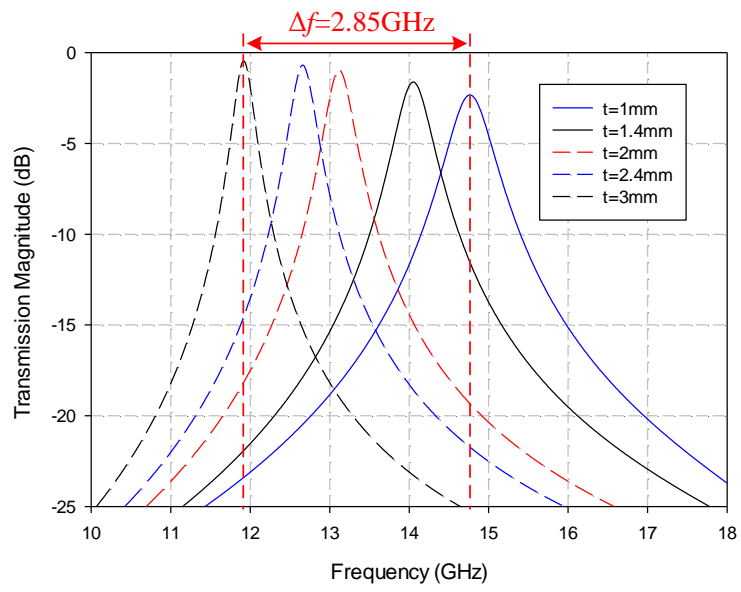
(a)
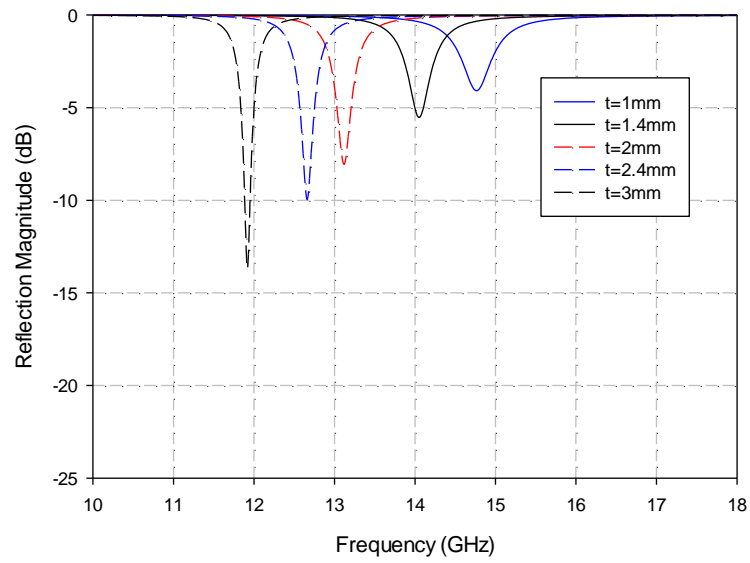
(b)

Fig. 6.1.7. Simulated (a) transmission and (b) reflection response for alternative design with *S*=4.24mm for different HI-PRS cavities.

6.1.3 Angular Stability Study

So far, it has been demonstrated that the double-layer tunable FSmS and both alternative designs of the multi-layer tunable FSmS can provide a significant tuning of the pass-band filter response. One could claim that the first design (section 6.1.1) should be chosen, as it is more simple compared to the other two presented in this Chapter (section 6.1.2). Nevertheless, as already mentioned in section 6.1.1, it is expected that it is not angularly stable due to the large separation between its two layers. Indeed, simulations are performed for the magnitude of the transmission coefficient for angles of incidence 0° and 30° which show that a large frequency shift of the pass-band is obtained with the angle of incidence (Fig. 6.1.8). More specifically, it can be seen from Fig. 6.1.8 that for t=7.5mm a 13.2% frequency shift is exhibited, while the corresponding frequency shift for t=8.5mm is 13.5% (i.e. slightly higher as the cavity thickness increases).
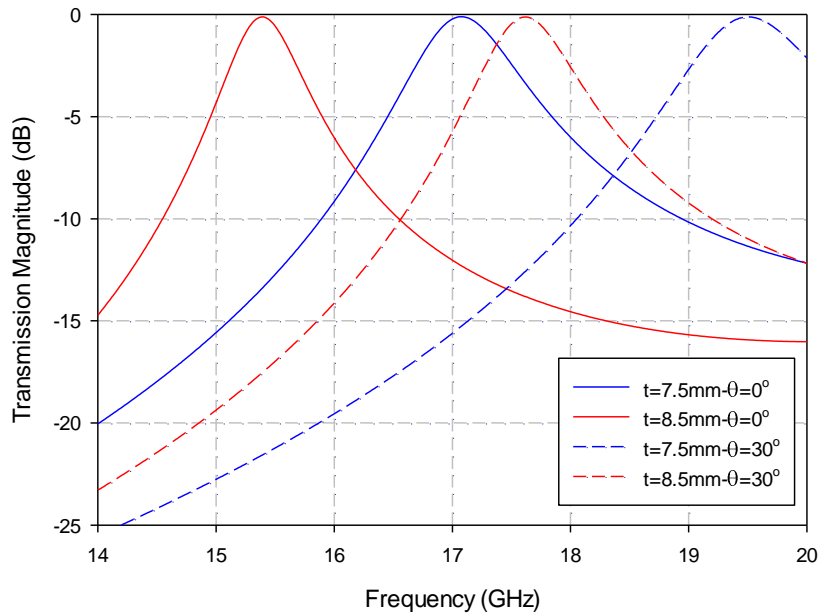

Fig. 6.1.8.   Angular stability study for the double-layer tunable FSmS with half-wavelength cavity.

Consequently, the two multi-layer designs (section 6.1.2) are expected to provide a better performance in terms of angular stability due to the reduced profile. Thus, the performance of the two designs is also evaluated. The design with S=2mm has a total profile varying from $\lambda/6$ for t=1mm to $\lambda/4$ for t=3mm, while for the case of S=4.24mm the profile is at least $\lambda/3$. As expected, this thinner profile results in a more angularly stable structure, which is evident from Fig. 6.1.9. In particular, the figure shows the transmission response for t=1mm for both designs with angles of incidence from 0° to 30°. It can be seen that the proposed structure exhibits a very small shift (1.1%) while the design with S=4.24mm undergoes a shift from 14.77GHz to 15.24GHz (3.1%). The proposed concept of multi-layer FSmS structures can be extended to even thinner cavities with optimised HI-PRS and PRS which will provide even better angular stability, but this is not within the scope of this thesis.
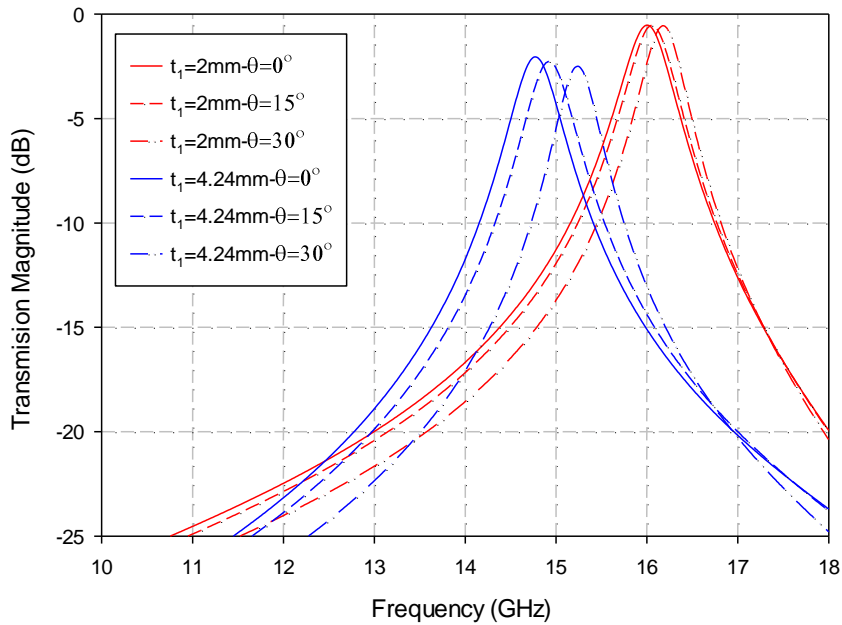

Fig. 6.1.9.   Angular stability study for the proposed tunable FSmS with S=2mm, and the design with S=4.24mm (t=1mm).

6.1.4 Measurements

Finally, a prototype of the proposed tunable FSmS has been fabricated in order to experimentally validate the concept. Three periodic arrays of 35×35 elements have been fabricated, two arrays of square apertures etched off a copper sheet and one array of square loop copper elements. Each of the arrays has been printed on thin polyester films with ε_r=3, tanδ=0.03, thickness 0.055mm and overall dimensions 250mm×250mm (12.5λ×12.5λ). Photographs of the fabricated periodic arrays are shown in Fig. 6.1.10. To facilitate the measurement set up and define the fixed distance *S*=2mm, the PRS array has been glued on a 2mm thick Rohacell-51 substrate (ε_r≈1) (Fig. 6.1.10a). The square loop array has been glued to the other side of the Rohacell-51 substrate, carefully aligning the two arrays (Fig. 6.1.10b). Subsequently, spacers of 1.1mm thickness where placed around the square loop array where the bender actuators have been positioned. Finally, the other square aperture array (forming the upper layer of the composite HI-PRS) has been glued to polystyrene foam (Fig. 6.1.10c) to make it rigid and placed on top, supported by the actuators. The bender actuators that have been used for this measurement are (as in the case of the tunable HIS measurement presented in Chapter 4) the PL140.11 from Physik Instrumente[TM] (PI), which achieve a nominal maximum displacement of 1mm [12]. Two horn antennas have been used for the measurement of the transmission characteristics of the fabricated prototype for different voltages applied to the actuators. The measured transmission response in comparison with the corresponding simulated results is shown in Fig. 6.1.11. Good agreement has been obtained with an achieved tuning of 8.8% for Δt=1.2mm. Moreover, a dynamic range of more than 20dB at 15.3GHz has been achieved for voltages 0V and 60V, demonstrating that the proposed FSmS can be tuned from a transmitting to a reflecting structure. It should be pointed out at this point that the actuators used for this measurement produced a displacement of 1.2mm which is within the ±20% of manufacturing error [12].
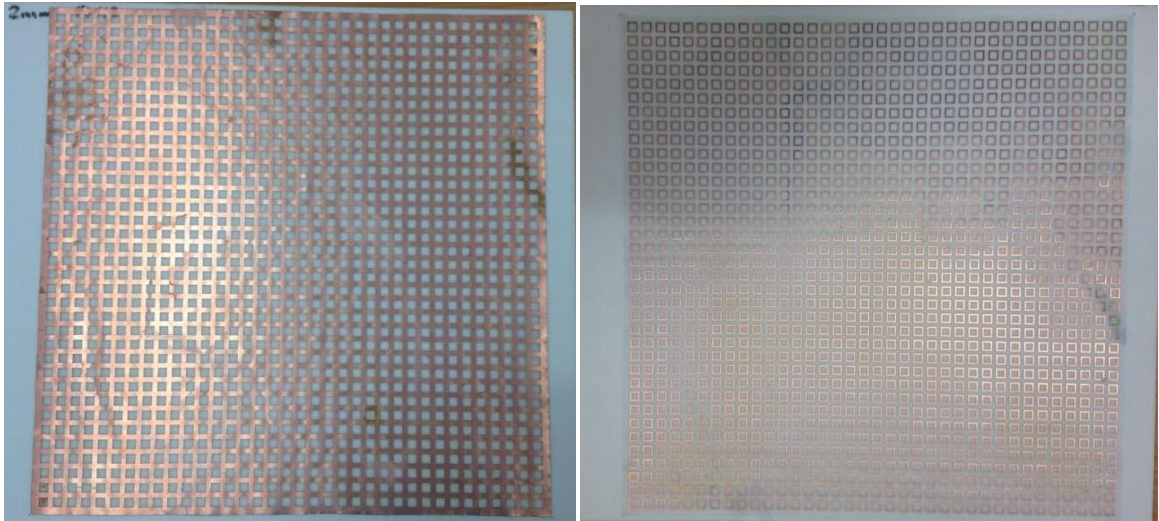
(a)   (b)
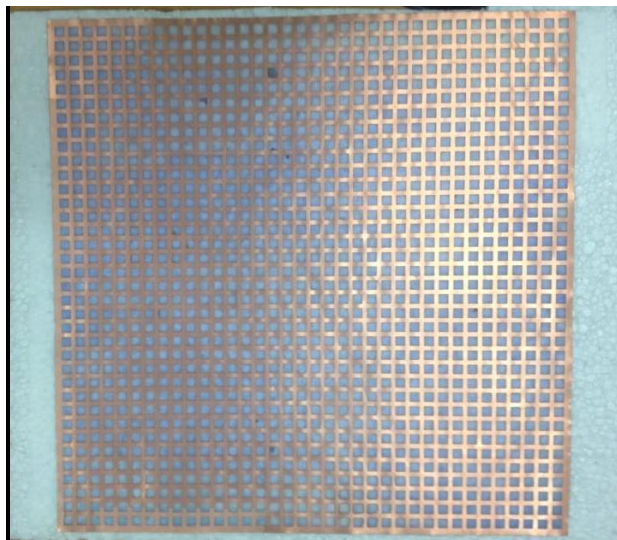
(c)

Fig. 6.1.10.   Photographs of fabricated arrays. (a) PRS, (b) Square loop array from HI-PRS
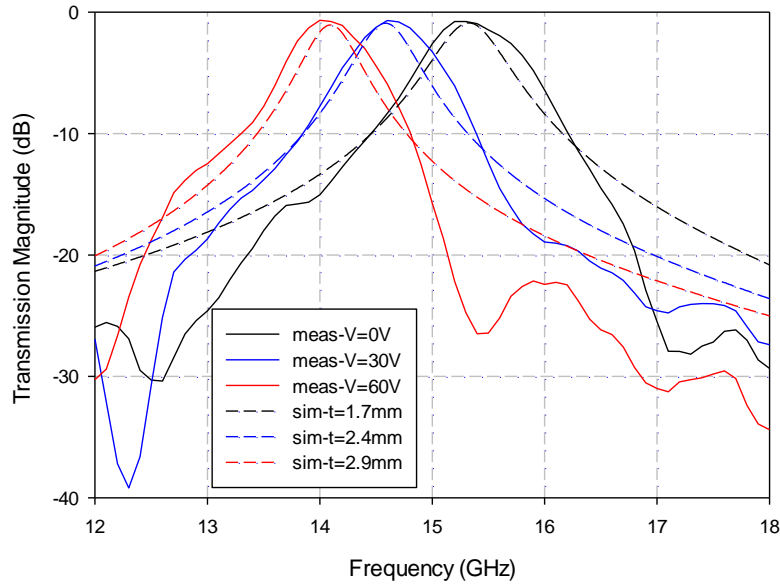
and (c) Square aperture array from HI-PRS.

Fig. 6.1.11.   Measured transmission magnitude for different voltages and comparison with simulated results.

6.2 TUNABLE FREQUENCY SELECTIVE META-SURFACES FOR HIGHER MILLIMETRE-WAVE FREQUENCIES

Next, a double-layer FSmS structure is investigated operating around 60GHz. The structure is illustrated in Fig. 6.2.1. It should be highlighted that the proposed FSmS consist of non-resonant elements of sub-wavelength dimensions as in the case of the proposed FSmS structures presented in the previous paragraph. It is formed by two identical meta-surfaces placed at distance *t* from each other with the periodic arrays facing the inside of the cavity. The piezoelectric actuators employed for the configurations under investigation are stack actuators which are used to support the lower of the two layers as can be seen from Fig. 6.2.1. When biased, they produce a displacement which dynamically changes the cavity distance between the two layers of the structure bringing them closer to each other. Since the actuators are placed around the meta-surfaces, they do not interfere with the radiation performance and hence the proposed configurations result in particularly low loss values.
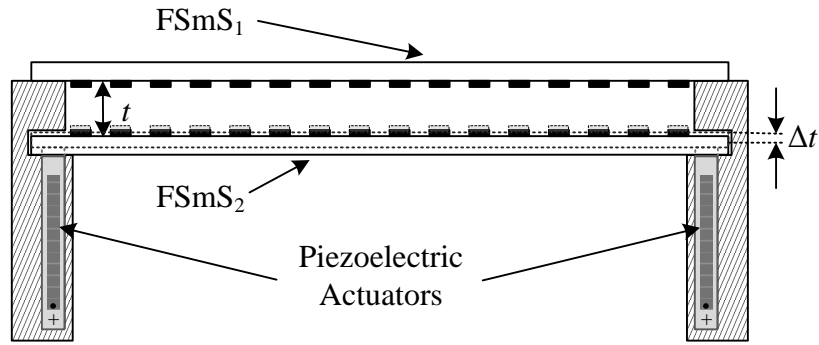
Fig. 6.2.1.   Schematic diagram of the proposed tunable double-layer FSmS.

6.2.1 Unit Cell Design

The unit cell for both meta-surfaces consists of a square aperture on a metallic sheet as shown in Fig. 6.2.2. The sheet is printed on a dielectric substrate with thickness h=0.8mm, and properties ε_r=2.2 and $tan\delta$=0.009. The periodicity of the structure is p=1.75mm while the aperture is d_a=0.7mm. The initial cavity thickness is set to t=3.37mm which gives a cavity resonance, i.e. a band-pass response at around 61.7GHz for 45° angle of incidence. Since this is a large cavity ($>\lambda/2$), the structure is not angularly stable, hence it has been designed for a fixed angle of incidence which is suitable for applications such as quasi-optical filters. The magnitude of the transmission and reflection coefficients versus frequency has been extracted simulating the unit cell of the double-layer structure in CST simulation software applying periodic boundary conditions.

(a)   (b)
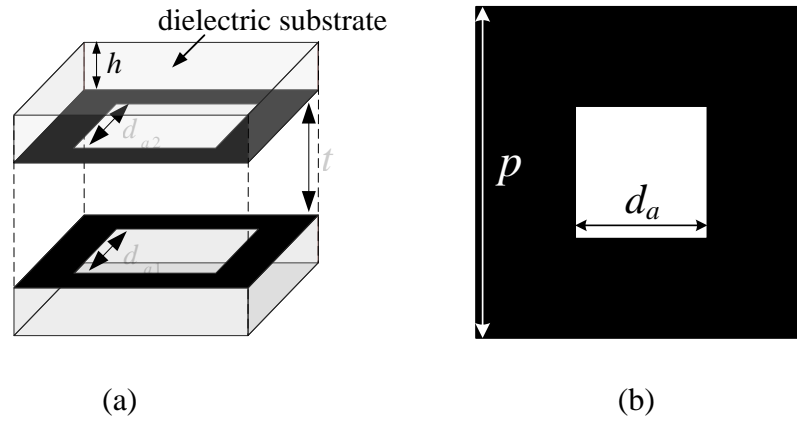
Fig. 6.2.2.　　Unit cell of the proposed double-layer FSmS (a) perspective and (b) top view.

The simulated results for different cavity distances from t=3.37mm to t=3.35mm are shown in Fig. 6.2.3. It can be observed that for t=3.37mm (unbiased actuators) the pass band is centred at 61.75GHz with an insertion loss of 0.7dB. For a displacement of Δt=10μm and Δt=20μm, the resonance frequency is shifted to 61.9GHz and 62.1GHz respectively. Moreover, the magnitude of the transmission coefficient at 62.1GHz is changed from -0.7dB to -11.8dB for Δt=20μm giving an achieved dynamic range of 11.1dB. The achieved tuning shows that the proposed double layer FSmS can be dynamically switched between a transmitting and a reflecting structure.

Fig. 6.2.3.   Simulated reflection and transmission magnitude of the proposed tunable double-layer FSmS for different cavity thicknesses.
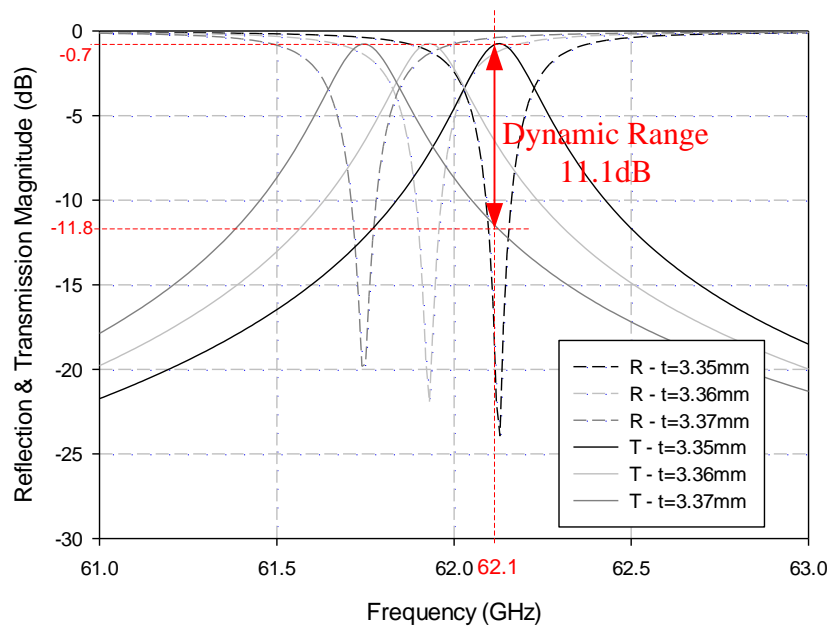
6.2.2 Losses Evaluation

In section 6.2 it has been stated that the proposed structure exhibits low losses which is a very important aspect, particularly for higher mm-wave frequencies. Therefore, an evaluation is carried out in this section of the main factors contributing to the losses in the proposed configuration. Three different cases have been considered in order to estimate whether the dielectric material or the metallic losses are more significant. Initially, both dielectric and metal losses are taken into account in the simulation, then only the dielectric losses are considered and finally both materials are considered lossless. This has been performed for the case of t=3.37mm. When all losses are taken into account, the insertion loss of the structure at the resonance is 0.77dB. In the case where only dielectric losses are considered in the simulations, the corresponding insertion loss is 0.042dB. Finally, if both materials are considered lossless the insertion loss is 0.01dB. This means that about 0.73dB are attributed

162

to the metal with only 0.03dB related to the dielectric substrates. Nevertheless, the total exhibited losses are very low.

Moreover, another study has been carried out to validate the choice of the air cavity in the proposed structure. The most important reason for choosing an air cavity as opposed to a dielectric filled one (with the two meta-surfaces printed on either side of the substrate), is to able to control the transmission characteristics by changing the cavity thickness. However, the reason that the arrays are facing the inside of the cavity and not the dielectric is to avoid losses. It has been shown from simulations that an alternative configuration with the periodic surfaces placed upside-down, so that the arrays are facing the outside of the cavity (Fig. 6.2.4) exhibits more losses. A comparison of the transmission magnitude of the two designs is depicted in Fig. 6.2.5. In order to achieve a resonance at the same frequency, the air cavity for the alternative design has been set at 4.115mm. In this case the insertion loss at the resonance is 5.44dB as opposed to 0.77dB which corresponds to the original configuration. It is evident that the proposed design is greatly advantageous in terms of losses compared with the alternative one.
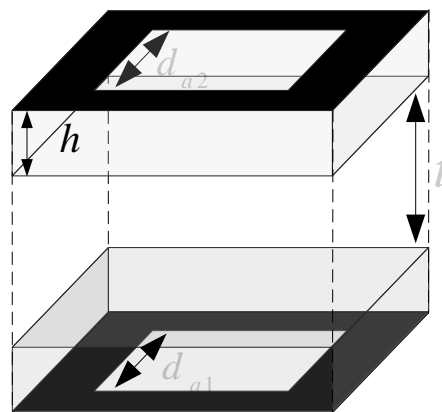

Fig. 6.2.4.   Schematic diagram of alternative structure.
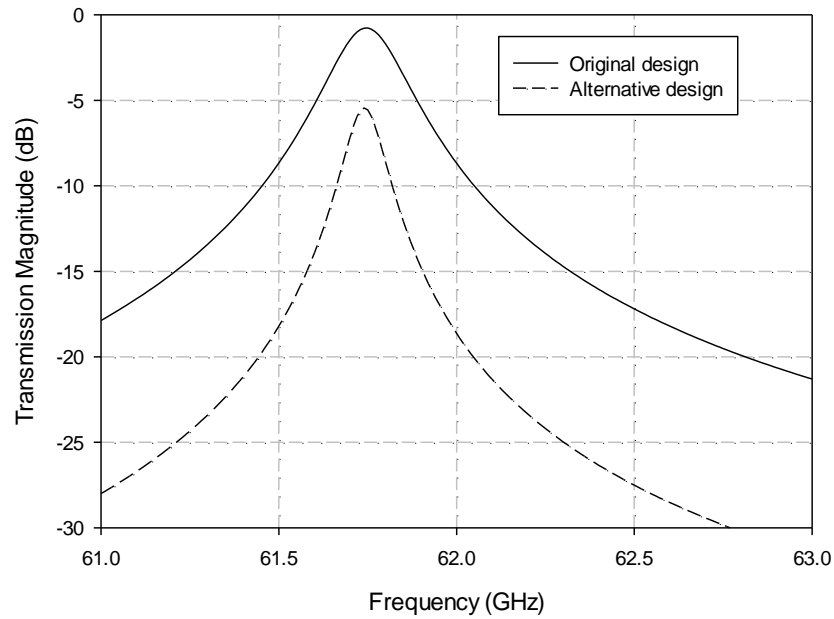
Fig. 6.2.5.   Comparison of transmission magnitude for the original tunable FSmS structure and the alternative design of Fig. 6.2.4.

6.2.2 Fabrication Considerations

For the practical implementation of the proposed tunable FSmS structure some considerations should be made. First of all, the size of the arrays has to be large enough (~10λ) to avoid diffraction effects. Secondly, the appropriate piezoelectric actuators should be selected. For the particular configuration the more suitable piezoelectric actuators are the commercial stack actuators P-885.51 from Physik Instrumente[TM] (PI) that can achieve a nominal maximum displacement of 18μm for an applied voltage of 120V. The reason for choosing these actuators for this type of application is that they can produce the desired displacement (~20μm), they are low-cost and they have high accuracy and fast response [12]. The performance of the specific actuators has already been discussed in Chapter 5, where the same type has been employed for the measurement of the tunable HIS.

164

Finally, due the high frequency operation, the effect of the surface roughness has to be evaluated. It is worth reminding here that in the case of the tunable HIS operating at 60GHz, the surface roughness caused a significant reduction of the copper conductivity resulting in very high losses. Therefore, an evaluation of the copper conductivity effect for the proposed FSmS is presented. The unit cell of the structure has been simulated for the ideal copper conductivity (5.96×10^7 S/m) and for reduced conductivities corresponding to the 50% (2.98×10^7 S/m), 20% (1.192×10^7 S/m) and 5% (0.596×10^7 S/m) of the ideal value. The corresponding transmission magnitude for t=3.37mm is shown in Fig. 6.2.6. It can be observed that even for 0.596×10^7 S/m conductivity, the insertion loss at the resonance is 2.77dB. Therefore, in this type of structure this parameter has a less significant effect compared to HIS structures.
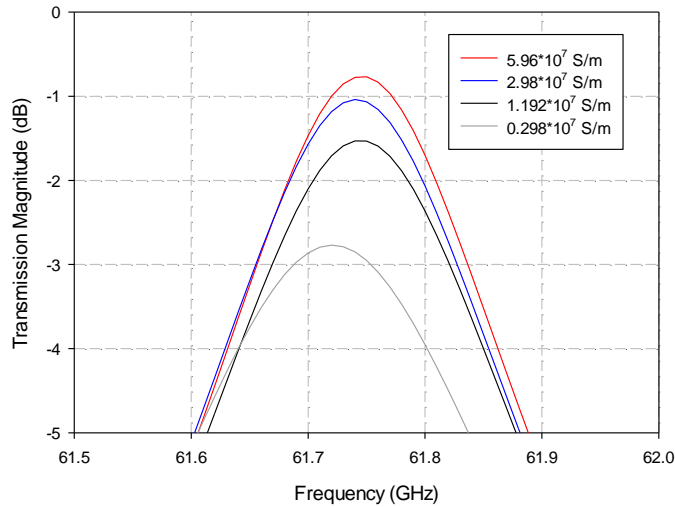

Fig. 6.2.6.   Transmission magnitude for different values of copper conductivity.

6.3 CONCLUSIONS

In this Chapter, dynamically tunable low-loss Frequency Selective Meta-Surfaces have been presented. Initially tunable FSmS structures for lower mm-wave frequencies based on

piezoelectric bender actuators have been demonstrated through simulation and experiments. A new type of FSS has been presented based on multi-layer meta-surfaces achieving a measured tuning of the pass-band of 8.8% for operation around 14.7GHz. Moreover alternative designs have been investigated. The proposed structures and tuning technique are directly scalable to higher mm-wave frequencies paving the way for a new class of low-loss tunable mm-wave FSS and related structures.

Subsequently, tunable double-layer meta-surfaces have been presented employing piezoelectric stack actuators for operation at higher mm-wave frequencies. Simulated results of the proposed configuration consisting of two layers and an air cavity between them showed promising results for tuning the reflection and transmission characteristics of mm-wave meta-surfaces while achieving a low loss performance. Furthermore, a losses evaluation has been carried out and fabrication considerations have been discussed.

REFERENCES

[1] C. L. Holloway, E. F. Kuester, J. A. Gordon, J. O'Hara, J. Booth, and D. R. Smith, "An Overview of the Theory and Applications of Metasurfaces: The Two-Dimensional Equivalents of Metamaterials," *IEEE Antennas and Propagation Magazine*, Vol. 54, No. 2, April 2012.

[2] R. Mittra, C. H. Chan, and T. Cwik, "Techniques for analyzing frequency selective surfaces-a review," *Proc. IEEE*, vol. 76, pp. 593–615, Dec. 1988.

[3] B. Munk, Frequency Selective Surfaces: Theory and Design, Wiley, 2000.

[4] C. Mias, "Varactor-tunable frequency selective surface with resistive-lumped-element biasing grids," *IEEE Microw. Wireless Component Lett.*, vol. 15, no. 9, pp. 570–572, Sep. 2005.

[5] B. Sanz-Izquierdo, E. A. Parker, and J. C. Batchelor, "Switchable frequency selective slot arrays," *IEEE Trans. Antennas Propag.*, vol. 59, no. 7, pp. 2728–2731, Jul. 2011.

[6] B. Schoenlinner, A. Abbaspour-Tamijani, L. C. Kempel, and G. M. Rebeiz, "Switchable low-loss RF MEMS ka-band frequency-selective surface," *IEEE Trans. Microw. Theory Tech.*, vol. 52, no. 11, pp. 2474–2481, Nov. 2004.

[7] J. M. Zendejas, J. P. Gianvittorio, Y. Rahmat-Samii, and J. W. Judy, "Magnetic MEMS reconfigurable frequency-selective surfaces," *J. Microelectromech. Syst.*, vol. 15, no. 3, pp. 613–623, Jun. 2006.

[8] E. A. Parker, S. B. Savia, "Active frequency selective surfaces with ferroelectric substrates," *Proc. Inst. Elect. Eng. Microwaves, Antennas and Propag.*, vol. 148, pp. 103–108, Apr. 2001.

[9] W. Hu, R. Dickie, R. Cahill, H. Gamble, Y. Ismail, V. Fusco, D. Linton, N. Grant, and S. Rea, "Liquid crystal tunable mm wave frequency selective surface," *IEEE Microw. Wireless Compon. Lett.*, vol. 17, no. 9, pp. 667–669, Sept. 2007.

[10] A. C. Lima and E. A. Parker, "Fabry–Perot approach to the design of double layer FSS," *Proc. Inst. Elect. Eng. Microw. Antennas Propag.*, vol. 143, no. 2, pp. 157–162.

[11] K. Konstantinidis, A. P. Feresidis, P. S. Hall, "Broadband Sub–Wavelength Profile High-Gain Antennas Based on Multi-layer Metasurfaces," *IEEE Trans. Antennas Propag.*, vol. 63, no. 1, pp. 423–427, January 2015.

[12] www.physikinstrumente.co.uk

CHAPTER 7.

CONCLUSIONS AND FUTURE WORK

Tunable microwave metamaterials have attracted significant research interest in recent years, due to the important requirement for reconfigurable and multi-functional systems such as frequency reconfigurable or beam-scanning antennas, tunable filters, reflectarrays and many more. This PhD dissertation has studied and proposed novel designs of metamaterial structures and introduced novel techniques and configurations for tuning metamaterials at microwave and mm-wave frequencies. The proposed tuning techniques offer the advantages of low complexity implementation, low cost, low loss performance. For the analysis of the aforementioned structures and estimation of their performance, theoretical approaches and simulation tools have been employed, which were introduced in Chapter 2.

In Chapter 3, novel tunable two-layer slot-patch Electromagnetic Band-Gap (EBG) structures have been presented for microwave frequencies. The proposed structures have been based on varactor diodes achieving a wide tuning of the EBG band-gap with significantly simplified biasing network. Subsequently, the proposed tunable EBG structures have been employed for isolation enhancement of two closely spaced printed wideband monopole antennas. Moreover, tunable monopoles have also been presented based on the proposed two-layer biasing technique and an isolation between them has been achieved using the proposed tunable EBG structures. Prototypes of the proposed structures have been fabricated and measured validating the simulation results. Thus, the work performed in this Chapter has led to three contributions: first the proposal of novel tunable EBG structures, secondly the design of tunable antennas and thirdly the proposed simplified two-layer biasing technique which can be applied to a number of different applications involving electrically tunable structures.

In Chapter 4, dynamically tunable low-loss High Impedance Surfaces based on piezoelectric bender actuators for low mm-wave frequencies have been demonstrated through simulation and experiments. The proposed HIS structures have been designed such that maximum tunability is obtained employing piezoelectric bender actuators to electromechanically change the HIS cavity thickness. This has led in significant tuning of the reflection phase response of the structures. A prototype has been fabricated operating around 14GHz and measurements have demonstrated the operation of the structure as an active impedance surface with low losses performance. Moreover, as an application of the proposed tunable HIS structures, a tunable dipole antenna with an active HIS ground plane has been presented. The work presented in this Chapter has led to further investigation and scaling of the proposed structures and tuning technique to higher mm-wave frequencies which has been carried out in Chapter 5.

Thus, in Chapter 5 tunable low-loss HIS type phase shifting surfaces have been presented for operation at higher mm-wave frequencies. These have been based on stack multilayer piezoelectric actuators giving significantly less displacement than the bender actuators employed in Chapter 4. Nevertheless, a measured phase shift of over 200° at 58.14GHz has been obtained with the proposed tunable HIS. Moreover an evaluation of the main factors contributing to losses in this type of structures operating at mm-wave and submm-wave frequencies has been presented giving useful information about design considerations that have to be made at such frequencies. Finally a 1D hollow Leaky-Wave Antenna (LWA) configuration with a continuous beam steering of 35° has been proposed based on the proposed tunable HIS.

Finally, in Chapter 6, tunable Frequency Selective Meta-Surfaces (FSmS) have been presented for both lower and higher mm-wave frequencies applying the tuning techniques

described in Chapters 4 and 5 respectively. Initially, a novel design of FSS has been presented based on multi-layer meta-surfaces for lower mm-wave frequencies. The tuning of the proposed FSS has been demonstrated using piezoelectric bender actuators with a measured tuning of the pass-band of 8.8% and very low insertion loss values. Similarly to the tunable HIS structures presented in Chapter 4, the proposed FSmS structures have the advantage of being scalable to higher mm-wave frequencies paving the way for a new class of tunable low loss metasurfaces and related applications. As a proof of the concept for higher mm-wave frequencies, tunable double-layer FSmS have been presented next employing piezoelectric stack actuators. Simulation results have shown that the proposed structure can be tuned from a transmitting to a reflecting structure for a specific operating frequency.

Overall, the work carried out in this thesis has achieved to solve some of the most important issues that correspond to tunable metamaterials, especially for mm-wave frequencies, such as parasitic effects and switching speeds. Moreover, it has been demonstrated that low loss tuning techniques can be employed with the appropriate choice of fabrication procedures and materials. Future work could include new developments of new structures by taking advantage of the tuning techniques and technologies presented here. More specifically the piezoelectric actuators presented in this thesis can be employed to develop new high performance tunable mm-wave structures. Also some of the novel designs could lead to new types of antennas and FSS based structures.

Particularly, as future development of the work carried out in Chapter 5, the beam scanning antenna could be further investigated, particularly in terms of designing and implementing a suitable feeding. Subsequently, a prototype could be fabricated and measured to validate the beam steering capabilities of the structure.

Furthermore, the concept of tunable HIS structures based on stack piezoelectric actuators can be employed to design tunable reflectarrays. This could be designed by dividing the periodic surface in lines of elements and imposing a different displacement at each line (each of which would be supported by a set of actuators). With a careful design, a non-uniform continuous height variation, could synthesize non-uniform phase responses. This could produce a controllable phase shift at each line of elements and consequently a dynamically tunable reflectarray.

Finally, the proposed tuning technique based on piezoelectric actuators could be extended to design tunable metamaterial structures and antennas THz frequencies. Using the appropriate fabrication techniques for such frequencies, optically flat periodic surfaces could be constructed and used to create an active ground plane for a beam scanning antenna at submm-waves with very low loss performance. This could be extremely useful in the currently investigated THz imaging systems where electronically controlling the pointing angle of the antennas' beam is required.

The findings and results of this PhD dissertation have been presented at several European and international conferences. Namely, in the Loughborough Antennas and Propagation Conference (LAPC) of 2012 and 2014, the European Conference on Antennas and Propagation (EuCAP) of 2013-5, the European Microwave Conference (EuMC) of 2013 and the Metamaterials Congress (Metamorphose) of 2014. Moreover, a part of the work presented in Chapter 5 has been published in IET Microwaves, Antennas and Propagation while another part has been submitted for publication at Antennas and Wireless Propagation Letters (AWPL). Also, the work presented in Chapter 3 has been accepted for publication at IEEE Transaction on Antennas and Propagation (TAP). Finally part of the work presented in Chapter 6 has also been submitted in IEEE Transaction on Antennas and Propagation (TAP).